Deuterium Retention in Carbon, Beryllium, and Carbon Layers on Titanium and Beryllium

K.U. Klages

Submitted for the Degree of
Doctor of Philosophy
from the
University of Surrey

UniS

School of Electronics and Physical Sciences
University of Surrey
Guildford, Surrey GU2 7XH, UK

Max-Planck-Institut für Plasmaphysik, EURATOM Association
Boltzmannstraße 2, 85748 Garching, Germany

September 2005

Summary

In the context of plasma-facing walls in future nuclear fusion devices, a knowledge of the reaction mechanisms and properties of these materials is essential for operation and safety. The aim of the studies for this thesis was to investigate the effect of implanting keV deuterium ions in various mixed and pure materials.

To do so required an adaptation of the existing ultra-high vacuum experiment Artoss; the modified version of this apparatus allowed the detection of hydrogen isotopes, besides having an updated vacuum system where vacuum conditions with base pressures of less than 3×10^{-9} Pa were achieved.

Using Artoss and another ultra-high vacuum device (XPS), clean samples of crystalline beryllium, highly-oriented pyrolytic graphite, and mixed materials consisting of beryllium and titanium substrates with carbon surface layers of less than 10 nm thickness were bombarded with 1 and 4 keV deuterium ions.

Deuterium retention in clean metallic beryllium was found to saturate at $2 \times 10^{15}/cm^2$; beryllium samples prepared with carbon surface layers displayed higher hydrogen isotope retention.

In addition to eroding the carbon surface layer, the deuterium ions carry the energy to modify the carbon surface layer, creating metallic carbide phases.

Carbon in its elementary form was found to erode at a significantly greater rate than carbon in the metallic carbide phases. The erosion behaviour of titanium carbide is in good agreement with computer simulations of a kinematic sputtering model, whereas the exponential erosion rate of elementary carbon suggests that chemical interactions play an additional important role.

These findings suggest that beryllium, despite being a highly toxic material, is well suited as a first-wall material in future fusion devices, provided a high-quality vacuum can be consistently achieved.

Key words: Nuclear fusion, hydrogen retention, surface science, XPS, ion beam analysis, beryllium, titanium, carbon, carbides

Email: konrad.klages@ipp.mpg.de

Acknowledgements

Table of contents

List of Figures

Glossary of Terms

acronym	explanation
amu	Atomic mass unit
a.u.	arbitrary units
CFC	Carbon fibre composite
ERD	Elastic recoil detection
FWHM	full-width at half-maximum
HOPG	Highly-oriented pyrolytic graphite
HREELS	High resolution electron energy loss spectroscopy
IBA	Ion beam analysis
IMFP	Inelastic mean free path
IS 1	Ion source 1
IS 2	Ion source 2
ISS	Ion scattering spectroscopy
ITER	International thermonuclear experimental reactor
JET	Joint European Torus
NRA	Nuclear reaction analysis
PFC	Plasma-facing component
QMS	Quadrupole mass spectrometry
RBS	Rutherford backscattering spectrometry
TDS	Thermal desorption spectroscopy
TRIDYN	Computer simulation code: dynamic adaptation of the TRIM code
TRIM	Computer simulation code: transport of ions in matter
UHV	Ultra-high vacuum
UPS	Ultra-violet photoelectron spectroscopy
XPS	X-ray photoelectron spectroscopy
Z	atomic number

1 Introduction

The growth in demand for energy both in the industrialised and the developing world has led to a rapid consumption of the available natural resources coal, oil, and gas. To maintain the current standard of living in an industrialised world, a continued availability and supply of energy is essential. At the same time, the burning of fossil fuels leads to the emission of so-called "greenhouse gases", in particular carbon dioxide (CO_2) into the atmosphere. This accelerates global warming, a general increase in the temperature of the atmospheric air and seawater.

Therefore, and especially with a decrease in natural resources - and thus an increase in energy prices - alternative energy sources are urgently sought. Numerous possibilities have been developed in recent years. Some countries, for example France, gain the bulk of their electricity supply through conventional nuclear energy, which is obtained through nuclear fission of heavy nuclei. Nuclear fission enables a supply of electricity without emission of greenhouse gases. However, the catastrophe at the conventional nuclear power station in Chernobyl, USSR/Ukraine, in 1986 highlighted the risks of using a nuclear chain reaction to obtain electricity. Furthermore, long-term storage of radioactive wastes with lifetimes of thousands of years leads to concerns.

Argentina, Brazil, Canada, China, Finland, India, Iran, North Korea, Russia, Pakistan, Japan, South Korea, Taiwan, Ukraine, and the U.S.A., are currently planning or building new nuclear reactors or reopening old ones. Bulgaria, the Czech Republic, Egypt,

France, Indonesia, Israel, Romania, Slovakia, South Africa, Turkey, and Vietnam are considering doing this. Armenia, Belgium, Germany, Hungary, Lithuania, Mexico, the Netherlands, Slovenia, Spain, Sweden, Switzerland, and the United Kingdom have nuclear reactors but currently no proposals for expansion.

Alternative possibilities for electricity supplies are the use of the natural resources wind, water, and sun. The development of wind turbines, hydroelectric plants, and solar panels in the past decades has led to the installation of these facilities in suitable regions. Whilst these alternative sources of energy allow the use of electricity without the emission of gases that are harmful to the environment, there is currently no energy source available which delivers electricity on a sustainable level to satisfy the current or predicted future demands without negative side effects for the environment or life on Earth.

1.1 Thermonuclear fusion as an energy source

For several decades, nuclear fusion has been seen as a potential source of energy, not least since it is this kind of a reaction that powers the sun. There are various competing forces stabilising an atomic nucleus; Figure 1 shows the binding energy per nucleon as a function of atomic mass number. As the binding energy of light nuclei increases with atomic mass number, it is clear that they also become more stable until a maximum is reached for nuclei close to iron. Beyond this maximum, nuclear stability decreases,

though more slowly than in the other direction. This peak is the basis both of nuclear fusion and fission. The energy released in the fusion of e.g. deuterium (D) with tritium (T) nuclei is 3.5 MeV/amu, compared with 1 MeV/amu in nuclear fission.
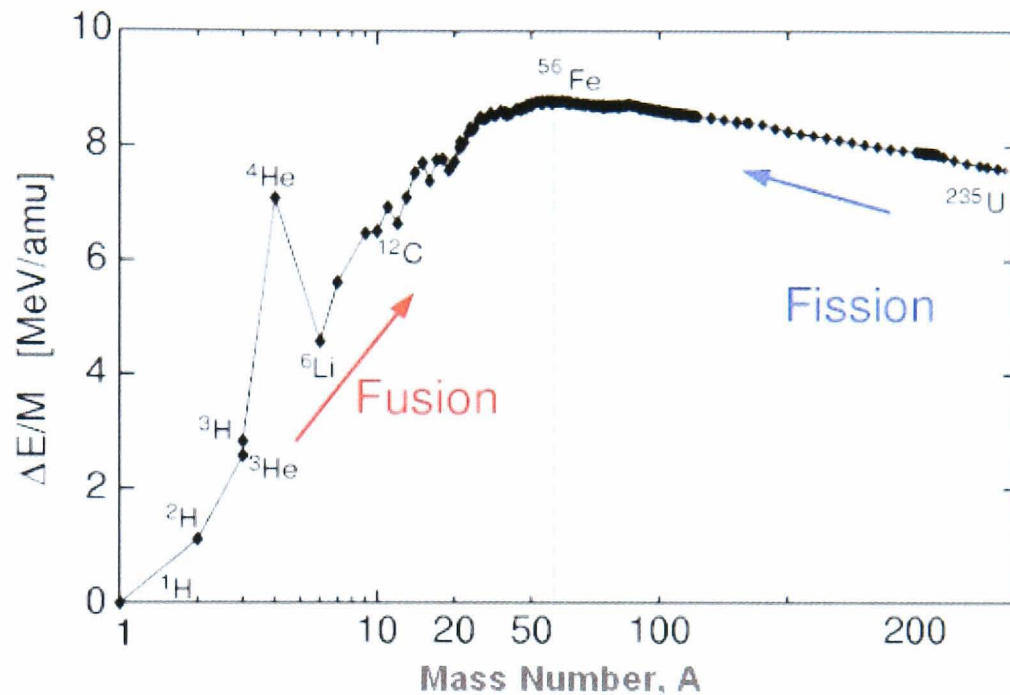
Figure 1: Binding energy per nucleon as a function of atomic mass number

For the fusion of two light nuclei to occur, it is necessary to bring the nuclei together sufficiently closely for the attractive short-range nuclear strong force to exceed the Coulomb repulsion. As the mass of the resultant nucleus is slightly smaller than the combined mass of the two original nuclei, this mass difference is converted into kinetic energy of the fusion products. The distribution of this kinetic energy is reciprocally proportional to the masses of the fusion products.

Investigations into the field of controlled nuclear fusion have in the past focused on the creation of suitable conditions for fusion to occur. This requires high kinetic energies of

the original particles (or equivalently high temperatures T), a sufficiently high density

n of nuclei, and a long energy confinement time τ. To achieve ignition of a nuclear

fusion reactor, the fusion product must exceed $n \cdot T \cdot \tau = 6 \times 10^{21} \, m^3 \, keV \, s$.

As can be seen in Figure 2, the fusion of deuterium (D) and tritium (T) nuclei requires

the least energy. Consequently, efforts to create fusion reactions in laboratories have

been mainly directed towards fusion of these two nuclei:

$$D + T \rightarrow \alpha \, (3.5 \, MeV) + n \, (14.1 \, MeV)$$ Equation 1

In this reaction an energy of 17.6 MeV is released. As a neutral particle the neutron is

not trapped by the toroidal magnetic chamber and is free to leave the plasma. Its energy

is thus available for extraction.
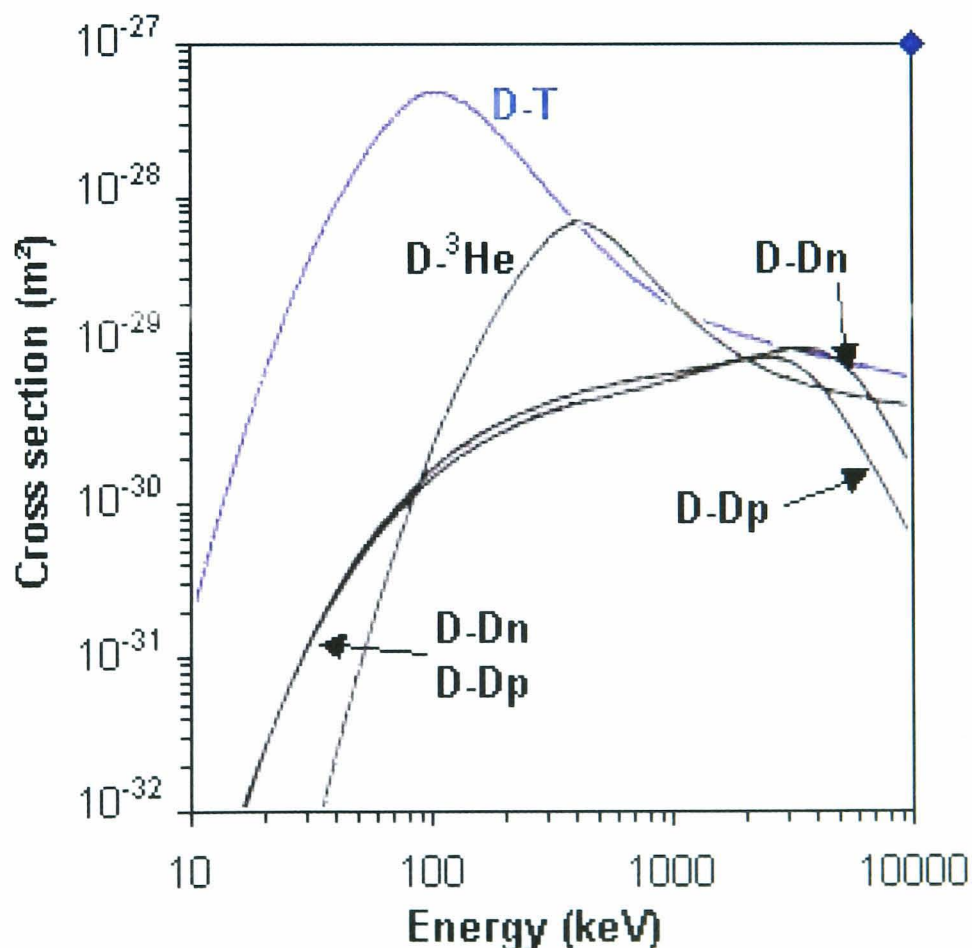
Figure 2: Cross-section of fusion for various reactions involving deuterium, as a
function of energy.

4

The progress that has been made over the past 50 years in achieving the conditions necessary for fusion to operate as a sustainable energy source has been substantial. Figure 3 shows the performance of past and present experimental fusion devices. A significant step was taken at the Joint European Torus (JET) in 1991, where for the first time a significant amount of energy was obtained in a controlled fusion process. This reinforced the idea that nuclear fusion has the potential to act as a future energy supply.
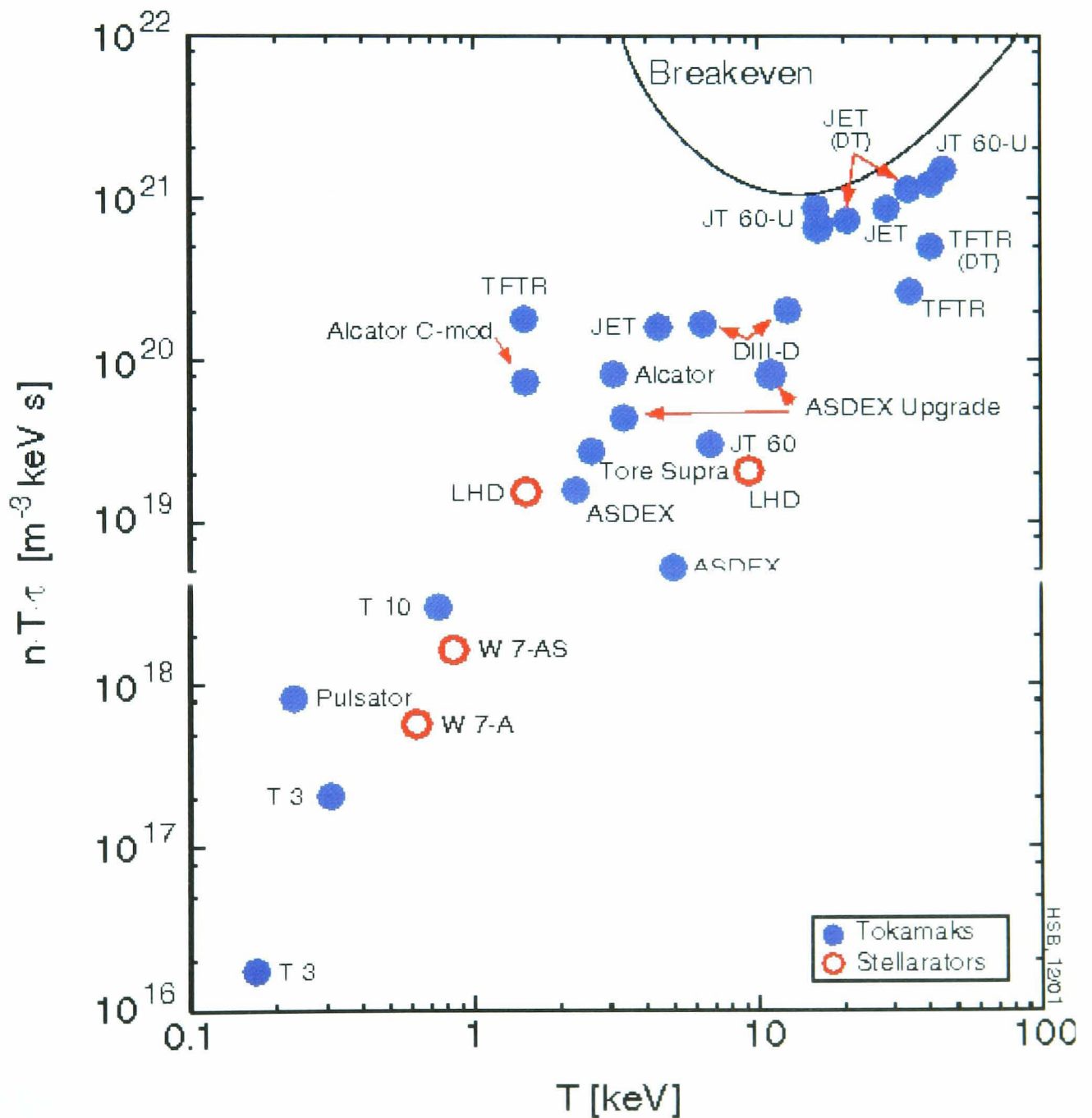
Figure 3: The fusion product $nT\tau$ vs. kinetic energy. At the break even condition the amount of energy obtained equals the amount of energy invested.

One possible way of achieving the conditions required for fusion of deuterium with tritium nuclei is to create a magnetically confined D/T plasma with a kinetic energy of about 10 keV of the hydrogen isotope ions. This corresponds to a plasma temperature of $10^8 K$.

In the so-called tokamak design of a nuclear fusion device, a plasma is contained in a toroidal magnetic field which is maintained by a set-up of toroidal coils. This setup is shown schematically in Figure 4(a). As the intensity of the magnetic field in a toroidal arrangement of field coils decreases radially, a drift of the plasma is induced which would result in an inevitable contact of the plasma with the inside surface of the vacuum device. To avoid this drift, an additional magnetic field is created through an induced toroidal electric current in the plasma, which leads to several poloidal revolutions of the field lines during one toroidal traversal of the tokamak (Figure 4 a). This current also heats the plasma together with microwave and neutral particle injection, and finally the energy deposited by the α-particles created in the fusion process. The stellarator design (Figure 4 b) operates without the induced plasma current. The design of stellarators is some decades behind the tokamaks; its advantage is the basic steady-state operation.

(a) Tokamak   (b) Stellarator
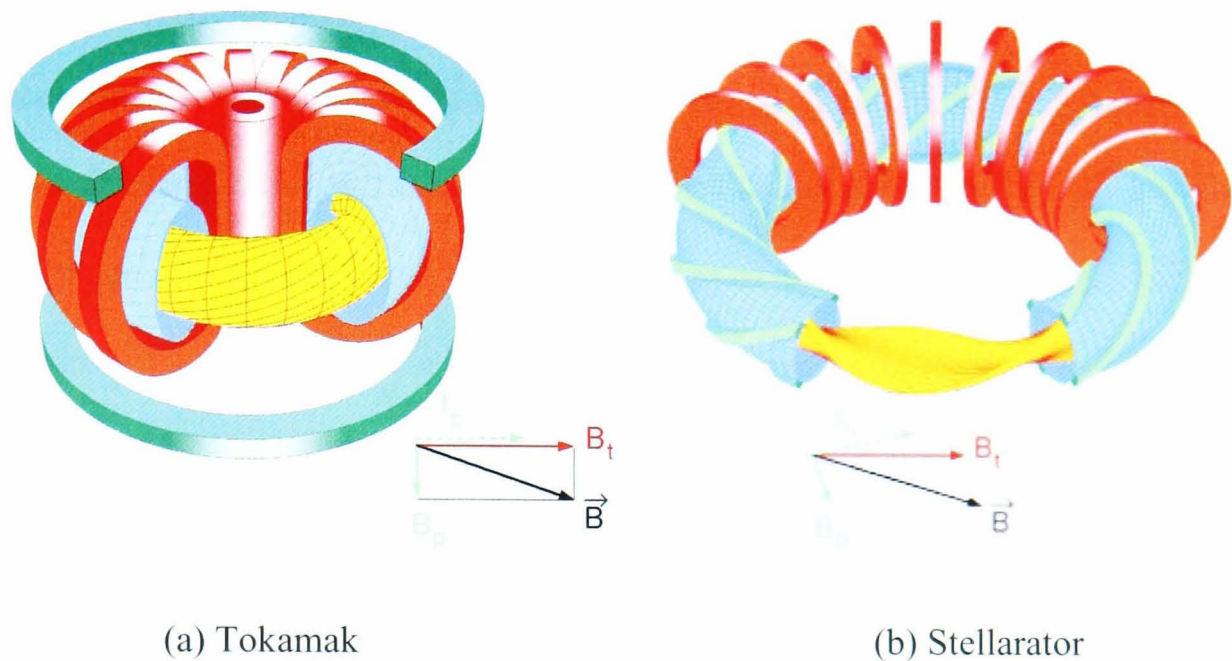
Figure 4: Schematic view of two magnetic setups for fusion devices. The tokamak design will be used in ITER. The stellarator operates in a steady-state mode without induced plasma current.

Despite the magnetic confinement of the plasma, charged particles escape from the magnetic cage due to collision events and interact with the first-wall of the reactor. The expression "first-wall" describes the plasma-facing inside surface of the vacuum vessel. Ions with several 100 eV impact on the inner wall of the main chamber of tokamak devices, while the divertor and high particle-flux baffle regions of the reactor experience particle implantation at some eV and some hundreds eV, respectively [Fed01]. In addition, energetic plasma ions neutralised in collisions with thermal neutral atoms recycling from the walls are not confined by the magnetic field and hit the vessel walls with energies of up to 10 keV. The interaction of charge-exchange neutrals from the plasma was investigated by H. Verbeek *et al.* [Ver98].

The interaction of these particle and heat loads with plasma-facing wall components together with the neutron irradiation establishes the plasma-wall interaction. Aspects of plasma-wall interactions that are particularly important for the operation and safety of future fusion devices are the erosion of wall materials as well as the hydrogen isotope inventories in the plasma-facing components (PFC). Erosion of the first-wall must be minimised as the penetration of eroded atoms will lead to a dilution of the plasma. Especially impurities of heavy elements in the plasma must be avoided as these will not completely ionise, leading to radiative power losses from the bound electrons. This power loss results in cooling of the plasma which deteriorates the required conditions for the nuclear fusion of ions from the plasma.

Eroded wall material migrates to other parts of the vacuum vessel as plasma impurity. These impurities are re-deposited on the first-wall of the chamber with particle energies ranging from thermal energy (a few eV) to several keV. Deposition and implantation of plasma impurities on the first-wall thus leads to the formation of multi-material surface layers which exhibit altered physical and chemical properties compared to the originally designed first-wall material. As a result of investigations of plasma-wall interactions the current design for the next step tokamak fusion experiment, the "International Thermonuclear Experimental Reactor" (ITER) [ITER96, Con97, Par00, Jan01] envisages to tile large areas of the first wall of the chamber with beryllium, while the high-flux divertor region will be coated with tungsten and carbon fibre composite (CFC) tiles as shown in Figure 6.

Beryllium was chosen due to its low atomic mass which allows significantly greater impurity concentrations in the plasma, as shown in Figure 5. In contrast to carbon, the

erosion of beryllium through chemical interactions with hydrogen isotopes is reduced substantially.
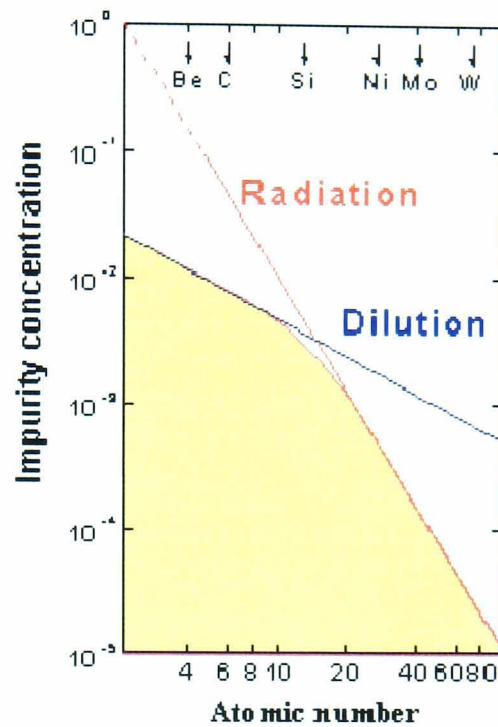
Figure 5: Permitted plasma impurity concentration for increasing atomic numbers. For light atomic nuclei the allowed impurity concentration is dilution-limited, whereas impurities consisting of heavy ions lead to radiative power loss.

The high-flux regions of a fusion reactor will experience high particle and heat loads. These regions will therefore be fitted with tungsten, for reduced sputtering through particle loads due to its high atomic weight, and carbon-fibre composite materials, which can withstand high transient heat loads due to the high temperature of sublimation of carbon of 4000 K.
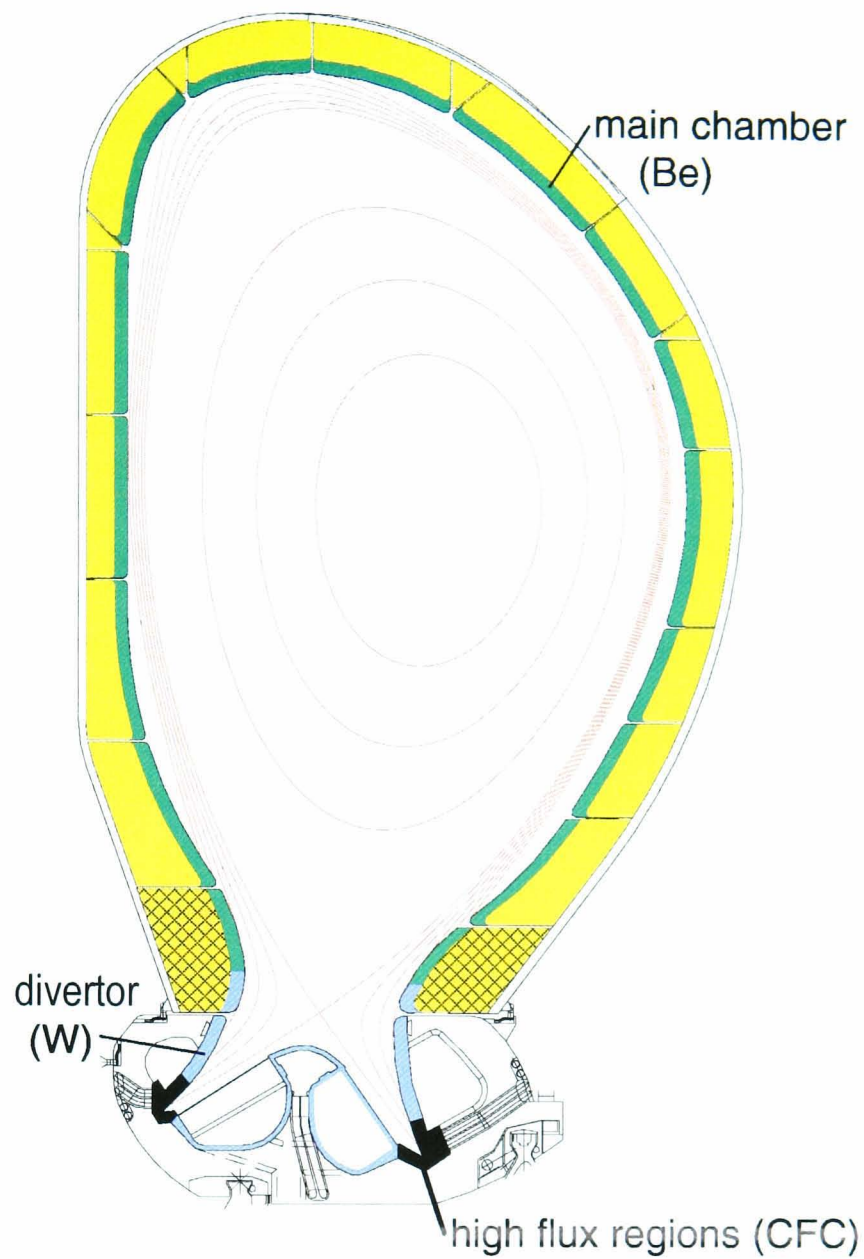
Figure 6: Poloidal cross-section through the planned "International Thermonuclear Experimental Reactor" (ITER). The regions where beryllium, tungsten and carbon fibre composites (CFC) are planned as first-wall material are indicated.

Most current nuclear fusion testing devices are equipped with carbon tiles as plasma-facing material because the benefits of carbon as first-wall material are its high temperature of sublimation and the low atomic number, which allows a large impurity concentration of the plasma during operation (Figure 5).

However, the chemical erosion of carbon due to hydrogen is a substantial drawback of carbon as a first-wall material. It has been shown that especially at low energies (< 100 eV) which are typical for ions in the plasma edge, there is a significant chemical erosion of carbon due to hydrogen ion bombardment [Rot96].

As an alternative first-wall material Beryllium has the disadvantage of a low melting temperature (1560 K). However, it shares the low-Z advantage of carbon, and more importantly, chemical erosion due to hydrogen is not known. Furthermore, as a highly reactive getter material beryllium accumulates impurities from the vacuum chamber, thus reducing the contamination and therefore dilution of the plasma.

As the fusion reaction requires the use of the radioactive hydrogen isotope tritium (cf. equation 1), the knowledge about the hydrogen inventory of materials is essential for the choice of the plasma-facing first-wall material in magnetic confinement nuclear fusion devices. The hydrogen isotope tritium (^3H) is a low energy β^- emitting isotope with a half-life of 12.3 years, and hence trapping of tritium in the plasma-facing components (PFC) will lead to activation of the first-wall. It has been observed [Par00] that deposited surface layers have a great influence on the hydrogen inventory in the first-wall materials.

1.2 Hydrogen retention in beryllium

The present work is carried out to investigate the fundamental processes governing the hydrogen inventory in well-defined materials. In particular, deuterium ion bombardment of prepared titanium and beryllium substrates as well as these metals with well-defined carbon surface layers was studied.

Models to describe the behaviour of wall materials have been based on kinematic interactions [Nau92, Hir97]. So far most research into plasma-wall interactions was carried out by analysing wall tiles or probes which had been inserted into fusion devices [May97]. This method yields information on the time-integrated macroscopic plasma-wall interactions. However, it is difficult to investigate and understand the underlying processes which lead to the behaviour observed in tiles that have experienced a long campaign in a large-scale experimental fusion device.

In order to predict the behaviour of first-wall materials for the strongly varying conditions in a full-scale fusion device, the fundamental properties of the particle-surface interactions must be studied under well-defined conditions. Individual processes such as particle reflection, sputtering or hydrogen retention have to be investigated on specifically prepared elementally clean and intermixed surfaces. These investigations must be performed in ultra-high vacuum conditions in order to minimise the effect of surface impurities from the residual gas in the vacuum system. Only ultra-high vacuum

(UHV) conditions at residual gas pressures lower than 10^{-8} Pa allow the study of clean metallic samples without oxidic surface layers.

The ideal choice of material for the investigation of the fundamental properties of a material is a single crystal, which eliminates effects due to grain boundaries, impurities, vacancies and porosity of the material. Whilst the effects of impurities from eroded first-wall material in the plasma are important for the operation of a nuclear fusion experimental device, individual properties of the materials which are considered for future first-wall operation can only be distinguished on single crystals.

To date only very few of the studies have been performed investigate the properties of beryllium were conducted in ultra-high vacuum. Whilst as plasma-facing material beryllium is not kept in ultra-high vacuum in fusion devices, it is only under these conditions that the underlying processes can be distinguished. Many of these studies have yielded widely varying results for the parameters being investigated [May97, May98, Cau02].

Many of these variations may be due to the effects of undefined surface oxide layers. Laboratory plasma experiments [Cau90a] have shown that hydrogen retention in beryllium is strongly affected by the presence of oxide and carbide on the surface of beryllium. It was found that no detectable permeation of hydrogen was obtained for temperatures below 670 K [Cau90b].

Analysis of the hydrogen transport behaviour of beryllium has been conducted by R.A. Anderl *et al.* [And92]. Their work was carried out studying polycrystalline beryllium in a vacuum chamber with a base pressure lower than 10^{-6} Pa, and their studies showed that the formation of an oxide layer during the course of the analysis had a significant effect on the retention of hydrogen isotopes in beryllium. It was observed that at 750 K hydrogen solubility in beryllium is 30 times higher than in beryllium oxide (BeO). A model was proposed in which a BeO layer acts as a diffusion barrier.

The study of hydrogen capture of carbidic surface layers by K. Ashida *et al.* [Ash97] indicates that the chemical state of the carbon has a great influence on the hydrogen inventory of the material. Their analysis was carried out by creating carbon/hydrogen surface layers through radio frequency discharge of ethylene (C_2H_4), where the hydrogen was captured in chemical bonds with carbon after deposition. Thermal treatment up to 1073 K did not lead to significant desorption of hydrogen. Although the surfaces of the samples in this analysis were contaminated with 20 at.% Zn from the electrode that was employed during carbon vapour deposition, it was observed that samples with a beryllium carbide, Be_2C, surface layer exhibited only a minor capacity for the capture and retention of hydrogen.

In agreement with measurements by J. Roth *et al.* [Rot97] the analysis that has been carried out until now clearly shows that to understand the mechanisms governing the hydrogen inventory in first-wall materials, it is necessary to investigate well defined samples in very well defined conditions.

All the above studies were performed on polycrystalline beryllium samples in vacuum conditions at pressures greater than 10^{-7} Pa , which unavoidably lead to beryllium oxide surface layers as impurities.

For the work presented in this thesis, the samples used are Be (0001) single crystals. Using single crystalline samples allows the detachment of the effects of initial damage in the crystalline structure from damage that results from the sample treatment. This separation is significant in order to distinguish the effects of ion bombardment from those on the *ab initio* condition of the crystalline structure of a sample.

The apparatus Artoss, which is described in detail in chapter 3.1, allows not only the preparation of mixed carbon and oxygen surface layers but also *in situ* implantation of hydrogen isotope ions and analysis of the sample with a variety of experimental techniques.

These investigations build on the results of P. Goldstraß [Gol99], who assembled parts of the apparatus Artoss to investigate the formation of carbide on a beryllium single crystal with (0001) orientation through implantation of C^+ and CO^+ ions and annealing of vapour deposited carbon surface layers.

However, the influence of the carbide formation on the retention of implanted hydrogen could not be investigated using the original setup of the apparatus. In the context of the present work a major reconstruction of the setup of Artoss was carried out. The main vacuum chambers were replaced and a new vacuum pumping system was installed. The

base pressure of the target-holding main chamber was reduced to 3×10^{-9} Pa through the use of a turbomolecular pumping system, liquid nitrogen cooling, and titanium sublimation.

The apparatus was relocated and connection to a new 3 MV tandem accelerator was completed. New diagnostics have been added to allow the detection of hydrogen isotopes and the study of interactions between implanted ions and surfaces of solids.

The new experimental possibilities of Artoss are discussed in chapter 2, Experimental techniques, and the setup is described in chapter 3.1, Apparatus: Artoss.

Chapter 4 deals with computer simulations which were performed to assist the analysis of the measured data. In particular, the simulation code TRIDYN is described.

The performance of measurements is explained in chapter 5. The possibilities and limits of the experimental setups are also discussed in this section.

Chapter 6 presents the results on the effect of deuterium ion bombardment of highly oriented pyrolytic graphite, titanium, and carbon layers on titanium on the chemical states of the surface of samples with X-ray photoelectron spectroscopy. Results on the physical composition, deuterium retention, and chemical surface states of beryllium and beryllium-carbon systems are presented in section 6.3.

A discussion of the obtained results is given in section 6.4, and chapter 7 offers a concluding summary.

2 Experimental techniques and data evaluation

In order to analyse the elemental composition of the surface of mixed materials consisting of metals, carbon and hydrogen isotopes, a variety of experimental techniques are required. Combining these techniques in the ultra-high vacuum system Artoss it is possible to observe and quantify the composition of mixed materials and to measure the chemical states of the involved atoms in the surface layer.

Quantitative information on the composition and depth profiles of the constituents of a sample can be studied through the accelerator-based techniques that are explained in detail in section 2.1: Rutherford backscattering spectrometry (RBS), nuclear reaction analysis (NRA), and elastic recoil detection (ERD).

To identify the chemical states of a specimen photoelectron spectroscopy is required as discussed in section 2.2. X-ray photoelectron spectroscopy (XPS) yields information on the binding energy of core electrons. Chemical interactions of constituents of a sample are identified through shifts in binding energies.

Furthermore, desorbed or emitted particles, in particular hydrogen isotopes, may be detected with a quadrupole mass spectrometer in order to investigate thermal desorption and re-emission of implanted ions (see section 2.3).

2.1 Accelerator-based techniques

In accelerator-based ion beam analysis (IBA) techniques the sample is exposed to a monoenergetic ion beam, and detectors count particles coming back from the sample. Figure 7 shows a schematic diagram of the collision. Depending on the geometry of the setup, and the type and energy of the incoming ion beam a number of regimes are possible:

- heavy elements in a sample can be measured using backscattered light projectiles at a high scattering angle. This setup is known as Rutherford backscattering spectrometry (RBS).

- Recoiling light elements may be observed using heavier projectiles and a small scattering angle, also known as elastic recoil detection analysis (ERD).

- Some combinations of projectile and target isotopes also allow the detection and quantification of a particular target isotope through a nuclear reaction between projectile and target resulting in high-energy emission reaction products (e.g. protons and α-particles). This technique is known as nuclear reaction analysis (NRA).

The knowledge of the slowing-down of ions in traversed matter is of fundamental importance in methods of material analysis using beams of charged atomic particles. Depth perception follows directly from the energy lost by the probing particles.

Many of the features of a backscattering spectrum are due to the energy loss of the analysis beam ions as they traverse the sample material. Hence, a quantitative knowledge of this energy loss is a key element in understanding a backscattering spectrum.
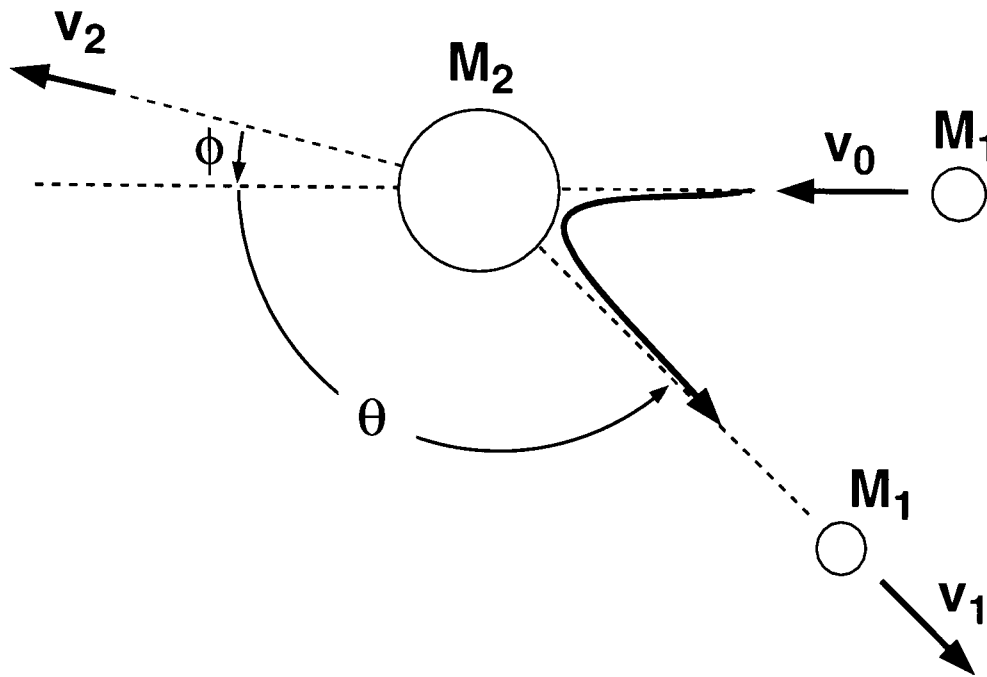
Figure 7: Schematic diagram of an elastic collision between a projectile M_1 and target atom M_2. The scattering angle of the projectile θ and the direction of the target ϕ are labelled. The initial and final velocity of the projectile are given by v_0 and v_1, and v_2 is the velocity of the target after the collision.

The stopping power of a material for a particular ion is defined as the energy loss per distance travelled in the material, denoted by dE/dx. This quantity depends on the ion, its energy, and the traversed material.

The stopping cross-section ε is defined as the ratio of energy loss and areal density of atoms.

Thus, the relation between stopping power and stopping cross-section is given by

$$\frac{dE}{dx} = N\varepsilon \qquad\qquad \text{Equation 2}$$

where N denotes the number of target atoms per unit area.

When a beam of charged particles penetrates matter, the slowing down of projectile ions is accompanied by a spreading of the beam energy. This phenomenon, known as "straggling", is due to statistical fluctuations in the number of collision processes. In material analysis with ion beams straggling broadens the measured energy distributions, which is discussed in chapter 2.1.1. This may limit depth and mass resolution.

To utilise ion backscattering for depth profiling of sample surfaces, it is necessary to relate the energy of the scattered particle to the depth in the sample where the scattering occurred. This depends on the energy loss of the analysis beam in the target, the kinematic factor for the scattering, the experimental setup, as well as the orientation of the sample.

2.1.1 Rutherford Backscattering Spectrometry (RBS)

Rutherford Backscattering Spectrometry (RBS) is based on elastic collisions between projectile ions from a monoenergetic beam and target atoms in a sample. To obtain

depth profiles of target atoms, the energy of backscattered ions is measured in surface

barrier detectors at a high backscattering angle.

The energy measured for a backscattered particle depends on two processes:

- Elastic scattering and

- Inelastic effects of nuclear and electronic interactions with the traversed material.

Particles lose energy as a result of the collision with a target nucleus. A particle will also

lose energy while it traverses the sample, both before and after the collision due to

electron interactions while passing the target atoms.

The energy E_1 of a backscattered projectile is a function of the energy of the incoming

ion E_0, the scattering angle θ and the masses of the projectile ion M_1 and target atom

M_2. The kinematic factor K is defined by the ratio of the projectile energy after and

before the collision:

$$K = \frac{E_1}{E_0} = \left[\frac{\sqrt{1 - \left(\frac{M_1}{M_2} \sin \theta \right)^2} \pm \frac{M_1}{M_2} \cos \theta}{1 + \frac{M_1}{M_2}} \right]^2 \qquad \text{Equation 3}$$

From conservation of energy and momentum it follows that backscattering is only

possible from atoms that are heavier than the projectile ion.

The energy loss as the projectile passes through the sample is given by the stopping

power dE/dx (cf. equation 2).

The number of backscattering events that occur from a given element in a sample also depends on two factors: the concentration of the element and the effective size of its nucleus. The probability that a material will cause a collision is described by the scattering cross-section σ.

For a proportion dQ/Q of particles deflected into the solid angle $d\Omega$, the differential cross-section is defined as

$$\frac{d\sigma}{d\Omega} = \frac{1}{N} \cdot \frac{dQ}{d\Omega} \cdot \frac{1}{Q}$$

Equation 4

where N denotes the number of target atoms per unit area.

If the collision between projectile and target can be modelled as a Coulomb interaction between the two positively charged nuclei, the differential cross-section is given by the Rutherford cross-section, which is defined as

$$\frac{d\sigma}{d\Omega} = \left(\frac{Z_1 Z_2 e^2}{16\pi\varepsilon_0 E} \right)^2 \frac{4}{\sin^4\theta} \frac{\left[\sqrt{1 - \left(\frac{M_1}{M_2}\sin\theta\right)^2} + \cos\theta \right]^2}{\sqrt{1 - \left(\frac{M_1}{M_2}\sin\theta\right)^2}}$$

Equation 5

in the laboratory frame of reference, where θ is the scattering angle.

E is the kinetic energy of the projectile ion, Z_1 and Z_2 are the atomic numbers of the projectile ion and target atom respectively, ε_0 is the dielectric constant and e denotes the elementary unit charge.

By looking at the range of the projectile ions it is thus possible with RBS to obtain quantitative information on the elemental composition in the near-surface of a sample. It is, however, only possible to detect and quantify elements that are heavier than the

projectile ions. Otherwise only forward scattering will occur and a detector at a large backscattering angle (e.g. 165°) will not collect any counts.

It is nonetheless possible to detect hydrogen with ion beam analysis techniques. Two methods are described below: elastic recoil detection (section 2.1.2) and nuclear reaction analysis (section 2.1.3).

2.1.2 Elastic Recoil Detection (ERD)

Elastic recoil detection analysis is in essence based on the same assumptions as RBS, i.e. energy and momentum transfer through scattering. However, rather than measuring backscattered projectiles at a high scattering angle, recoiling target atoms are detected in a forward scattering geometry. ERD uses high-energy ions with a mass greater than that of target atoms to be studied. A detector at a low scattering angle (e.g. 30°) then collects the recoiling atoms. The detector can be covered with a foil (e.g. some μm Ni or mylar) to ensure that only recoiling light elements are detected while the heavy projectile cannot penetrate the barrier.

The heavy ion projectile must have a mass greater than that of the target atom due to the scattering laws; hence, alpha particles are commonly used to obtain recoil spectra of hydrogen isotopes.

2.1.3 Nuclear Reaction Analysis (NRA)

The nuclear reaction $D(^{3}He, p)^{4}He$ allows quantitative measurements of the implanted D. The reaction has a broad resonance at an energy of around 640 keV for the incoming ^{3}He ions, as shown in Figure 8.
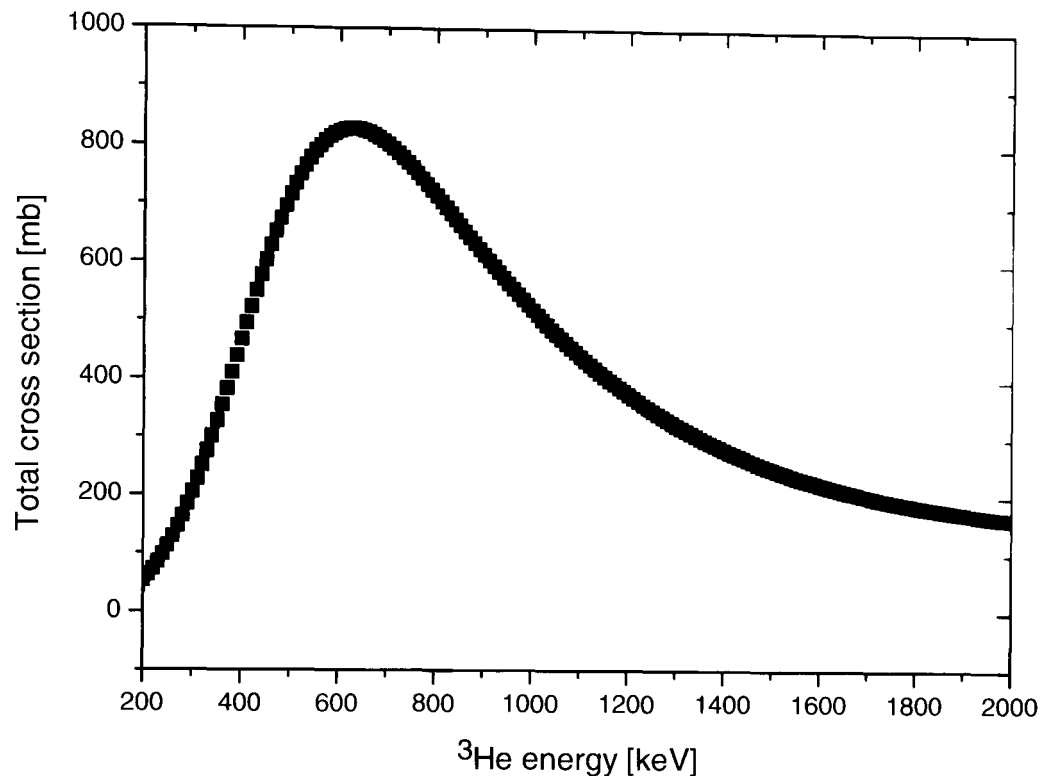
Figure 8: Cross section of the nuclear reaction $D(^{3}He, p)^{4}He$. The resonance around 640 keV allows the detection of deuterium with a ^{3}He ion beam.

Using two detectors at scattering angles of 135° and 105° allows the detection of the products of the reaction. If the 135° detector is covered by a 0.1 mm stainless steel foil only the high-energy protons from the nuclear reaction are observed, while the 105° detector is located such that it detects ^{4}He at a shallow exit angle. The 135° proton detector yields quantitative information on the amount of deuterium in the surface of the sample. A depth profile of the deuterium may be obtained through analysis of the ^{4}He detected at 105° due to the shallow exit angle and thus a longer path through the sample

[Rot80]. Using a 800 keV ^{3}He beam, the accessible depth in graphite is about 1500 nm [Fra89].

2.2 Photoelectron Spectroscopy

The chemical composition of the surface layer of a sample can be analysed using photoelectron spectroscopy. With these techniques electrons are emitted from the near-surface layer of a sample after excitation with photons. Depending on the energy of the photon source, core electrons or valence band electrons can be emitted. By using an X-ray source it is possible to excite core electrons, whilst an ultra-violet light source will only emit electrons with a small binding energy.

2.2.1 X-ray Photoelectron Spectroscopy (XPS)

Surface analysis by X-ray photoelectron spectroscopy (XPS) is achieved by irradiating a sample with monoenergetic, soft X-rays and analysing the energy of the detected electrons. The setup Artoss is equipped with a Mg K_α (1253.6 eV) X-ray source; the XPS system used for titanium and carbon systems is equipped with a monochromatic Al K_α (1486.6 eV) source. These photons have a limited penetration power of less than 10 μm in solids. They interact with atoms in the surface region, causing electrons to be

emitted through the photoelectric effect. The emitted electrons have measured kinetic energies given by

$$E_{kin} = h\nu - E_b - \phi_s \qquad \text{Equation 6}$$

where $h\nu$ is the energy of the photon, E_b is the binding energy of the atomic orbital from which the electron originates, and ϕ_s is the spectrometer work function.

The binding energy E_b denotes the difference in the total energy of a system in the ground state and the energy of the system after an electron has been removed.

The connection between the photon energy, the electron binding energy, and the kinetic energy of the photoelectron is shown in Figure 10.

The binding energy may be regarded as the energy difference between the initial and final states after the photoelectron has left the atom. Because a number of possible final states are available to the ions of each type of atom, there is a corresponding variety of kinetic energies of the emitted electrons. Moreover, a different probability (or cross-section) exists for each final state.

As each element has a unique set of electron binding energies, XPS can be used to identify the elements in the surface and determine their surface concentrations. Variations in the elemental binding energies - "chemical shifts" - arise from differences in the chemical potential of compounds. These chemical shifts can be used to assign the chemical state of the analysed sample.

Figure 9 shows typical spectra of the Be 1s binding energy region for clean, metallic beryllium and beryllium carbide (Be_2C).
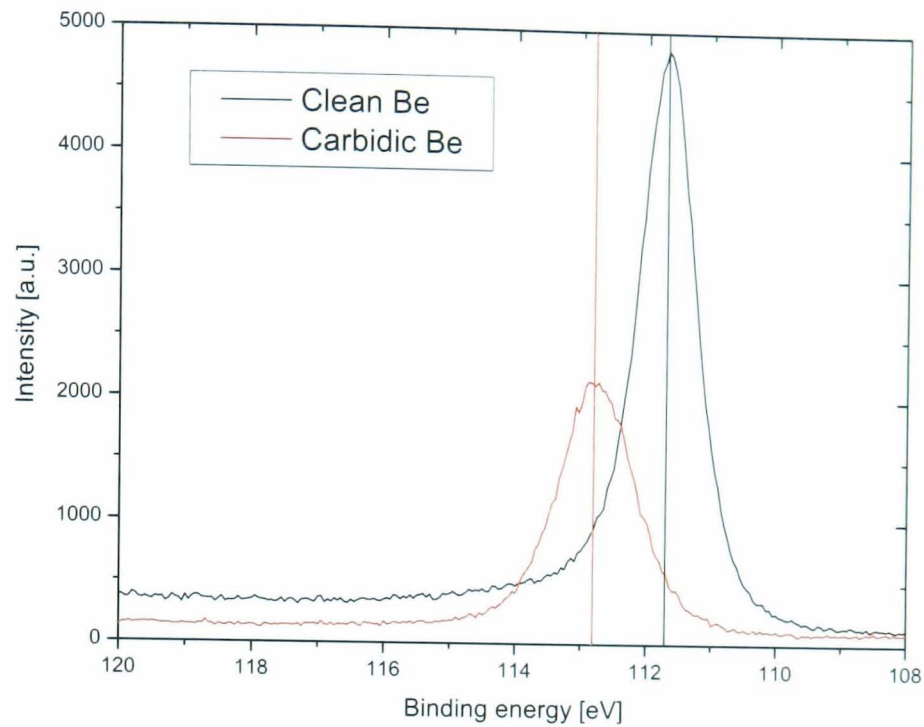
Figure 9: XPS spectra of beryllium: the shift in the binding energy peak of Be 1s electrons allows the identification of the chemical state of the surface layers on the analysed samples.

Probabilities of electron interactions with matter exceed those of the photons by far, so while the path length of the photons is of the order of micrometres, that of the electrons is only of the order of some nanometres.

Thus, whilst ionisation occurs to a depth of a few micrometres, only the electrons that originate within the top nanometres below the sample surface can leave the surface without energy loss through inelastic collision processes. Electrons that have lost energy before emerging from the surface form the underground of every photoelectron energy spectrum.

After leaving the sample, the kinetic energy of the electrons is detected by an electron spectrometer. The analyser is operated as an energy window, referred to as the "pass energy", accepting only electrons with an energy within this energy window. To maintain a constant energy resolution the pass energy is fixed; incoming electrons are adjusted to this pass energy window through a variable electrostatic field prior to entering the energy analyser. Hence a scan of the retardation voltage yields a spectrum of the number of electrons for a given pass-energy window as a function of the kinetic energy, and thus the binding energy, of the detected electron.

Energy scans across a wide binding energy range, e.g. 1200 eV to 0 eV in 0.2 eV steps, generate a survey spectrum showing electron contributions from all elements in the sample surface. To obtain chemical information on a particular element, scans of the appropriate binding energy region with a finer energy resolution (0.05 eV) are required.
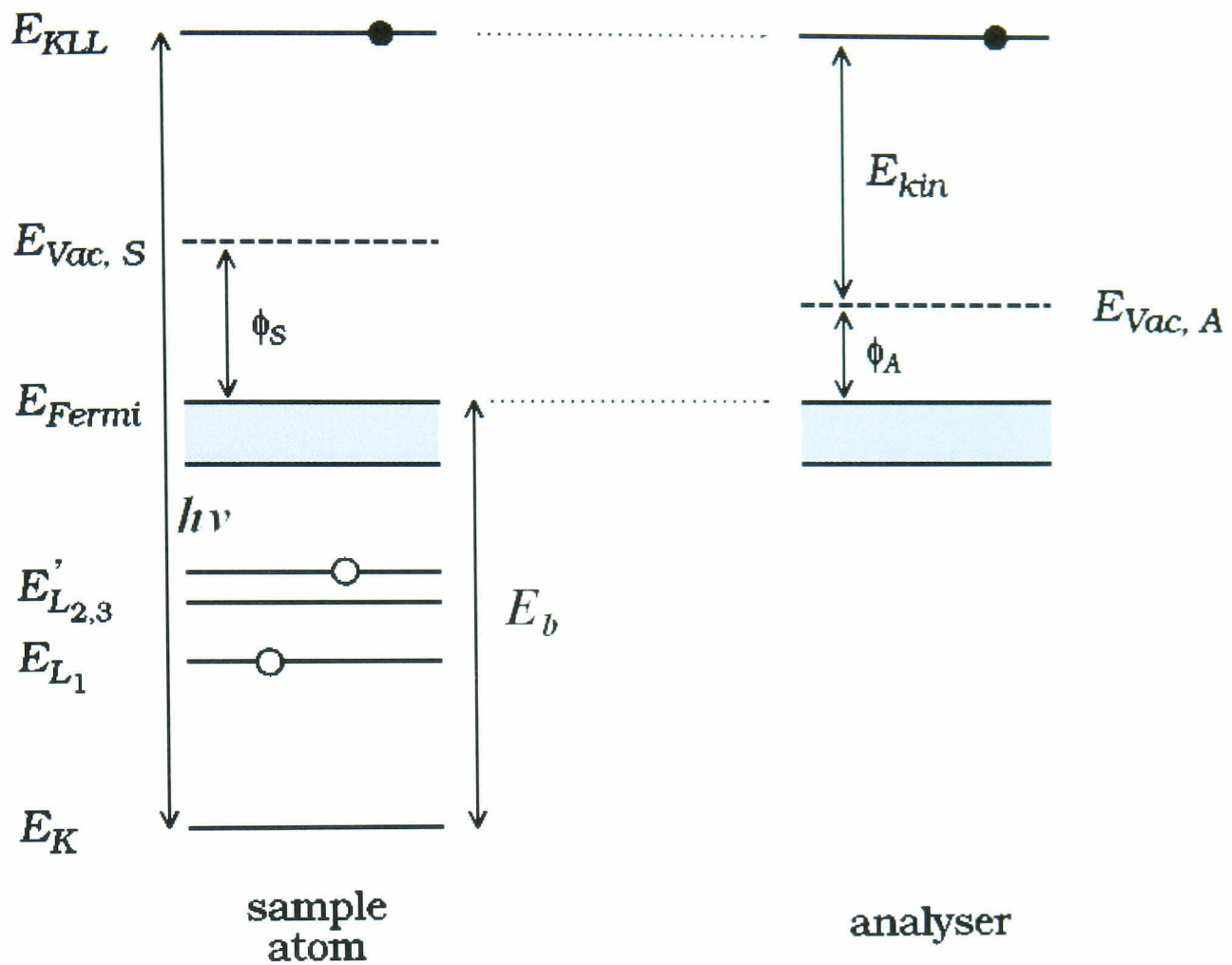
Figure 10: Schematic diagram of XPS processes.

To summarise, in the case of XPS the sample is irradiated by an X-ray source and the emitted photoelectrons are detected and analysed. The energy of emitted photoelectrons is given by equation 6.

Typically, a Mg K_α X-ray source with a photon energy of 1253.6 eV is used. As a result of a variation of the binding energy E_b due to a particular chemical reaction, XPS allows not only an identification of elements but also yields information on the chemical state of the elements within the analysis region.

The information depth accessible with XPS is limited owing to scattering of photoelectrons as they travel through the sample. Hence, for a depth d the attenuation of the emitted intensity I_0 is given by the Lambert-Beer-Law

$$I = I_0 \exp\left(-\frac{d}{\lambda}\right)$$
Equation 7

where λ is the inelastic mean free path of electrons. For $\lambda = 2\,\text{nm}$ this means that only 8% of the detected intensity originates from a depth greater than $5\,\text{nm}$.

Due to the random path that photoelectrons take on their passage to the surface of a sample, the attenuation length indicating the information depth of photoelectrons is smaller than their inelastic mean free path. The attenuation length is defined as the depth from the sample surface from which the intensity of the photoelectron signal is reduced to $\frac{1}{e}$. The attenuation of photoelectron intensity is described by D. Briggs and M. Seah [Bri83].

For a quantification of the atomic composition of a sample with XPS, the intensity of the observed elements within the attenuation-limited analysing depth is determined. With the measured intensities of each element the atomic concentration is calculated. For these calculations a homogeneous distribution of elements in the surface layer is assumed. The ratio of the concentrations of two elements A and B is determined by equation 8, where I_A and I_B denote the intensity of the signals, and S_A and S_B the sensitivity factors corresponding to the elements A and B. The sensitivity factors take into account the electrical and optical parameters of the setup, and depend both on elements and energy.

$$\frac{N_A}{N_B} = \frac{I_A/S_A}{I_B/S_B}$$

Equation 8

The concentration of A, C_A, is thus given by

$$C_A = \frac{N_A}{\sum_i N_i} = \frac{I_A/S_A}{\sum_i I_i/S_i}$$

Equation 9

The intensities of measured lines result from the integral of the area beneath a peak, weighted according to their respective sensitivity factors.

Studies of the carbon C 1s binding energy region with XPS [Lut01] have shown that the elementary carbon phase of graphitic carbon is composed of two contributions:

At a binding energy of 284.2 eV the C 1s electrons are arranged as in regular graphitic systems; and at a binding energy of 285.3 eV in carbon there is a "disordered" graphitic phase.

The disordered graphitic phase appears after the graphite has been bombarded with ions. Annealing leads to reordering of the carbon with a reduction of the disordered component.

2.2.2 Calculation of surface layer thicknesses using XPS

XPS provides, as discussed above, the capability of elemental surface analysis. The surface composition can also be determined in a quantitative manner. Upon deposition of e.g. a carbon surface layer on a substrate, the inelastic mean free path (IMFP) λ of

the photoelectron originating from the substrate is changed. The number of photoelectrons from the substrate reaching the detector, and therefore the substrate intensity, decreases according to the Lambert-Beer law (cf. equation 7).

The determination of the inelastic mean free path is subject to controversial discussions between A. Jablonski and C.J. Powell, B. Lesiak et al., S. Tanuma et al., W.S.M. Werner, and W.H. Gries [Jab99, Les89, Tan88, Tan91a, Tan91b, Tan97, Wer92, Gri95, Gri96]. The resulting values differ up to a factor of 2. Both the material properties (density, atomic volume) and fit parameters enter into the various calculations. A comprehensive survey on the different approaches and the resulting values has been compiled by A. Jablonski and C.J. Powell [Jab02].

In this work, the "universal equation" (equation 10) is used. It is based on a compilation of numerous experimental data of IMFPs, determined as a function of the excitation energy in the range of 1 eV to 1500 eV. For pure elements, λ (in nm) is calculated according to equation 10 by M.P. Seah and W.A. Dench (1979) [Sea79]. For experiments with inorganic compounds, this equation is slightly modified.

$$\lambda(E_{kin}) = \frac{538}{E_{kin}^{2}} a + 0.41 a^{3/2} E_{kin}^{1/2} \qquad \text{Equation 10}$$

In this equation, E_{kin} is the kinetic energy of the photoelectrons (in eV), and a is the atom diameter (in nm) of the attenuating material through which the photoelectrons travel. For the determination of the atomic diameter of carbon, here a density of the deposited carbon layers of 1.8 g cm^{-3} is used, which differs from the values for the density of graphite (2.2. g cm^{-3}) or diamond (3.51 g cm^{-3}). Measurements of carbon

layers, which were deposited by magnetron sputtering, resulted in a density of 1.9 g cm^{-3} [Mar84]. The resulting carbon layer thicknesses for the carbon layers deposited from the vapour phase and determined by XPS using a density of 1.8 g cm^{-3} agree well with the layer thicknesses which were determined independently by RBS, as described by [Gol00]. This observation justifies the determination of the carbon layer thicknesses by equation 10.

Generally, layer growth is assumed for the determination of the thicknesses of the deposited layers. From the XPS intensities measured for the substrate and film elements (I_S and I_F, respectively), the layer thicknesses can be determined according to equation 11 and equation 12 [Bri85]. Both the IMFP λ of the photoelectrons and the analysis angle of the photoelectrons θ are considered in the calculations. The values for λ correspond to the attenuation of the photoelectrons from the substrate by the film λ_S^F and to the attenuation of film photoelectrons, attenuated by the film itself λ_F^F.

$$I_S = I_S^\infty \exp\left(-\frac{d_F}{\lambda_F^S \cos\theta}\right)$$

Equation 11

$$I_F = I_F^\infty \left[1 - \exp\left(-\frac{d_F}{\lambda_F^F \cos\theta}\right)\right]$$

Equation 12

According to these equations, also the intensities of the respective elements for a clean substrate I_S^∞ and a clean, thick film I_F^∞ are necessary. However, it is impossible to determine both intensities during the course of a measurement series. Moreover, the substrate intensity at the beginning of the measurement cannot be used, because the sample needs to be moved to a different position within the chamber for the film

deposition. Due to this, the position of the measurement spot is varied and the absolute intensity is not comparable for all the measurements during the experimental series. Analogous arguments hold true for the intensity of a thick film. To solve these difficulties, the film thicknesses are not determined using equation 11 or equation 12, but by using the ratio of these equations (cf. equation 13). Therefore, for the calculation of the layer thickness, both the substrate and the film intensities are used.

$$\underbrace{\frac{I_F}{I_S}\frac{S_S}{S_F}}_{r} = \underbrace{\left[\exp\left(\frac{1}{\lambda_F^F \cos\theta}\right)\right]^{d_F}}_{m} - \underbrace{\left[\exp\left(\frac{1}{\lambda_S^F \cos\theta} - \frac{1}{\lambda_F^F \cos\theta}\right)\right]^{d_F}}_{n} \qquad \text{Equation 13}$$

$$m^{d_F} - n^{d_F} - r = 0 \longrightarrow d_F \qquad \text{Equation 14}$$

The solution of equation 14 and therefore the film thickness d_F is determined numerically (using Mathcad). The ratio of the unknown intensities for the clean substrate respectively the infinitely thick layer (I_S^∞ and I_F^∞) is replaced by the known sensitivity factors for the pure elements, cf. equation 15. These factors are determined with elemental samples and are tabulated for the used XPS system, taking into account the experimental settings, particularly the apertures of the analyser system (PC-ACCESS ESCA (1999)). Those factors are based on the photoelectron cross-sections for ionising core levels with Al K_α and Mg K_α radiation, respectively, for each element. The relation between the intensities I_S^∞, I_F^∞ and the sensitivity factors S_F and S_S is given by

$$\frac{I_S^\infty}{I_F^\infty} = \frac{S_S}{S_F} \qquad \text{Equation 15}$$

The analysis of the deposited layers is limited by the inelastic mean free path of the photoelectrons through these films. The intensity of the photoelectrons with element-specific kinetic energies is attenuated on their way through the material. The values for λ used in this work are given in Table 1 below. The maximum carbon layer for the detection of a substrate signal amounts to approximately 9 nm. For the Be signal, the relatively small sensitivity factor is of importance, as it limits the maximum carbon layer thickness at which a Be 1s signal can still be detected with a sufficiently large intensity. The sensitivity factors for the geometries used in the Artoss and XPS experiments, respectively, are also given in the table. Only for titanium (Ti) the sensitivity factors for 54° (non-monochromatic X-ray source, Artoss) and 90° (monochromatic X-ray source, XPS) are different.

XPS signal	λ [nm] Al K_α	λ [nm] Mg K_α	Sensitivity factor S 54° / 90°
C 1s (through C layer)	1.494	1.341	0.296
Be 1s (through C layer)	1.597	1.454	0.074
Be 1s (through Be layer)	1.365	1.243	0.074
Ti 2p (through C layer)	1.381	1.219	2.001 / 1.798
Ti 2p (through Ti layer)	0.536	0.471	2.001 / 1.798

Table 1: Inelastic mean free paths and sensitivity factors for the XPS (Al K_α) and Artoss (Mg K_α) setups.

2.2.3 XPS difference spectra

The shift in binding energy of some of the peaks with increasing exposure to ion bombardment is very small, as can be seen in Figure 11. The peak position corresponding to carbon in the titanium carbide phase (TiC) remains fixed, as there is no further chemical interaction between the carbon in the carbide phase and the implanted deuterium.

With the standard fitting parameters it is not possible to quantify this phenomenon in terms of changed parameters beyond the allowed margin of errors. However, the accuracy of the used apparatus permits the assumption that this shift is a result of chemical interactions with the implanted hydrogen isotopes and not only a statistical artefact.
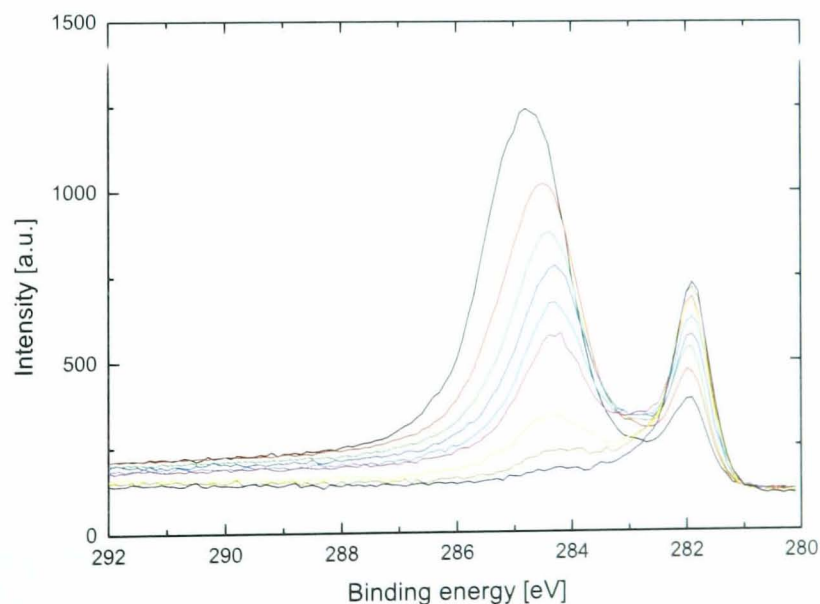
Figure 11: A clear shift in the position of the elementary carbon peak around 285 eV is visible, while the signal from carbon in TiC remains at its fixed position.

Subtracting the initial and final spectra shows the variation more clearly; Figure 12 and Figure 13 are examples of such difference spectra.
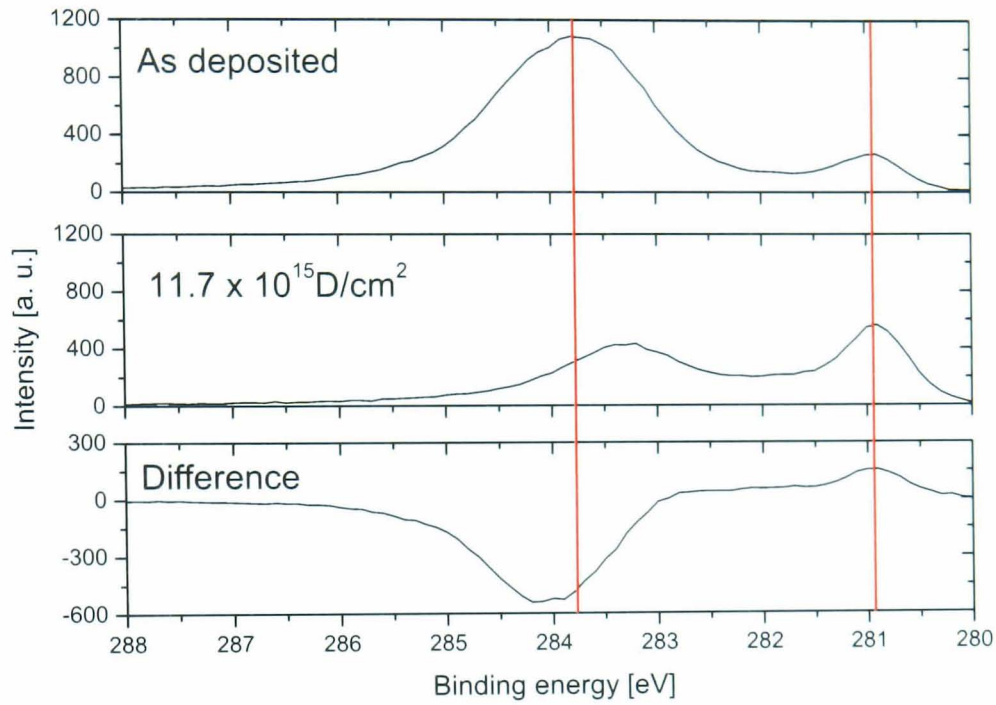
Figure 12: Difference spectrum of a carbon layer on titanium after deuterium ion bombardment.
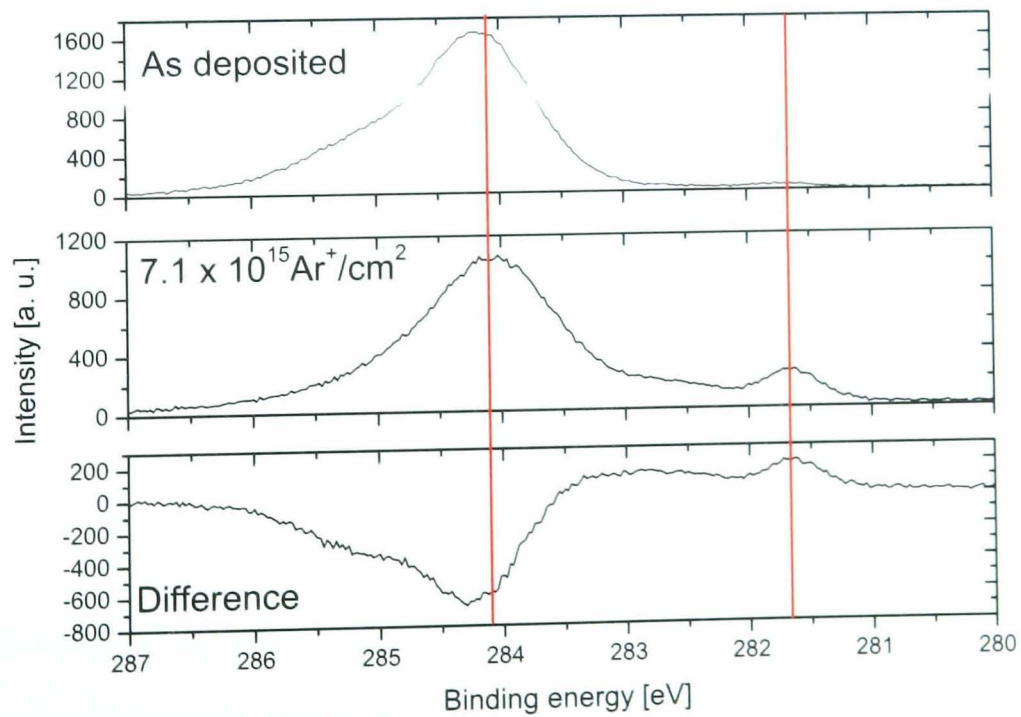
Figure 13: Difference spectrum of a carbon layer on titanium after noble gas ion bombardment with argon.

The study of chemical interactions due to electron binding energy shifts is not possible if the shifts are low compared to the accuracy of the parameters in the fitting procedure. This is particularly evident in the case of binding energy shifts due to interactions with hydrogen isotopes. Electrons from hydrogen itself are not discernible as a discrete peak in the electron binding energy spectrum. However, the comparison of binding energies after bombardment with deuterium ion with noble gas ions shows that small shifts in electron binding energy occur through deuterium ion bombardment.

2.3 Quadrupole Mass Spectrometry (QMS)

The term desorption describes the process of breaking a chemical bond (chemisorption) or releasing a trapped particle (physisorption) and removing an adsorbed particle from a surface. If the desorption energy results from thermal excitation of a sample, this mechanism is called thermal desorption and may be exploited for thermal desorption spectroscopy (TDS). Any particle that carries more thermal energy at a particular temperature than the desorption energy for this particular particle will be desorbed. It is thus possible to measure the binding energy of a particle through its temperature of desorption. For TDS measurements the temperature of the sample is increased and the number of desorbed particles is measured quantitatively as a function of time. If the temperature is increased through a constant ramp there is a linear relation between time and temperature which facilitates interpretation of measurements.

The desorption rate $R_d(t)$ may be described formally by the Arrhenius relation

$$R_d(t) = -\frac{dN}{dt} = v(\theta)\frac{N^m}{N_0^{m-1}}\exp\left[-\frac{E_d(\theta)}{k_B T}\right]$$

Equation 16

where k_B is the Boltzmann constant, T the temperature of the sample, $E_d(\theta)$ the activation energy for desorption. θ denotes the ratio of adsorbed particles N and the total number of surface particles N_0, and is thus a measure of the coverage of the surface of the sample. The order of the reaction m describes the dependence of the concentration of a particular particle on the desorption rate. It is not necessarily an integer if interactions take place between desorbed particles and the surface of the sample or between adsorbed particles. The pre-exponential factor $v_m(\theta)$ corresponds to the frequency of oscillations of adsorbed particles for first order reactions, and is of the order of 10^{13} s^{-1}. For higher order reactions corrections must be made to take interactions of the adsorbed particles into account.

In general, E_d, v_m and m are functions of θ, making the evaluation of TDS spectra very complex. Hence, for practical purposes a number of approximate solutions with simplified assumptions are used. Most methods for evaluating spectra assume that E_d and v are independent of θ for a fixed order parameter m.

An experimental setup that provides a direct line-of-sight between the implantation spot on the sample from an ion gun enables the measurement of particles that are directly re-emitted during implantation. Moreover, if the quadrupole mass spectrometer is equipped with a mechanical chopper that periodically interrupts the emitted particle beam, it is

possible in combination with a lock-in amplifier to distinguish particles that have traversed the direct line-of-sight from those that have had collisions with the wall of the experimental chamber [Vie82]. The differentiation of directly emitted species from those which have undergone collisions with the wall of the vacuum chamber is important, as wall interactions can lead to a change in the composition of emitted molecules through molecular recombination of the species.

3 Experimental setups

In this chapter the experimental setups which were used to carry out the measurements for this work are described.

The apparatus Artoss is an ultra-high vacuum (UHV) setup with facilities to clean and prepare samples, the possibilities for sample modifications through ion implantation and thermal treatment, as well as the availability to study the composition of a sample with ion beam analysis and chemical information through photoelectron spectroscopy (see section 3.1). An earlier design of this apparatus was dismantled and reconstructed with updated vacuum equipment, new vacuum chambers as well as a new vacuum pumping system. As part of the upgrade of the setup Artoss, facilities were installed for the detection and quantification of hydrogen isotopes in the near-surface of samples through ion beam analysis techniques with a new 3 MV tandem accelerator and the ability to study emission and desorption of particles with a line-of-sight quadrupole mass-spectrometer.

The XPS apparatus is a further UHV setup. This apparatus allows X-ray photoelectron spectroscopy with a monochromatic X-ray source for increased electron binding energy resolution (see section 3.2).

3.1 Apparatus: Artoss

The setup Artoss was designed to investigate the surfaces of prepared mixed-material systems and to study the effect of keV ion implantations on these surfaces in ultra high vacuum (UHV) conditions.

A previous setup of the apparatus was used to study the formation of carbides on beryllium [Gol00, Gol01]. To analyse the effects of hydrogen isotopes on the surfaces of mixed materials, an adaptation of the apparatus was required.

The apparatus consists of three chambers and a load lock; a schematic top view is shown in Figure 14. Chamber I holds the low energy ion source for implantation. Chamber II contains a bending magnet for mass separation of the low-energy ion beam. The ultra-high vacuum chamber III, the main target chamber, is equipped with the facilities for preparation and analysis of samples.
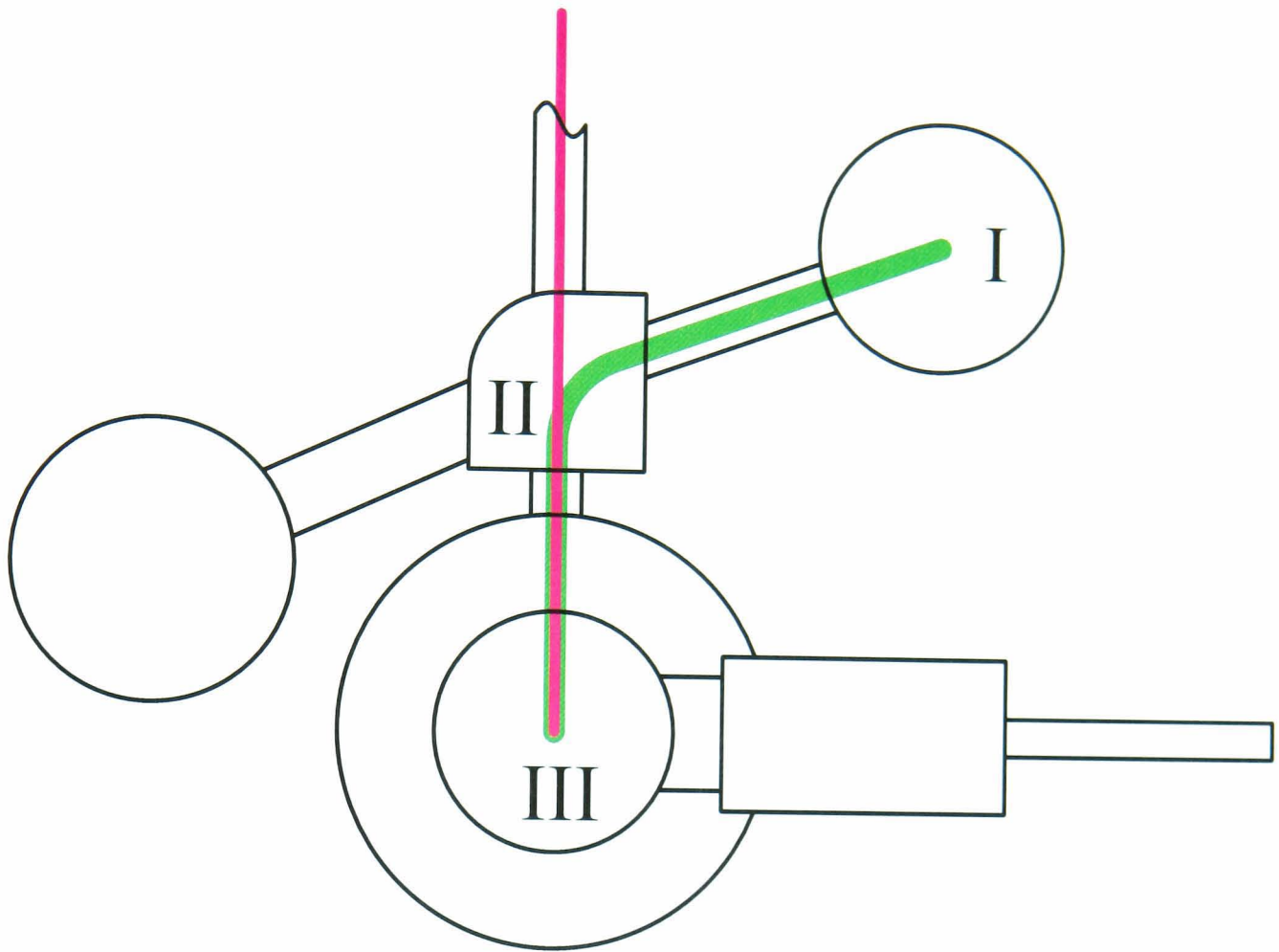
Figure 14: Schematic top-view of the setup of the vacuum chambers of Artoss:
- I: Ion source 1
- II: Bending magnet
- III: Main target chamber

3.1.1 Chamber I: Ion source 1

The ion source (IS 1) is used to generate an ion beam from gaseous precursor materials

for implantation and sputter cleaning of samples in chamber III. Ionisation is achieved

by electron impact from an incandescent filament. Ion energies can be set between

1 keV and 20 keV with an energy width of about 3 eV [Ara89]. Chamber I, the ion

source, can be separated from the bending magnet, chamber II, by a mechanical valve.

Ion lenses and steering plates allow shaping of the ion beam and directing it into the

bending magnet. A steering plate allows blanking of the beam by applying an appropriate voltage.

3.1.2 Chamber II: Bending magnet

In chamber II the ion beam from IS I is deflected through 80° by a bending magnet into the main target chamber III. Thus a mass separated, monoenergetic beam is available. The chamber is equipped with an ion pump (PHI Captorr 640 l/s) and a turbomolecular pump. The ion beam of a 3 MV tandem accelerator is guided through chamber II, with the bending magnet switched off. The chamber also acts as a differential pumping stage between the accelerator beam line (typical pressure 10^{-6} Pa) and the ion source chamber I and the UHV main target chamber III. The magnet current is controlled by a Hall probe with field controller (Bruker B-H 15) outside the vacuum chamber in the centre of the magnet.

The ion species constituting the ion beam can be selected through the bending magnet. Figure 15 shows the ion current constituents with argon, Figure 17 shows the ion current constituents with deuterium (m/q=4, D_2^+), argon (m/q=40 Ar^+; 20 Ar^{2+}), and impurities from a vacuum leak (m/q=28, N_2).
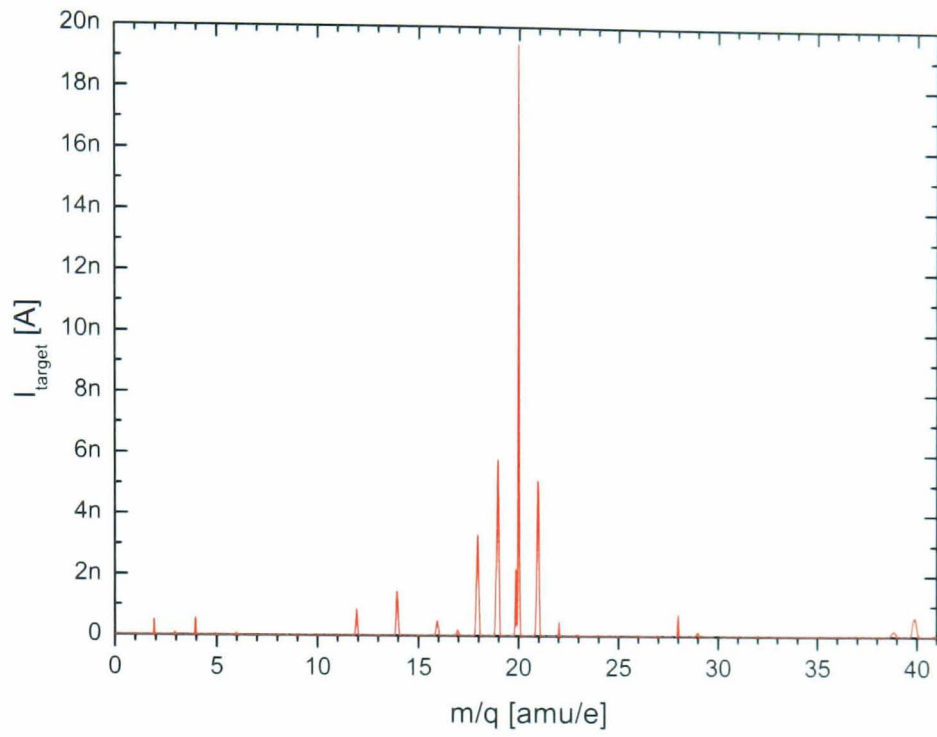
Figure 15: Mass to charge ratio of ions on the target: scan of the current in the bending magnet with argon as source gas.
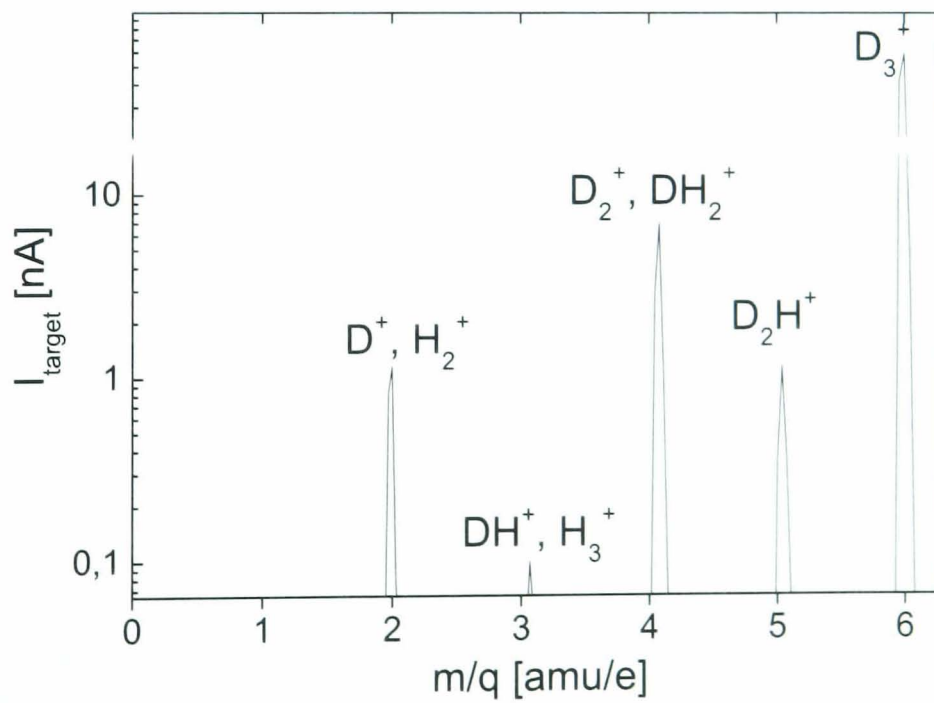
Figure 16: A scan of the magnetic deflection allows unique selection of particular isotopes from the general ion current generated in the ion source. The highest particle

flux was always achieved with D_3^+ ions, which equals ion bombardment of individual D ions with 1/3 of the kinetic energy.

Through deflection of the ion beam by 80° it is thus possible to select individual ion species for implantation. Operation of the ion source IS 1 with deuterium D_2 precursor gas and a voltage of 3 kV yields a current of 1 μA before mass separation. This current consists of all ions in the ion source vacuum chamber, and includes impurities both from the source gas supply and from the residual gas in the vacuum system. With suitable operation of the bending magnet it is possible to select the desired ion species, D^+, D_2^+, and D_3^+ with kinetic energies of 3 keV, 1.5 keV and 1 keV per deuterium nucleus, respectively (see Figure 16). The ion source in the Artoss setup provided the highest current with D_3^+ ions. Implantations were therefore performed with this ion species.
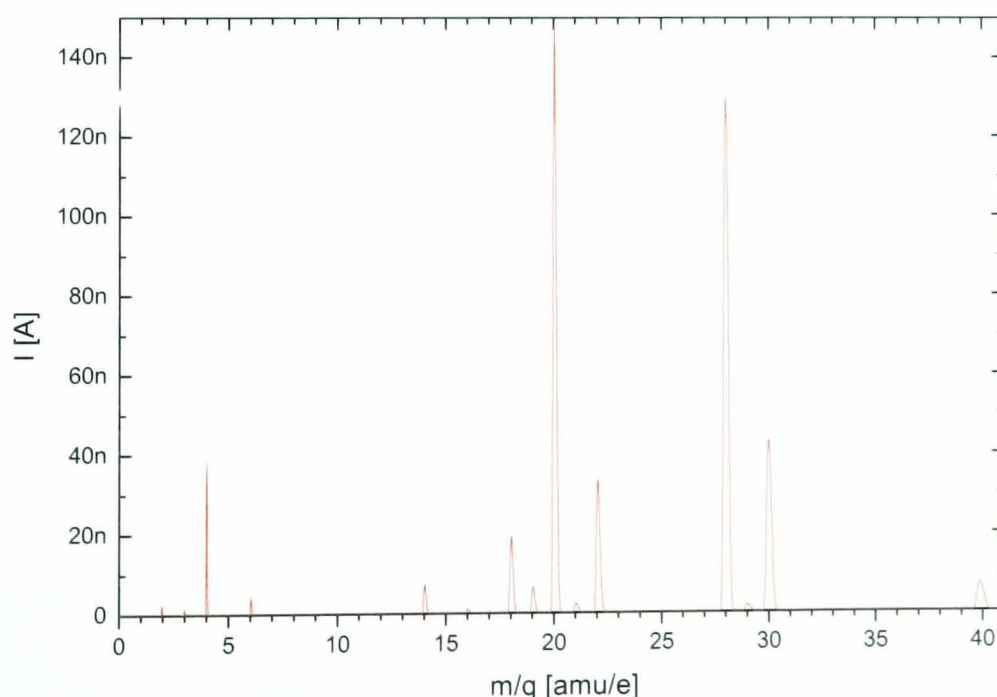
Figure 17: The ion source and bending magnet combination allow unique selection of individual ion species of up to great atomic masses exceeding that of argon (m/q=40).

Vacuum leaks in the ion source (e.g. m/q=28: N_2) are guided from the sample during standard operation.

3.1.3 Chamber III: Main target chamber

A schematic side view of the main target chamber is shown in Figure 18.

It is equipped with a turbomolecular pump to maintain a base pressure of less than 1×10^{-8} Pa after baking. To achieve these vacuum conditions baking of the experimental chambers at 150°C is required for several days.

With a titanium sublimator and a liquid nitrogen cooling trap the base pressure is reduced to below 3×10^{-9} Pa.
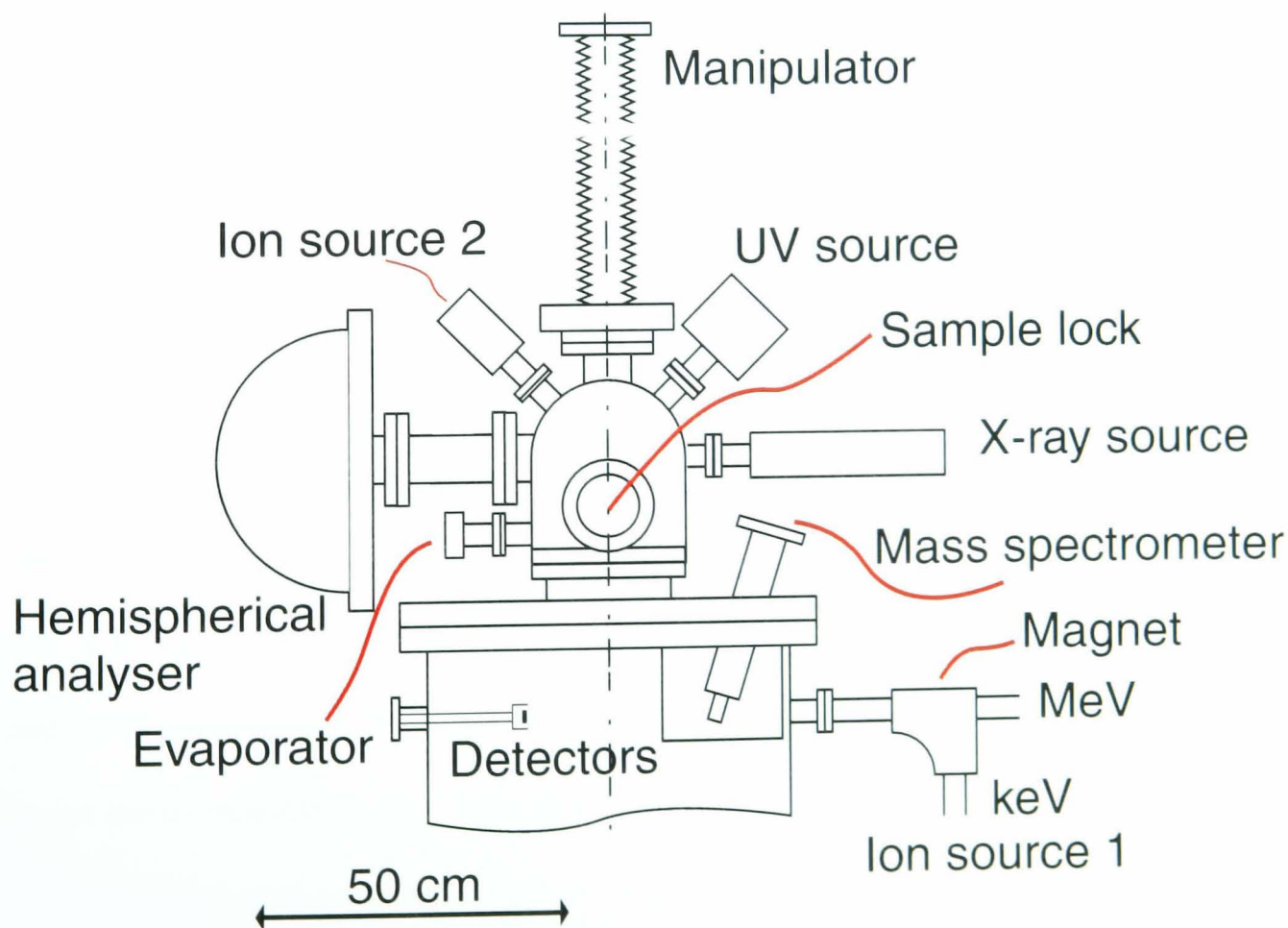
Figure 18: Schematic side-view of the main target chamber. The components are shown in one plane for the purpose of demonstration.

The keV (from IS 1) and MeV (from the tandem accelerator) ion beams are guided towards the sample in the centre of chamber III through an ion optical system. The system has two operational modes: it is used to focus the keV ion beams by electrostatic lenses, and to decelerate the keV ion beam from IS 1 down to energies below 100 eV. It is based on the design of H. Liebl *et al.* [Lie87] and has been optimised for the Artoss geometry using SIMION, a computer code [Dah95]. The keV or decelerated ion beams may be scanned across the sample with two pairs of deflection plates at the exit of the lens system. In addition, to prepare multi-component materials by ion implantation, the chamber can be backfilled with gases through a leak valve. For vapour deposition of solid materials, in particular carbon, an electron evaporation source (Omicron EFM3) is available.

In the plane of the beam lines from IS 1 and the 3 MV tandem accelerator four bakeable silicon surface barrier detectors (Eurisys Measurements) are installed at scattering angles of 165°, 135°, 105° and 30° for Rutherford backscattering (RBS), nuclear reaction analysis (NRA) and elastic recoil detection (ERD). The layout of these detectors is shown in Figure 19.

The detector at 165° was used for standard RBS analysis. Particularly the 135°, 105° and 30° detectors are well-suited for hydrogen isotope analysis. ERD at 30° detects target atoms recoiled by MeV ions (e.g. 2.7 MeV ^{4}He or 24 MeV ^{28}Si), while NRA at 135° and 105° allows depth profiling of deuterium through the $D\left(^3He,p\right)^4He$ reaction.

For precise sample current measurements, the sample is shielded by a double cylinder Faraday cup with dimensions large compared to the sample size. The outer cylinder is at ground potential. During ion beam analysis and implantation, the inner cylinder is biased with respect to the sample to collect secondary electrons and reflected charged particles. Therefore, the inner cylinder is included in the sample current measurement (Keithley 6517A electrometer or Ortec 439 digital current integrator).
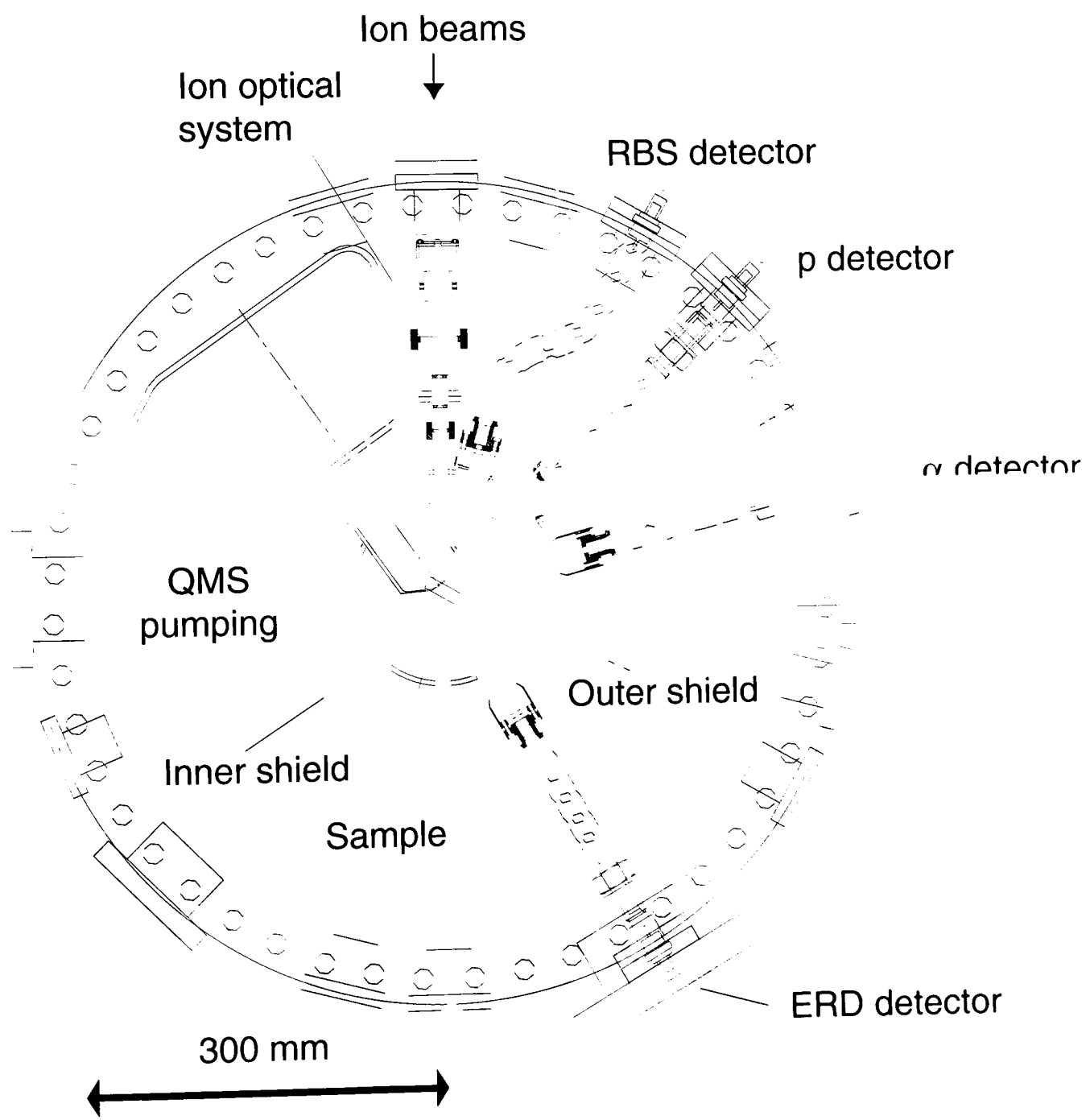
Figure 19: Installations in the ion beam analysis plane. Shown are the double cylinder Faraday cup, the QMS differential pumping stage, the ion optical lens and the surface barrier detectors.

Further techniques to study the hydrogen isotope inventory and interaction with multi-component materials are available with a line-of-sight quadrupole mass spectrometer (adapted version of Balzers QMG 422). The ioniser is located in the ion beam plane to ensure a direct line-of-sight. The mass spectrometer is housed in a differential pumping stage within the main chamber III, pumped by two sequential turbomolecular pumps to increase the compression for light particles, in particular hydrogen isotopes. A movable cone with an entrance aperture of the size of the sample diameter (12 mm) is placed directly in front of the sample during thermal desorption spectroscopy (TDS) or direct re-emission measurements.

Ion implantation and ion beam analysis techniques are not obstructed by the differential pumping chamber or the QMS cone during standard operation.

The differential pumping stage lowers the background pressure around the mass spectrometer, which is particularly important during direct re-emission measurements. In these experiments, the sample is implanted by an ion beam through the ion optical lens system via a channel in the collector cone, while the mass spectrometer detects particles emitted from the sample. To discriminate directly-emitted particles from background particles, a tuning-fork chopper interrupts the particle flux from the sample periodically with a frequency of approximately 8 Hz.

The mass spectrometer signal is detected by a lock-in amplifier. For TDS measurements, the chopper does not obscure the line-of-sight between the sample and the ioniser of the quadrupole mass-spectrometer. When not in use, the bottom plate of the differential pumping stage with the collector cone is opened and the cone does not obstruct the ion beam analysis equipment.

Above the ion beam analysis plane, surface analysis and preparation equipment is installed in a second plane. For sample cleaning by sputtering and for XPS sputter depth profiling, a second ion source IS 2 (Specs IQ 12/38) is available. Up to four different gases are available simultaneously and are dosed by means of a leak valve. The chamber is equipped with two photon sources:

An ultra-violet source (VSI/Specs UVS 300) for valence band spectroscopy (ultra-violet photoelectron spectroscopy, UPS) employing He I (21.2 eV) and He II (40.8 eV) radiation, and an X-ray source (PHI, model 04-548) with Al (1486.6 eV) and Mg (1253.6 eV) anodes for core level spectroscopy (X-ray photoelectron spectroscopy, XPS).

The ion source and both photon sources are confocal with the entrance lens system (PHI Omni Focus III) of the hemispherical electrostatic analyser (PHI, model 10-360). The hemispherical analyser is equipped with a multi-channel detector for fast data acquisition. The analyser allows detection of electrons as well as positively charged ions. Thus, not only photoelectron spectroscopy is possible with this set-up, but also low-energy ion scattering spectroscopy (ISS) with monolayer surface sensitivity is available.

The sample may be positioned with the computer-controlled manipulator in all three dimensions, as well as rotated about the vertical axis. On the lower end of the manipulator a Faraday cup (aperture 0.5 mm) is mounted to enable the determination of the intensity, the precise position as well as the profiles of the ion beams. Three permanently mounted reference materials (gold, silver, and highly oriented pyrolytic graphite) are used for energy calibration. Samples can be heated by a filament which is mounted on the sample holder, and also cooled through a liquid nitrogen reservoir which is mounted to the manipulator.

The samples are mounted on a transferable support which also contains a filament for electron bombardment heating, contacts for thermocouples (chromel-alumel) and a separate connection for sample current measurements. The whole unit can be transferred from the load lock to the central manipulator. Therefore, filament exchanges or broken thermocouples can be repaired without breaking the vacuum in the main chamber. Sample temperatures between below 200 K and above 1000 K are easily accessible. The cooling system is particularly useful during TDS experiments to bring the sample back to low temperatures after a desorption run.

The sample transfer into the main vacuum chamber passes through a differentially pumped load lock. The base pressure in the load lock after extended pumping is below 5×10^{-7} Pa.

3.2 Apparatus: XPS

To achieve higher precision in electron binding energies an XPS set-up

(PHI ESCA 5600) was used.

This setup is equipped with a monochromatic X-ray source, which yields an increased

energy resolution of below 0.29 eV [Mil97].

The increased energy of the XPS setup is shown in Figure 20.
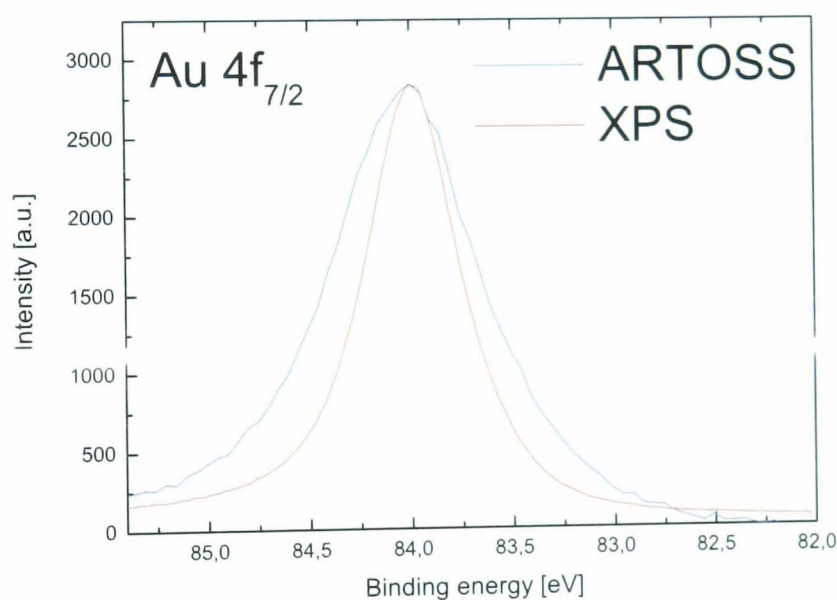
Figure 20: The XPS-setup provides enhanced energy resolution over the Artoss-setup
due to a monochromatic X-ray source.

4 Computer simulations

The deuterium ion bombardments were simulated using the Monte-Carlo simulation code TRIDYN which models the collisional transport of energetic ($v \gg v_{therm}$) projectiles in amorphous materials. Comparing the measured data to the simulations which only take collision-induced processes into account, yields further information on the possible occurrence of chemical reactions during erosion of the carbon surface layers.

The TRIDYN simulation code by W. Möller and W. Eckstein [Moe84, Eck91] is an extension of the TRIM-SP code by Biersack and Eckstein (Bie84), which is based on the TRIM ("Transport of Ions in Matter") code by J. Biersack and L. Haggmark [Bie80] to calculate the trajectories of ions in materials. Particle trajectories in TRIM calculations are followed using the binary collision model between the projectile and the sample atoms. Recoils generated during these collisions are followed in the same manner; thus TRIM models the entire collision cascade induced by the incident particle. The collision cascade is followed until the entire energy of the incident particle and of any generated recoil has been deposited due to inelastic energy loss through interaction with the target electrons. The inelastic energy loss is simulated in TRIDYN using the Lindhardt stopping formula [Lin61] which is well suited for projectile energies below 25 keV/amu, as is the case in this work.

While in TRIM the target is considered to be static the TRIDYN code additionally includes a dynamic adaptation of the bombarded material due to deposition of implanted ions as well as physical sputtering of surface atoms.

The target sample is divided into layers of equal thickness. Layer thicknesses are free to vary due to particle implantation from the ion beam as well as erosion processes through kinematic collisions. The ion beam is modelled by pseudo-particles (consisting of a number of particles) and after the collision cascade of each pseudo-particle the composition of the target system is re-evaluated, taking into account kinematic effects of implantation and sputtering. Diffusion, segregation and chemical erosion are not taken into account; it is thus possible to identify these effects by comparing kinematic simulations with the experiment.

5 Experimental procedures

The study of the elementary composition and chemical states of mixed materials with chosen prepared composition in ultra-high vacuum requires careful planning. The analysis of clean beryllium systems must be carried out in quick succession to avoid surface contamination from residual gas even in ultra-high vacuum.

To achieve the implantation fluences for these measurements with a deuterium (D_3^+) ion current of 100 nA, it was possible to perform up to 20 successive implantations with sample analysis after each implantation step in one day.

5.1 Preparation of multi-component surface layers

Samples may be cleaned by noble gas sputtering from IS 2 at keV ion energies, also during sample annealing. In a beryllium single crystal it is possible to reduce the oxygen impurity to less than 10^{14} cm^{-2} by Ar^+ and He^+ ion bombardment [Gol00]. Multi-component surface layers can be created through vapour deposition with the electron beam evaporation source as well as by implantation of ions with energies ranging from below 100 eV (operating the electron optical system in deceleration mode) to 20 keV using IS 1. During deposition of carbon from a high-purity (99.999 %) source the pressure does not exceed 5×10^{-8} Pa.

The ion implantation experiments on beryllium by P. Goldstraß [Gol00] used carbon dioxide CO_2 (Linde 4.5) as source gas both for C^+ and CO^+ ions. Using carbon monoxide CO as source gas gives larger beam currents. However, the CO in the residual gas leads to adsorbed C and O (both up to 4%) on the Be surface.

The mixed materials in this work were created by carbon vapour deposition on cleaned metallic surfaces.

5.2 Measurement strategy
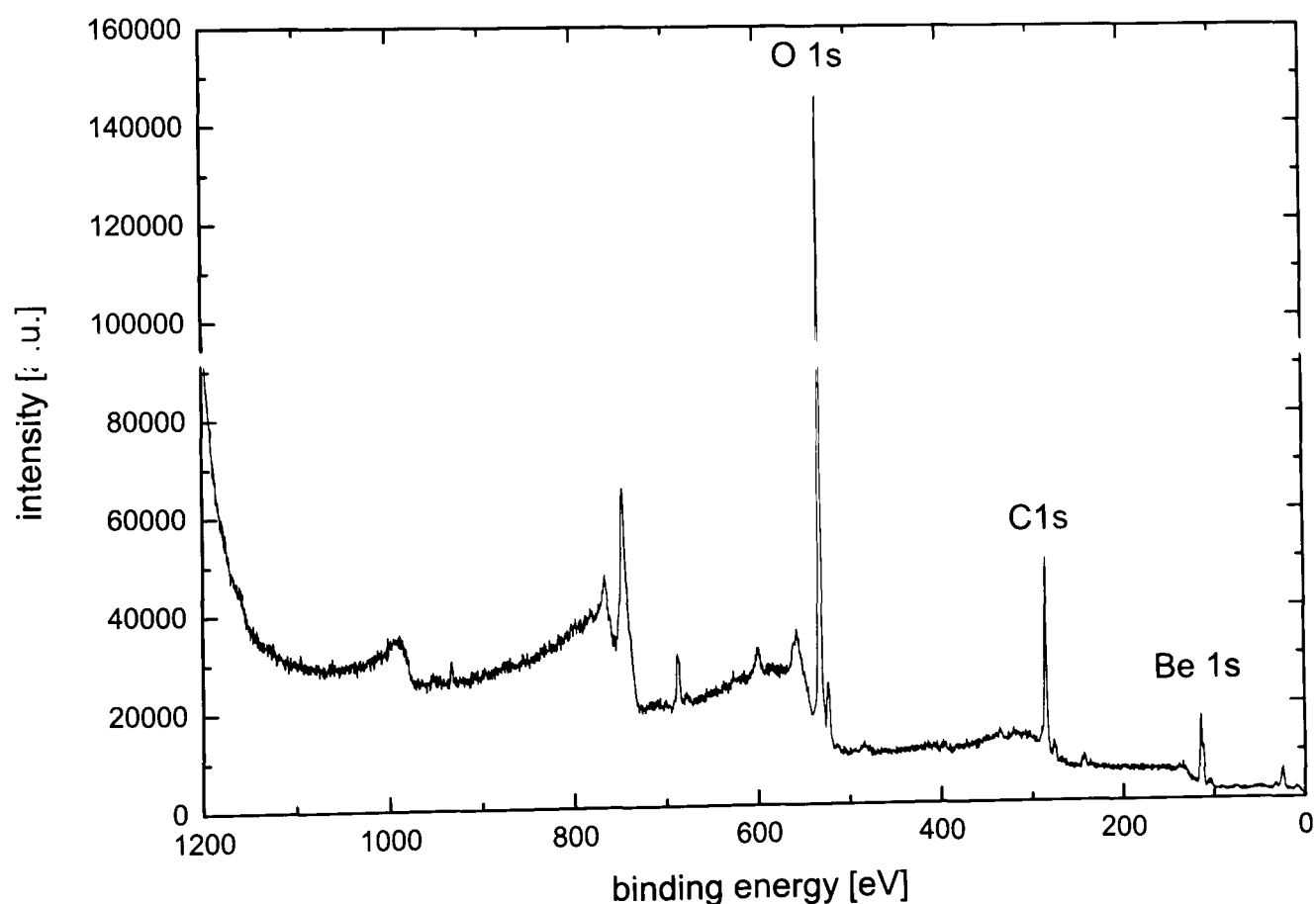
Figure 21: Beryllium XPS survey spectrum after introduction into the ultra-high vacuum system before cleaning through noble gas sputtering. Impurities of oxygen and carbon are clearly visible.

After exposure to atmospheric conditions, XPS analysis of beryllium samples exhibits

an oxygen- and carbon-containing surface layer, shown in Figure 21. The XPS analysis

after noble gas sputtering (Figure 22) clearly shows a dominant signal from beryllium

(Be 1s) photoelectrons, with impurities of carbon and oxygen reduced to below one

monolayer.
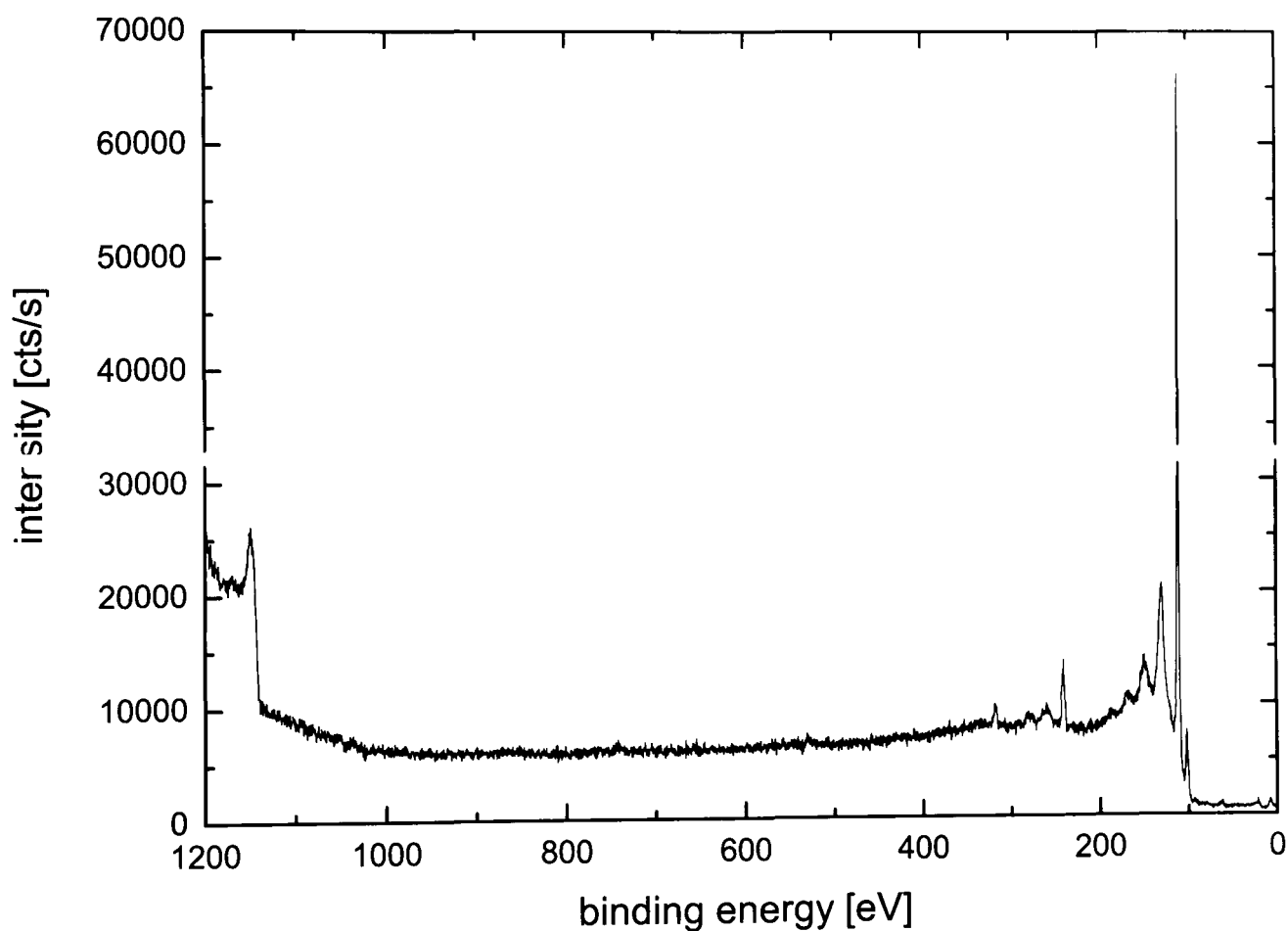
Figure 22: A survey spectrum of a cleaned beryllium sample shows no oxygen impurity.
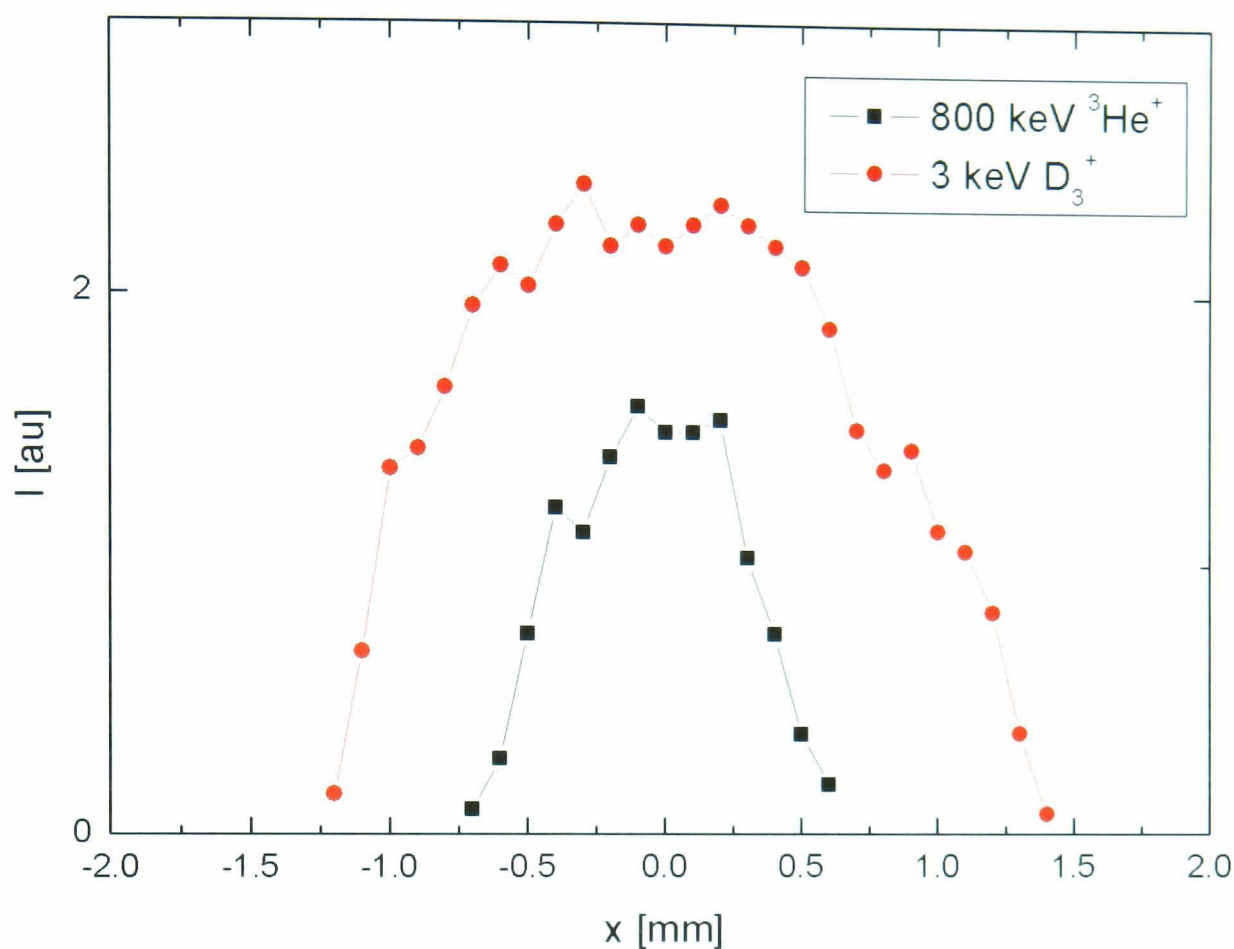
Figure 23. The profiles of the ion beams for implantation from IS1 and measurement from the accelerator were chosen such that accelerator analysis was always possible within the implanted region.

Series of deuterium implantation and analysis cycles were always carried out within one day, without any interruption. With a deuterium ion current of 200 nA it is possible to perform up to 15 cycles of implantations and accelerator-based analysis, or less than 10 cycles of implantations and XPS analysis in one day. The ion beam profiles were selected such that the [3]He ion beam for RBS and NRA was always within the deuterium implanted area (Figure 23).

The oxygen impurity from residual gas at 5×10^{-9} Pa from a 15-hour pause made it impossible to continue implantation series the following morning.

During deuterium ion bombardment, the oxygen impurity concentration was not increased while measurement series were carried out.

5.3 Analysis

The setup of Artoss allows *in situ* analysis with a variety of techniques which have been chosen to investigate various properties of multi-component surface layers. Previous analysis has concentrated on X-ray and ultra-violet photoemission spectroscopy (XPS, UPS) as well as ion beam techniques.

While XPS is very sensitive in the top few monolayers, the range of RBS is considerably deeper, ranging from several hundred nm to some μm, depending on ion species and primary energy. With RBS it is, however, not possible to obtain information on very thin surface layers which XPS can detect. Therefore, XPS and RBS not only complement each other in elemental and chemical state information, but also with respect to quantitative analysis. XPS is sensitive at very low coverages down to small fractions of a monolayer. Up to several monolayers, both methods provide quantitative information with similar accuracy and this coverage region allows a comparison and calibration of both methods.

At surface layers with thicknesses well above the inelastic mean free path of the photoelectrons (some nm), RBS is still able to probe the layer thickness with large accuracy. Figure 24 shows a comparison of both methods for carbon films deposited on beryllium. Below the inelastic mean free path of the photoelectrons (depicted in Figure 24 as horizontal lines for Be 1s and C 1s photoelectrons) both RBS and XPS results agree well. For thicker carbon layers, RBS is the method of choice, since for XPS not only do inelastic mean free paths limit the information depth, but the layer morphology is also crucial for quantification of thick layers.

The combination of XPS and RBS has been applied successfully to characterise mixed carbidic and oxidic surface layers on beryllium [Gol00]. However, with RBS backscattering only occurs if the target atom is heavier than the projectile, and XPS is not sensitive to the s state electrons of hydrogen and helium. It is therefore not possible to detect hydrogen or helium with this technique.
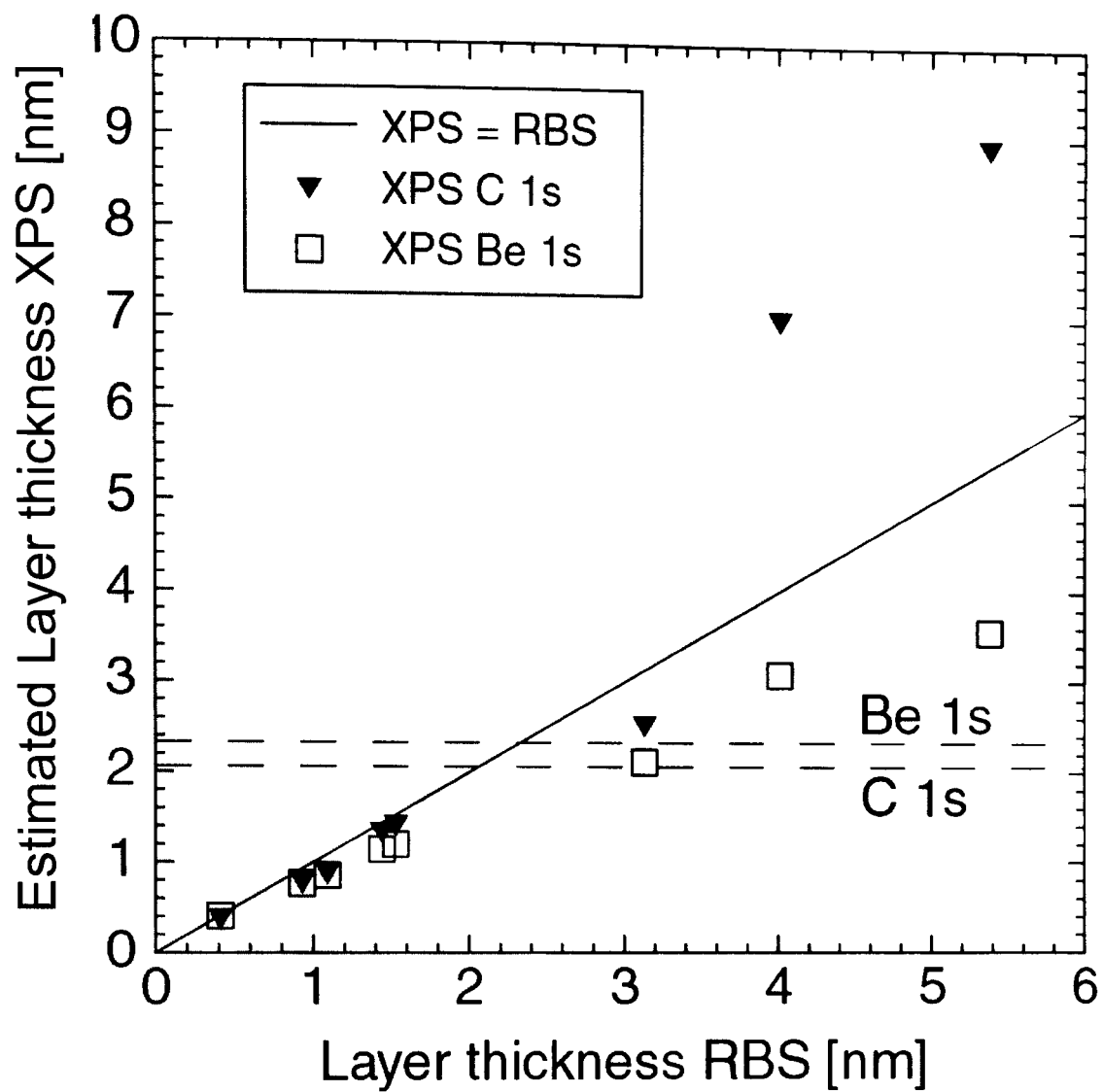
Figure 24: Carbon layer thickness obtained from the XPS C 1s and Be 1s signals versus the thickness from the RBS signal. The broken lines indicate the inelastic mean free paths of C 1s and Be 1s photoelectrons in carbon.

6 Results

This chapter contains the results of the experimental series that were performed in the experimental setups Artoss and XPS. Measurements were carried out in sequential series of deuterium ion implantation and subsequent analysis through accelerator based ion beam analysis (as described in section 2.1), or X-ray photoelectron spectroscopy (section 2.2).

Presented in this chapter are the measurements of ion bombardment of

- Highly-oriented pyrolytic graphite, a particularly clean form of graphitic carbon (section 6.1)
- carbon layers on polycrystalline titanium (section 6.2)
- carbon layers on single-crystalline beryllium (section 6.3)
- single-crystalline beryllium (section 6.3)

All experimental series were conducted with varying ion fluences; both survey spectra to observe general features, and high-resolution spectra to detect details, were taken.

Two types of ions were used: deuterium, as this is of interest in nuclear fusion, and argon, to highlight the effects of chemical reactions between the hydrogen isotope and the materials.

The data collected in the first series (using HOPG) not only yielded results that were interesting in their own right, but also provided useful reference for later experiments, where carbon-coated titanium and beryllium were used.

Figure 27 shows difference spectra of highly-oriented pyrolytic graphite bombarded with D^+ ions. The peak position in the spectrum at 284.2 eV indicates elementary carbon. The contribution at 282.6 eV stems from carbon in the beryllium carbide state (Be_2C) at the interface with the beryllium substrate.

A small chemical impurity in the form of oxygen is observed at 531 eV in Figure 22 after noble gas sputtering. The oxygen impurity of less than half of one monolayer was present due to the residual gas in the UHV vacuum of 5×10^{-9} Pa. During the vapour-deposition of carbon, a pressure rise to 5×10^{-8} Pa was caused by the heating of a tungsten filament and a graphite rod in the vapour-deposition source. No further contamination through an increase in the oxygen contribution was observed during carbon vapour-deposition or deuterium ion implantation.

In atmospheric conditions, the surfaces of beryllium samples are always covered by oxide layers through oxygen impurities from the air. Figure 21 shows a typical XPS spectrum of beryllium after introduction into the ultra-high vacuum system from atmospheric conditions.

After introduction of a beryllium sample into the vacuum chamber, the oxide layer covers on the surface of the beryllium crystal can be removed through physical

sputtering. To achieve elementary beryllium surfaces without chemical impurities, sputtering with chemically inert noble gases of some keV is an appropriate technique.

Figure 21 shows the surface composition of an uncleaned beryllium specimen. After a series of bombardments with noble gas ions it was possible to obtain a beryllium surface with less than 0.5 monolayers oxygen as the only chemical impurity observable in XPS spectra (Figure 22).

Series of successive deuterium implantations and measurements were carried out with accelerator-based techniques (RBS/NRA) and XPS. The accelerator based techniques yield quantitative information on the retention of implanted deuterium as well as the erosion of the carbon surface layer. The XPS spectra show the chemical state of the system, indicating the formation of beryllium carbide Be_2C.

To study the retention of deuterium in beryllium, a series of implantations and NRA spectra was performed.

X-ray photoelectron spectroscopy yields very precise information on the creation of chemical interactions between the various substances of a sample due to external application of energy through heating or ion implantations. It is thus possible to investigate the formation of a metal carbide phase through ion bombardment of carbon layers on metals.

However, XPS is not sensitive to hydrogen isotopes or the effect of chemical bonds between hydrogen and a substrate.

The formation of a carbidic phase between carbon and a metal substrate thus leads to peak shifts of several eV, whilst chemical phases consisting of carbon and hydrogen isotopes merely produce minute shifts of peaks of photoelectrons plotted as functions of electron binding energy. To distinguish these small shifts in binding energy, the difference of signals was established, which indicated decreases and increases in intensity and thus allowed the identification of interactions with hydrogen ions, after comparison with analogous implantations with noble gas argon ions.

6.1 Graphite

The hydrogen ion bombardment of carbon was analysed through deuterium ion bombardment of highly oriented pyrolytic graphite (HOPG), which contains well-aligned layers of carbon in the graphitic sp^2 phase. HOPG is a particularly clean form of graphitic carbon. The sample is simply cleaned by removing some surface layers, which hold the surface impurities with a sticky tape before introduction into the vacuum chamber. Thus, cleaning of the sample does not require ion bombardment, which would lead to disordering of the graphitic carbon structure.

A highly oriented pyrolytic graphite (HOPG) sample is bombarded with 1 keV D^+ ions up to fluences of 2.3×10^{16} cm^{-2}. After each ion bombardment cycle, XPS spectra are

taken both in survey and high-resolution modes. Survey spectra prove no contamination accumulation at the sample surface during all treatment steps, since only peaks attributable to carbon are observed (see Figure 25).
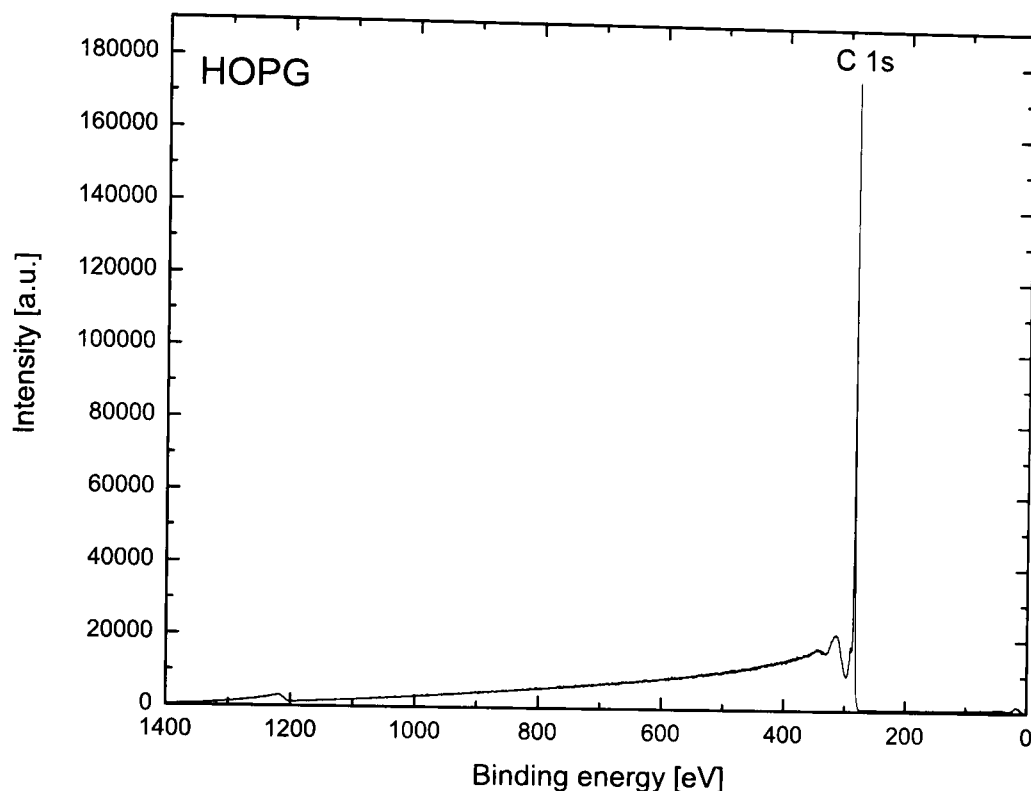
Figure 25: Survey spectrum of clean HOPG.

Already after a D^+ fluence of 1×10^{15} cm^{-2} the C 1s peak shows a shift in its overall maximum of 0.1 eV to lower binding energies (from 284.2 to 284.1 eV). After an implanted deuterium fluence of 2.3×10^{16} cm^{-2}, the shift amounts to 0.15 eV and after annealing at 700 K the peak maximum is at 284.0 eV. In contrast to Ar^+ bombardment measurements of thin carbon layers on gold [Lut01a] where the disorder introduced by the ion beam and the remaining graphitic peak can be separated unambiguously by peak fitting, this procedure is not possible here. Nonetheless, to gain information on the additionally introduced binding states of carbon under D^+ irradiation, the C 1s spectrum from clean, unirradiated HOPG is subtracted from the respective bombarded spectra

after Shirley background removal. This background is the result of inelastic electron scattering processes and leads to a gradual increase in the base line of the signal at higher binding energies [Shi72].
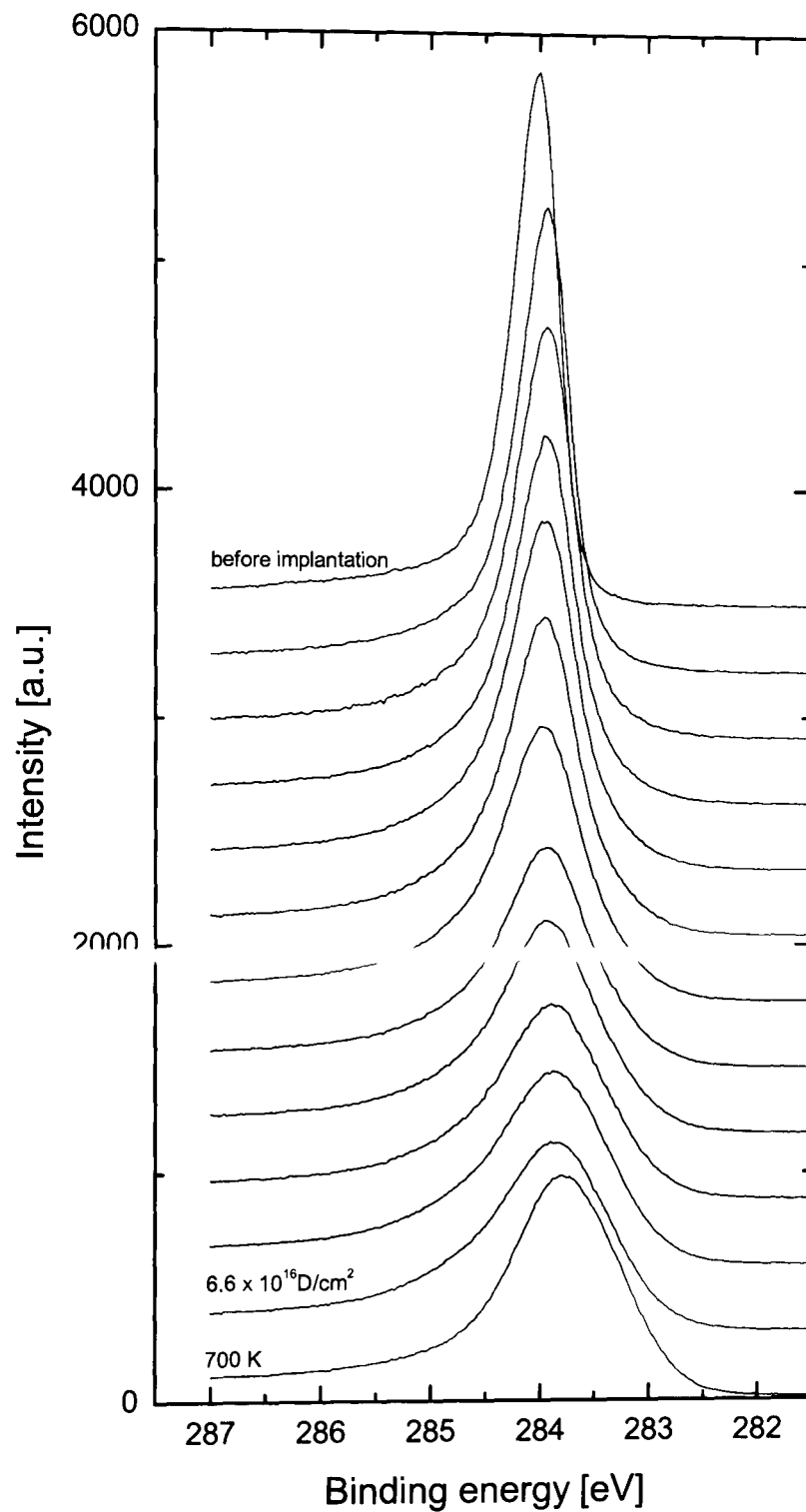
Figure 26: XPS spectra in the C 1s region of HOPG showing increasing fluences of D⁺ ion bombardment at 1 keV.

The difference spectra are plotted in Figure 27 in two groups for better visibility. The upper group consists of the first six implantation steps between 1.0 and 4.7×10^{15} cm^{-2}. The lower group comprises the following five implantation steps from 6.6 to 23×10^{15} cm^{-2} together with the final annealing experiment at 700 K for 30 min. Solid and broken lines alternate with increasing fluences; the first and last curves in the groups are marked in the plot. Positive intensity differences (values above the zero lines) in these spectra denote additional intensity compared to clean HOPG, whereas negative values show decreased intensity at the respective binding energy region.
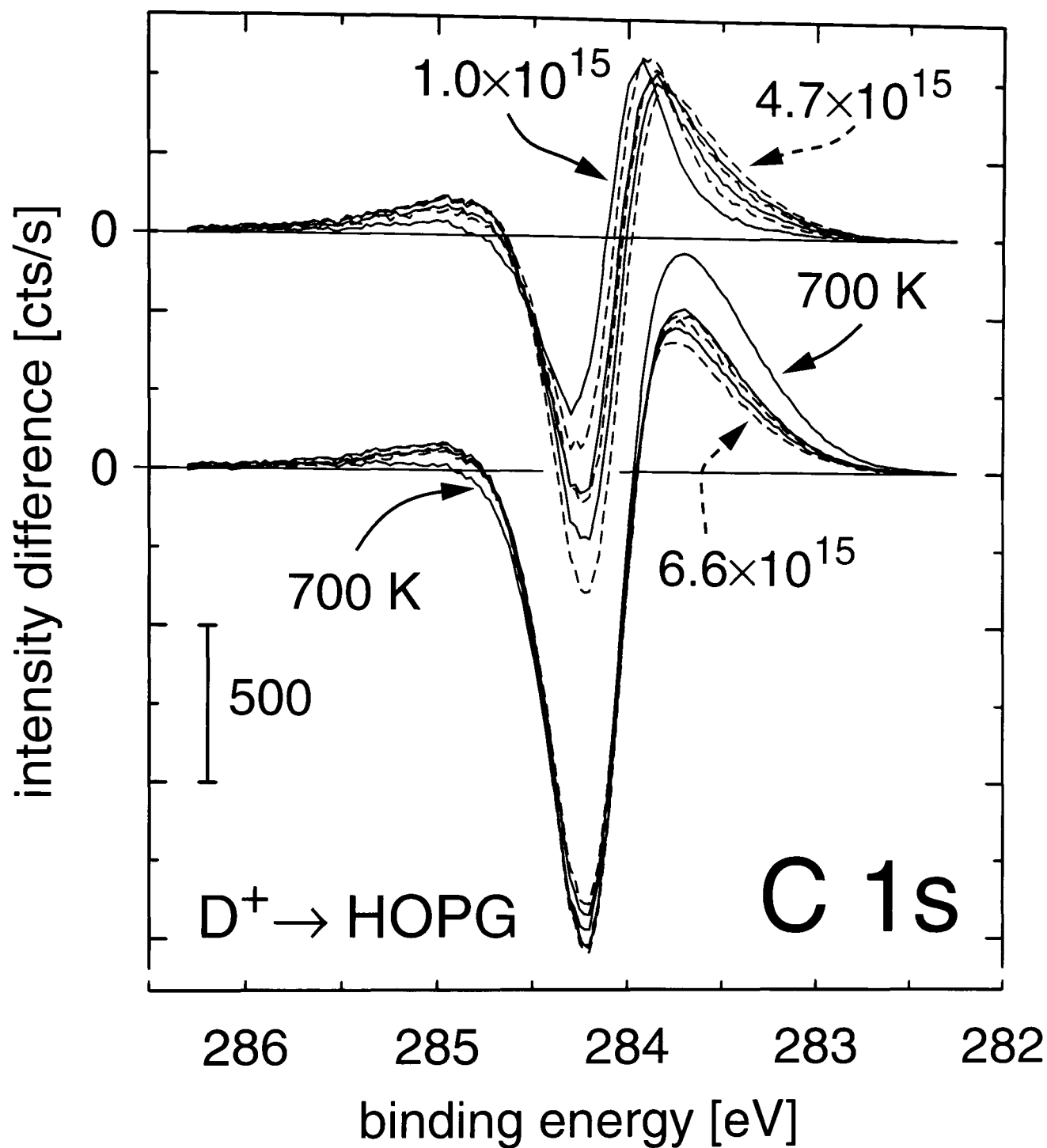
Figure 27: XPS difference spectra in the C 1s region of HOPG bombarded with 1 keV D^+ ions.

The consecutive fluence steps are separated into two groups. Successive spectra are marked with solid and broken lines, respectively. Some fluences are indicated, the

intermediate fluences correspond to the values of the data points in Figure 30. The final spectrum is measured after annealing at 700 K for 30 minutes.

The difference spectra immediately indicate intensity variations during the treatment cycles at three distinct binding energies. The intensity changes (height at maximum/minimum in Figure 27) of the three peaks in the difference spectra are plotted with increasing deuterium fluence in Figure 28(a). The greatest changes take place at a binding energy of 284.2 eV, which can be attributed to graphitic carbon. The position of this peak does not change throughout the whole treatment series. However, intensity in this position continuously decreases compared to the clean HOPG. After the final 700 K heating, a slight increase in intensity at this position is again observed.

The peak at the higher binding energy of 284.9 eV is very weak. However, its position is also stable. Intensity at this binding energy increases during the first implantation steps up to a fluence of approximately 7×10^{15} cm^{-2}. At higher fluences, first a small decrease is noticed and the intensity then remains constant up to the final implantation step. After heating at 700 K, the intensity around 284.9 eV almost drops back to the level at the clean HOPG surface.

The third peak component appears at 283.9 eV and shifts during the implantation to 283.7 eV. This component appears immediately after the first ion implantation step and maintains the initial maximum intensity throughout the subsequent ion treatments. It is only after the 700 K heating that the intensity of this component increases again and reaches a new maximum, while remaining constant at 283.7 eV binding energy.
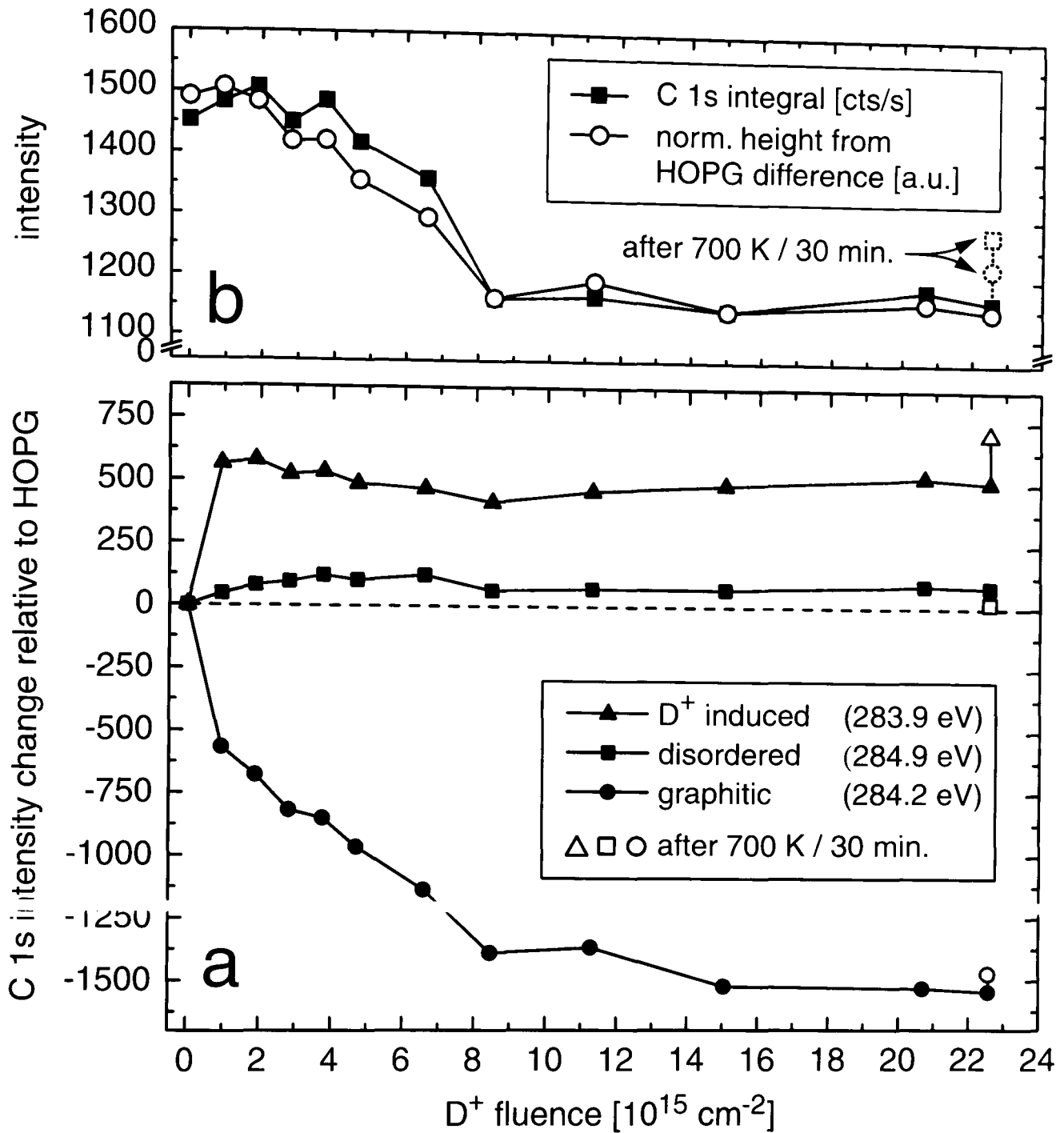
Figure 28: Chemical composition of highly oriented pyrolytic graphite during deuterium bombardment. Panel (a) shows the intensity changes of the three peaks identified in Figure 27. Positive values indicate an increase in intensity compared to HOPG at the respective binding energy, negative values a decrease. Panel (b) compares the total C 1s intensity from the raw spectra (after subtraction of a Shirley background) with the sum of the heights from panel (a) at each fluence. The scaling of the height curve is chosen to allow comparison with the intensity curve. Values after 700 K heating are indicated in the plots.

This method of spectrum evaluation by differences is justified by the overall development of the sum of the three difference peaks. In Figure 28(b) the sum of the three peaks is plotted together with the total C 1s peak integral from the XPS spectra (after Shirley background subtraction) to allow a comparison. For comparison, the sum is normalised to the amplitude of the C 1s curve. Both lines show the same overall behaviour.

After a small initial intensity increase during the start of ion bombardment, the curves decrease until a fluence of approximately 8×10^{15} cm^{-2} is reached. At higher fluences, no further changes are observed. The intensity increase seen for the C 1s peak after sample heating to 700 K is also reproduced by the sum of the difference peaks.

The variations in the difference spectra of the HOPG bombarded with deuterium are compared to the difference spectra of HOPG bombarded with argon.

Figure 29 shows an analogous experiment to Figure 27 for 1 keV Ar$^+$ up to a fluence of 8.5×10^{15} cm^{-2} and final annealing to 970 K for 60 min. As in the difference spectra from the D$^+$ experiment, three peaks are observed. However, the peak positions after Ar$^+$ bombardment do not shift with fluence. The peak around 285 eV appears under Ar$^+$ bombardment and develops with fluence. The dashed line corresponds to 8.5×10^{14} cm^{-2}, the subsequent implantation steps (fluences between 2.1×10^{15} cm^{-2} and 8.5×10^{15} cm^{-2}) already show saturation at this binding energy. After annealing to 970 K this peak almost completely vanishes again, as in the deuterium case.

The gradual changes with fluence are also visible in the intensity at 284.2 eV. At this position, however, no influence of the annealing step is recognised. The peak around 283.7 eV exhibits the most pronounced alteration after annealing. While Ar⁻ bombardment creates this peak already after the first fluence step and subsequent implantation cycles do not modify it, annealing strongly increases the intensity at this binding energy. The peak position, however, remains unaffected.

This confirms that the peak shift due to deuterium ion bombardment originates from chemical interactions between the projectile deuterium ions and the carbon sample. No such chemical interactions are possible with noble gas ions.
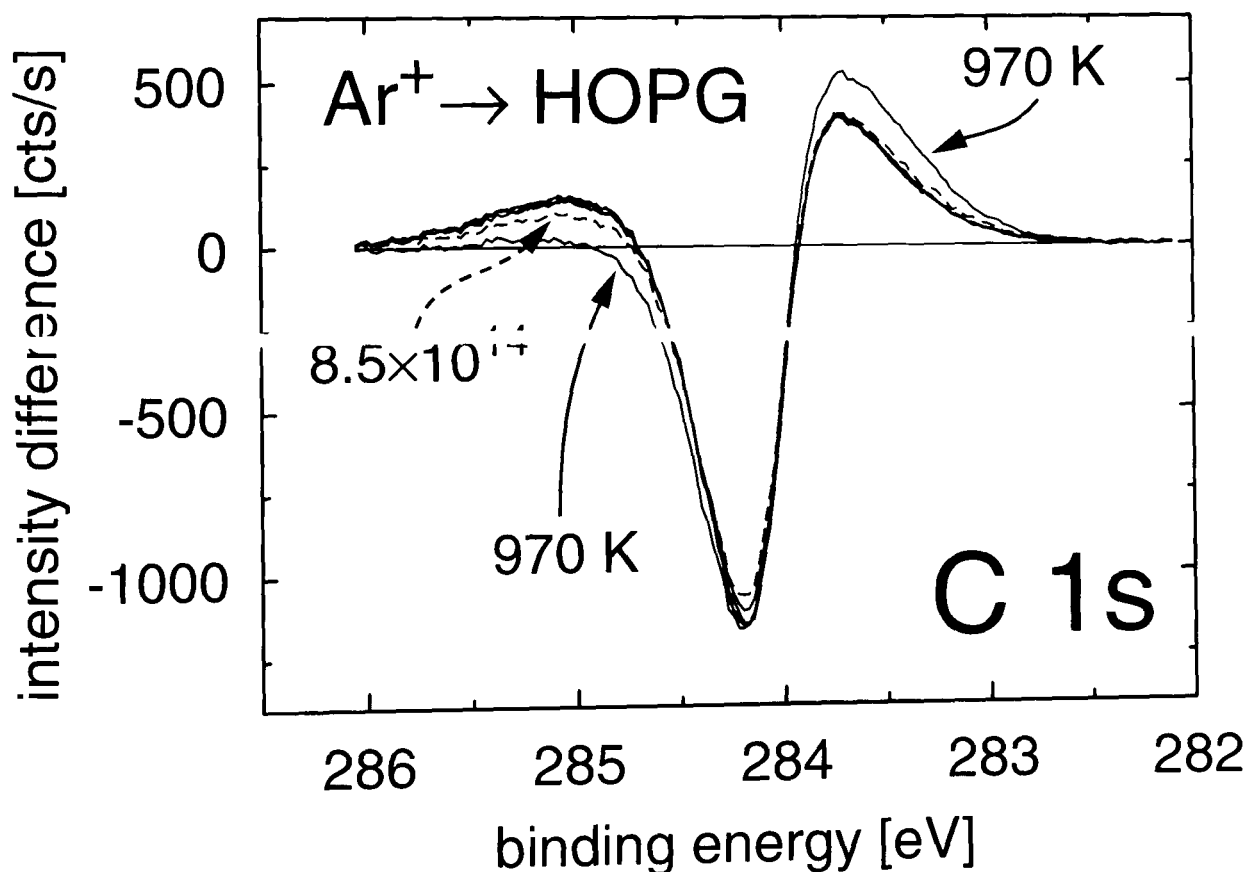
Figure 29: XPS difference spectra in the C 1s region of HOPG bombarded with 1 keV Ar⁺. Sample treatments are indicated. The overlapping spectra correspond to fluences from 2.1 to 8.5×10^{15} cm⁻².

6.2 Carbon films on titanium

A 2.9 nm carbon film on titanium was bombarded with 4 keV D^+ ions up to a fluence of 1.4×10^{17} cm^{-2}. The carbon layer thickness was determined from the XPS signal through the model for electron attenuation lengths in solids by A. Jablonski *et al.* [Jab02] as described in chapter 2.2.2.

The XPS information depth therefore is larger than the carbon layer thickness. Figure 30 shows the C 1s range after the indicated fluences. The spectrum without ion bombardment shows a broad peak compared to HOPG located at 284.6 eV, originating from graphitic carbon. A second peak at 281.8 eV originates from titanium carbide (TiC), formed at the interface between deposited carbon and titanium metal. Intensity between these peaks around 282.6 eV can be attributed to titanium subcarbides.

Aalready after a fluence of 3.9×10^{15} cm^{-2}, the graphitic peak shifts by 0.11 eV to lower binding energies and reaches a fixed position at 1.2×10^{16} cm^{-2} after a total shift of 0.22 eV. At the same time, no shift is observed in the position of the TiC signal. The total intensity of the C 1s signal decreases. The peak corresponding to elementary, graphitic carbon vanishes after a D^+ fluence of 5.5×10^{16} cm^{-2}, up to where the TiC signal continually increases. Within the fluence range applied here, no complete erosion of formed TiC is observed. Compared to the spectra of the bombarded HOPG samples, no increased intensity around 285.2 eV due to ion-beam-induced effects is visible.
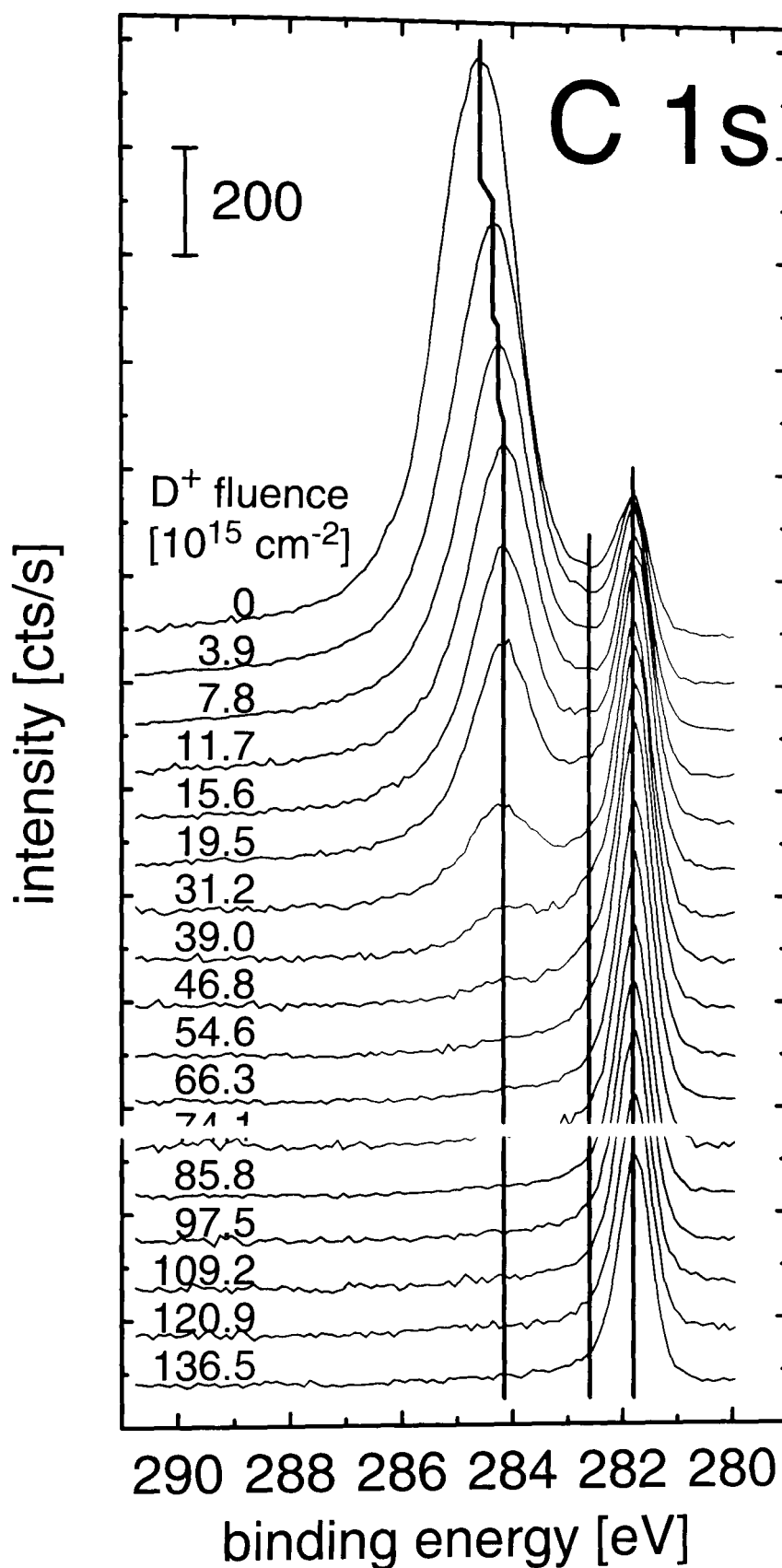
Figure 30: XPS spectra in the C 1s region of a 2.9 nm carbon film on titanium before and after D^+ ion bombardment at 4 keV. The curves are labelled with the applied D^+ fluences. The vertical lines indicate binding energies of graphitic carbon (284.2 eV), titanium subcarbides (282.6 eV), and TiC (281.8 eV), respectively.

These observed changes in the C 1s signals are more clearly visible in the difference spectra (plotted in Figure 31). Shown is the difference of the unirradiated spectrum from the spectra observed after fluences of 3.9×10^{15} to 4.7×10^{16} cm^{-2}. Compared to HOPG in Figure 27 and Figure 29 where a peak in the differences around 285 eV is observed, here only an intensity decrease is visible. No additional intensity is produced by the D$^+$ ion beam. In contrast to Ar$^+$ bombardment experiments of carbon films on Ti where the disordered graphitic carbon (peak at 285.2 eV), produced during the carbon vapour deposition, is eroded during the first ion implantation steps, no peak is formed at this binding energy under D$^+$ bombardment.
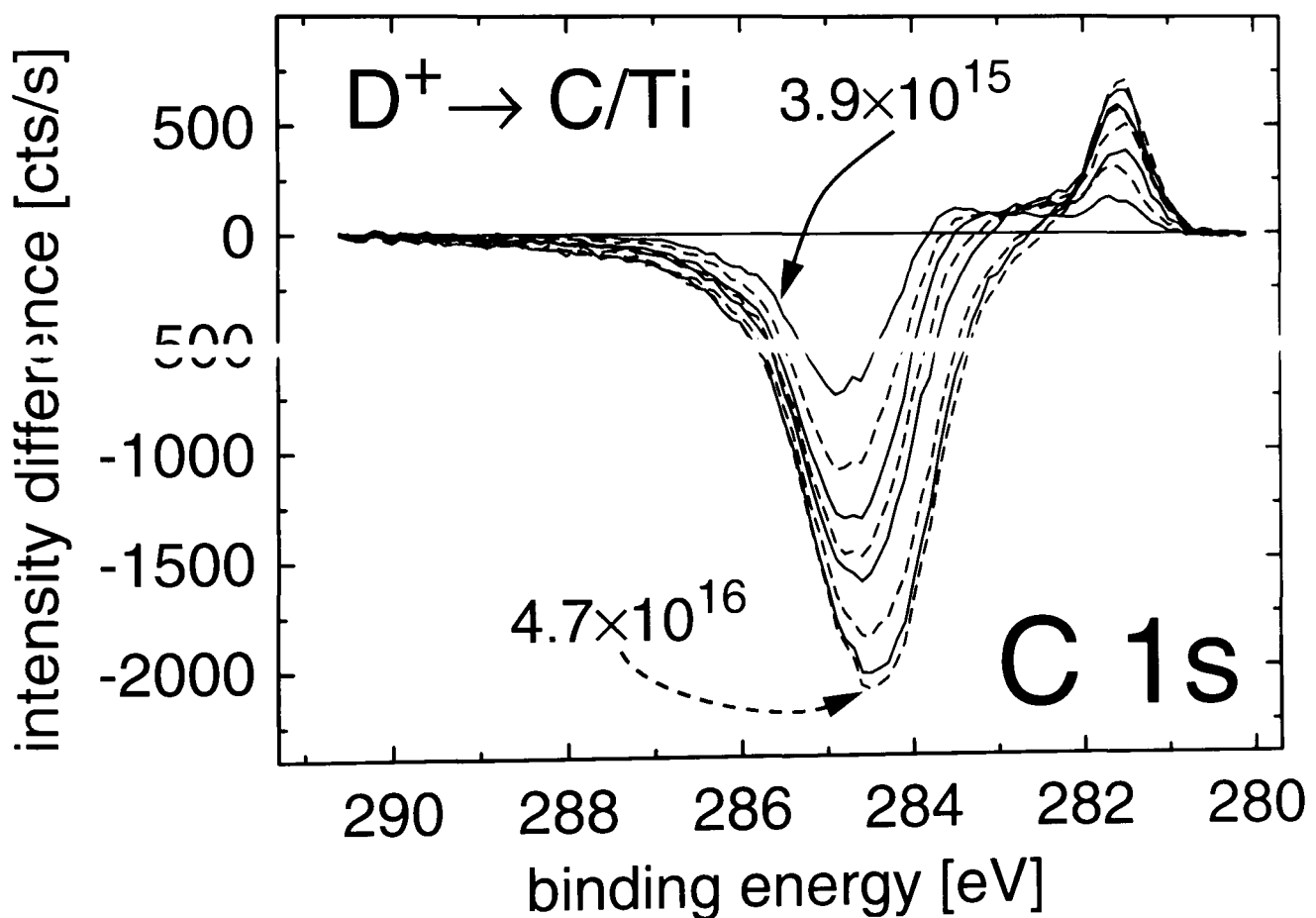
Figure 31: XPS difference spectra after D$^+$ implantation in 2.9 nm carbon on Ti, in the fluence range between 3.9×10^{15} and 4.7×10^{16} cm^{-2} (difference spectra at higher fluences in Figure 30 are omitted for clarity, since they exhibit only minor further changes).

Consecutive spectra are marked with solid and broken lines, respectively. The intermediate fluence values are labelled in Figure 30.

The peak around 283.8 eV, well developed in the HOPG experiments, is also identified on the carbon film. However, the maximum is only distinct at a fluence of 3.9×10^{15} cm^{-2}; it vanishes at higher ion fluences. The 281.8 eV peak originating from carbon in a TiC environment is clearly observed and remains fixed in its binding energy position for all fluences. The carbide intensity continues to increase with fluence, while the total carbon intensity decreases. Intensity pointing to the existence of titanium subcarbides (around 282.6 eV) is visible at the initial stages of D^+ bombardment. Beyond fluences of 1.6×10^{16} cm^{-2} the subcarbides are hardly discernible in the difference spectra. However, in the raw spectra (Figure 30) there is still some intensity around this binding energy. The existence of subcarbides cannot therefore be excluded.

XPS analysis yields no direct information about photoelectrons from hydrogen isotopes. However, comparison of deuterium ion bombardment with noble gas (argon) bombardment shows slight shifts in binding energies of the bombarded material. These shifts thus indicate chemical interactions between the hydrogen isotopes and the sample.

During deuterium and argon ion bombardment of HOPG a shift in binding energy and a broadening of the C 1s peak are observed. The shift of the C 1s peak to lower binding energy for both ion species is caused by a decrease in intensity at the graphitic carbon position (284.2 eV) and an increase of intensity at lower binding energy. The difference spectra reveal a peak 0.35–0.53 eV below the graphitic signal. In contrast to the existing

literature the difference spectra allow to distinguish components in the C 1s signal rather than to characterise spectral changes through mere peak shifts.

Compared to results from previous work it is possible to attribute the main peak and the high binding energy signal to graphitic carbon and carbon in a disordered graphitic environment [Lut01a]. The fact that the high binding energy component (285.2 eV) also disappears in the HOPG experiments under annealing confirms the assignment to a disordered graphite state. The new peak at lower binding energy is assigned to states induced by the ion beams. A shift to lower binding energy has previously been observed in the literature [Ash86, Ugo92] without separating components in the C 1s signal. In these measurements no shift towards higher binding energies after extended ion implantation is observed. On the contrary, after annealing of the implanted samples the C 1s signal shifts even further to lower binding energy.

The intensity decrease in the C 1s signal during ion implantation into HOPG is explained by the dilution of the carbon in the XPS information depth by hydrogen or argon. In contrast to what has been reported in the literature [Ash86, Ugo92, Fin01] no peak shift to higher binding energies at prolonged D^+ implantation is observed; this shift had been attributed to the formation of C–H bonds [Ugo92, Fin01]. Binding energies above 285.0 eV could also be attributed to sp^3-hybridised carbon [Fin01] which, however, is unlikely to be produced within a collision cascade at low fluences. Not compatible with the argument of C–H bond formation for a signal at any new binding energy is the fact that all binding energy shifts and intensity contributions observed here appear under both D^+ and inert Ar^+ bombardment. The binding energy values for sp and

sp^2 carbon from M. Portail *et al.* [Por00] indicate an interpretation of the shift to lower binding energies by C–H bond formation of unsaturated hydrocarbons. High Resolution Electron Energy Loss Spectroscopy (HREELS) measurements also confirm the formation of sp^2 and sp^3 carbon [Por00]. However, the identical observations for Ar implantation rule out this interpretation at least as far as being the only explanation. Similar shifts were also observed under He$^+$ implantation by K. Ashida *et al.* [Ash84]. The C 1s intensity below 284.0 eV can therefore be attributed to defects in the graphite lattice, produced by the collision cascades, and is therefore different from the disordered graphitic carbon with a binding energy of 285.2 eV. The reason for the smaller changes at below 284 eV in the case of the carbon film compared to the HOPG is the lower degree of structural order in the film. The film C 1s peak is initially already much wider than from HOPG and changes due to the ion-beam-induced effects are harder to detect.

The C 1s spectra and also the respective difference spectra of the carbon film on titanium do not allow a similar distinction between the elementary carbon binding states as in the case of HOPG. Initially, the disordered graphite phase has a high weight within the whole peak. The D$^+$ bombardment leads to an erosion, preferentially of the disordered graphite, and finally also of the graphitic carbon. The preferential erosion of the disordered phase is concluded from the decrease of the full-width at half-maximum (FWHM) of the high binding-energy-peak (1.63 eV initially and 1.04 eV after the implantation of 3.9×10^{16} cm^{-2}), the total shift of the peak to lower binding energies, as well as from the asymmetric development of the peak in the difference spectrum.

As in the HOPG experiments, the D^+ bombardment leads to the formation of a small amount of radiation-induced defects, indicated by the small peak around 283.6 eV in the difference spectra. In contrast to the HOPG samples, these defects in the film are only visible initially and are obscured by the decrease of the subcarbide phases during D^+ implantation. Carbon bound directly to titanium in TiC is initially present at the interface between the carbon layer and the substrate [Lin01]. It becomes more accessible to XPS with progressing layer erosion and even increases by ion-beam mixing. Ion-beam-induced carbide formation was already observed for noble gas ions [Lut01b]. After a maximum of the TiC signal (at 281.8 eV) at 5.5×10^{16} cm^{-2} this intensity decreases because of TiC erosion.
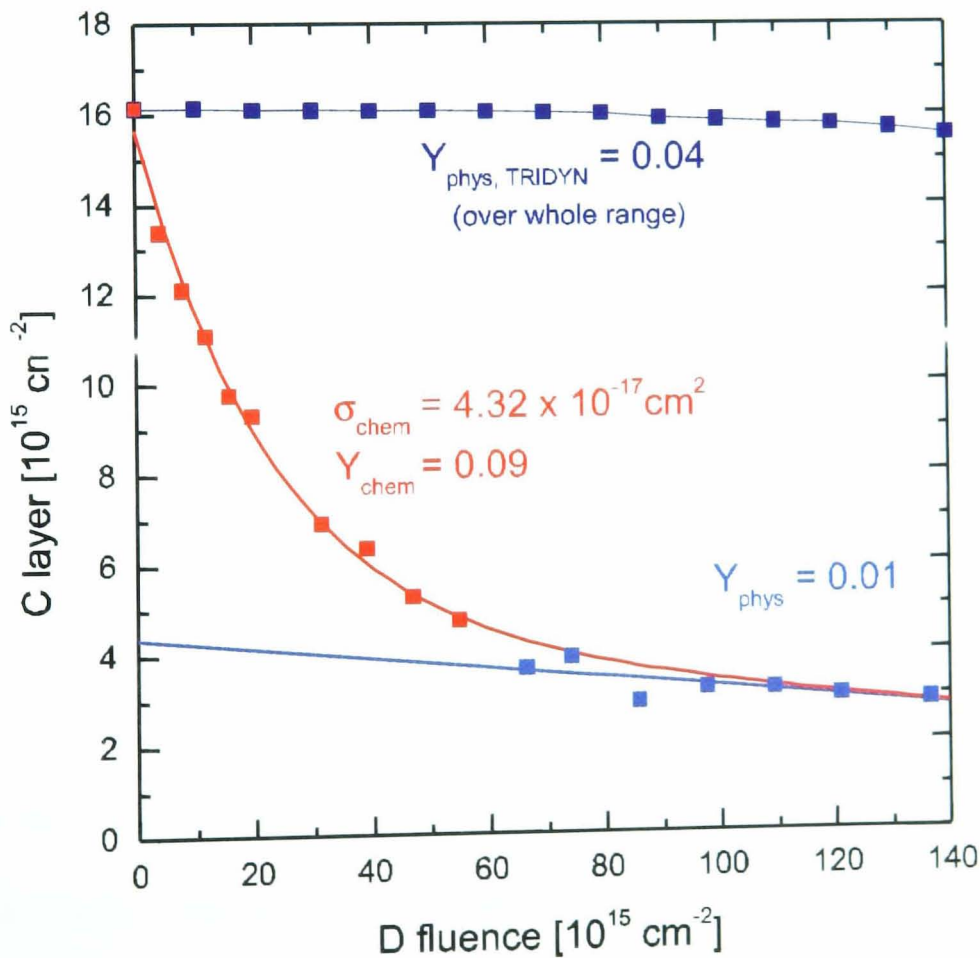
Figure 32: The erosion of a carbon surface layer on titanium is deduced from the XPS spectra which are displayed in Figure 30.

The total C 1s intensity decreases exponentially up to a deuterium fluence of

8×10^{16} cm^{-2}. At higher fluences, the intensity decrease follows a linear shape. The

threshold between the two parts is accompanied by the complete disappearance of all

carbon intensity other than from TiC (peak at 281.8 eV). The different slopes suggest

different erosion mechanisms. Below the threshold, elementary carbon is eroded

chemically by deuterium ions. The exponential shape is caused by an erosion

mechanism which involves the entire carbon layer, similar to the ion-induced desorption

of an adsorbed monolayer which was described by E. Taglauer *et al.* [Tag80]. This

model describes erosion of atomic monolayers through ion bombardment. The projectile

ions interact with the atoms in the entire surface layers, which thus do not provide

sufficient atoms for linear erosion yields and hence erosion follows an exponential

pattern. Applying this model to the deuterium ion bombardment of carbon layers on

titanium shows that the erosion mechanism of the carbon layer is governed by an

interaction between the implanted deuterium ion and the entire carbon surface layer.

This is plausible since the implantation range of 4 keV D$^+$ in C on Ti extends to more

than 100 nm, as calculated by TRIDYN. Therefore, the whole carbon layer of 2.9 nm is

irradiated and chemical erosion takes place simultaneously throughout the entire layer.

From the exponential curve (Figure 32), a reaction cross-section for carbon by D$^+$ of

$\sigma = 4.32 \times 10^{-17}$ cm^2 is calculated. Above the threshold fluence, an erosion yield of

Y=0.01 results from a linear fit to the data. The erosion yield Y is defined as the ratio of

the number of eroded atoms to the number of projectile ions. This number is in the range

of the physical sputtering yield: TRIDYN simulations using the code of W. Eckstein

[Eck93] were performed to simulate the kinematic erosion of this. For 4 keV D⁻ ion bombardment of graphite a yield of 0.04 was obtained.

Taking into account that TiC has a 1:1 stoichiometry, the result of this work agrees well with this TRIDYN calculation.

6.3 Deuterium bombardment of beryllium

The bombardment with deuterium of clean, metallic beryllium, and clean beryllium with carbon surface layers was investigated to determine the retention of deuterium in these samples, the erosion of surface layers, and the chemical states of the surface layers.

The deuterium retention was measured with the ^{3}He(D,^{4}He)p nuclear reaction, the carbon surface layer thickness was quantified through Rutherford backscattering spectrometry, and the chemical state of the carbon surface layer was determined through X-ray photoelectron spectroscopy.

Section 6.3.1 contains the results of deuterium retention in clean beryllium, section 6.3.2 contains the results of deuterium retention in beryllium with carbon surface layers and beryllium carbide surface layers and section 6.3.3 presents the formation of beryllium carbide through deuterium ion bombardment of elementary carbon layers on beryllium.

The effect of carbon-containing surface layers on the retention of deuterium in clean beryllium substrate, was looked at through consecutive series of implantations and

quantitative (RBS/NRA) measurements which were carried out on cleaned beryllium, elementary carbon layers as well as beryllium carbide (Be_2C) surface layers on cleaned beryllium substrates.

The process of erosion of beryllium carbide was detached from the formation of beryllium carbide by creating beryllium carbide through annealing before deuterium implantation. Annealing at 700 K was sufficient for the formation of beryllium carbide without substantial quantitative loss of carbon from the surface of the sample.

To understand the effects of the formation of beryllium carbide through deuterium ion bombardment and the chemical implications of implanted and retained deuterium, it is necessary to create conditions in which these two effects can be observed independently.

This was achieved by annealing samples of beryllium with elementary carbon surface layers at 700 K. The carbon surface layer was thus transformed into beryllium carbide (Be_2C) before deuterium implantation. As a result, no further chemical interactions between the beryllium and carbon in the form of beryllium carbide formation are possible. Comparison of the scenarios of elementary and carbidic carbon surface layers thus allows the identification of the effects of carbide formation and deuterium retention.

To identify and separate the effects of carbide formation from the erosion of carbon, a series of implantations was carried out on a prepared beryllium carbide surface layer on beryllium substrate.

The carbide layer was created by carbon vapour deposition on cleaned beryllium and subsequent annealing of the system at 700 K. This heating step was sufficient for the formation of beryllium carbide without quantitative loss of carbon from the surface layer on the sample.

6.3.1 Deuterium retention in clean, metallic beryllium

To study the retention of deuterium in beryllium, a cleaned beryllium crystal was bombarded with deuterium. Before implantation, an XPS spectrum indicates clean elementary beryllium with less than 0.5 monolayers oxygen and less than 0.1 monolayers carbon (see Figure 22).
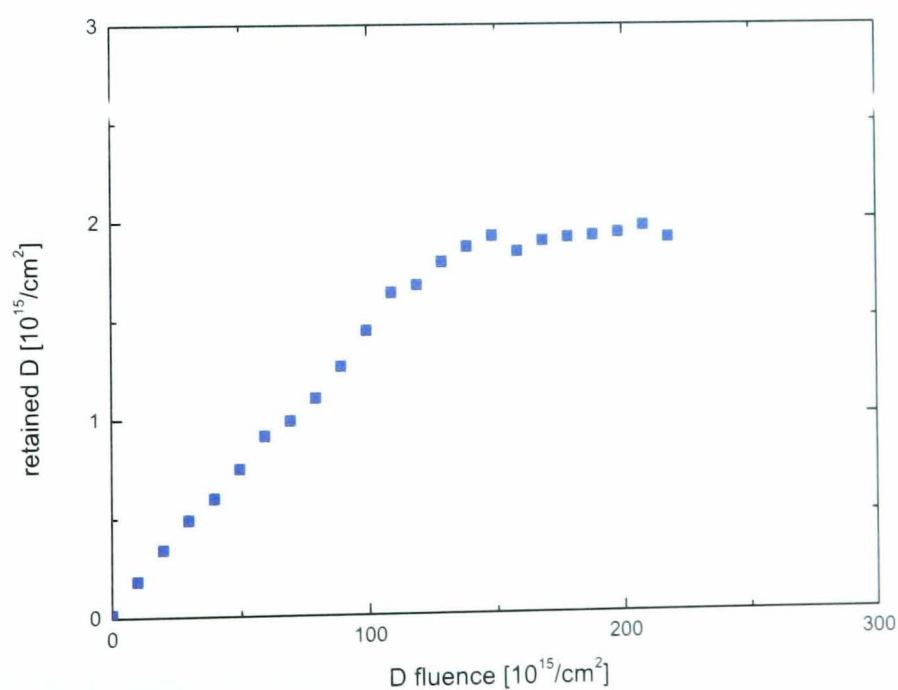
Figure 33: Retained deuterium in clean beryllium after 1 keV deuterium ion implantation.

After an initial linear increase in the retention of deuterium with a retention rate of 2% up to an implanted fluence of 1.5×10^{17} cm^{-2}, saturation in the retained deuterium is achieved after an implanted fluence of 2.5×10^{17} cm^{-2}. The saturated retained quantity of deuterium is determined at 2×10^{15} D per cm^2. This level of saturation is maintained after further deuterium implantation. (Figure 33)

Previously reported saturation levels of hydrogen isotopes in elementary beryllium indicate an impurity surface layer. Operation in vacuum conditions of 10^{-6} Pa to 10^{-7} Pa invariably leads to an impurity surface layer, consisting mainly of atmospheric oxygen [And99]. These values will therefore reflect the conditions in a fusion reactor. However, they differ from hydrogen isotope retention in clean, metallic beryllium samples, which were studied here.

The retained neon from the sputtering cycles amounted to less than 5×10^{15} cm^{-2} (Figure 22). As a noble gas, the neon does not represent an impurity for chemical reactions between the available species of beryllium, carbon, and deuterium.

For the cleaning of the beryllium substrate, neon was chosen because its boiling temperature of 27.07 K ensured that no sublimation would occur on the liquid nitrogen cold trap at 77.36 K. Alternatively, the choice of argon (boiling temperature: 83.8 K) would have resulted in sublimation on the cold trap while the sputtering yield of the main impurities oxygen and carbon through helium ion bombardment would require significantly longer sputtering periods.

The effect of surface impurity layers on the hydrogen isotope retention in beryllium is shown in Figure 34. The first six implantations of a clean beryllium sample were performed in one day. The following implantations were continued on the following day. In the interruption of 15 hours, a thin beryllium oxide surface layer was formed and a change in the deuterium retention is observed. After a deuterium fluence of $75 \times 10^{15} \, cm^{-2}$ the trend of the previous day is resumed, as indicated by the dashed line to guide the eye.

As a result, all following implantations which are presented here were carried out uninterruptedly in one day to ensure that the effects of oxygen impurities were minimised.
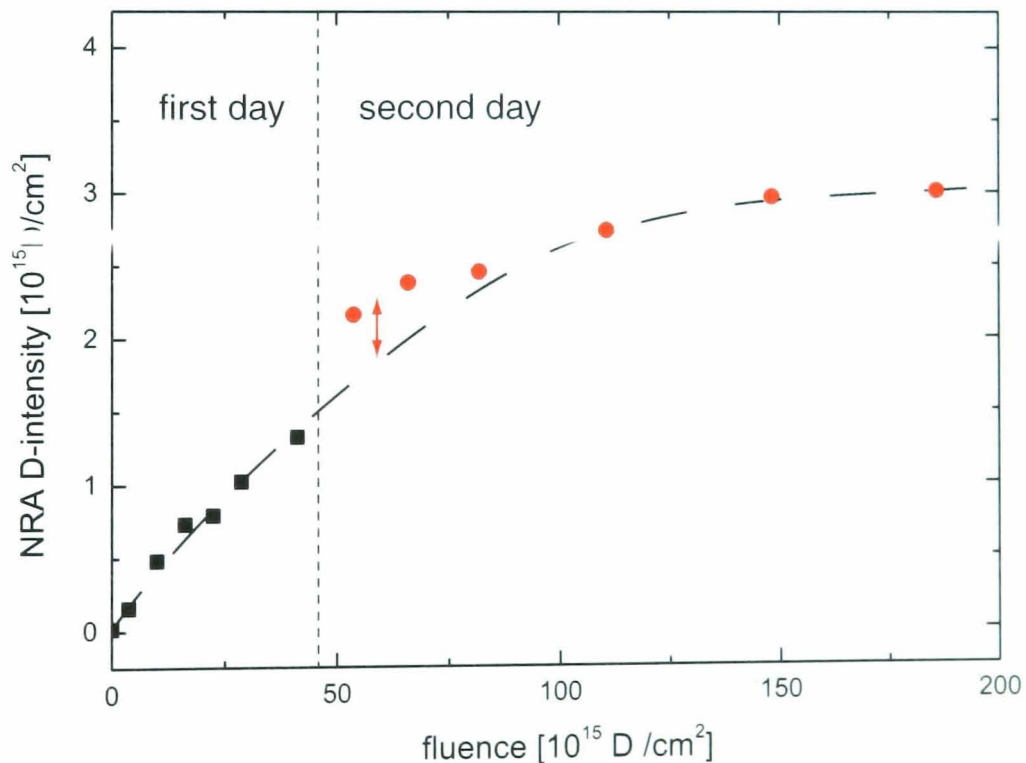
Figure 34: Retention of deuterium in cleaned beryllium and effect of beryllium oxide surface impurity layer after 15 hours (dashed line) in ultra high vacuum (below 3×10^{-9} Pa).

6.3.2 Deuterium retention in beryllium with carbon and beryllium carbide surface layers

To study the retention of deuterium in beryllium with carbon surface layers, systems of elementary carbon surface layers and systems of beryllium carbide (Be$_2$C) surface layers were bombarded with deuterium ions. The combination of projectile energy (1.0 keV deuterium) and surface layer thickness (2-8 nm) was chosen such that the implanted deuterium came to rest in the beryllium substrate; the mean range of implanted deuterium ions into beryllium at 1 keV is greater than 26 nm.

To be able to separate the processes of carbide formation as well as its effects on the deuterium retention in beryllium, implantations were also investigated on prepared carbide layer systems on beryllium.

The discrepancy in the retention of deuterium in beryllium between the results presented here and earlier observations [Cau97] must be attributed to surface conditions of the samples.

Surface layers of oxygen or carbon affect the retention of deuterium. The surface impurities provide new binding states for the deuterium which act as barriers to the desorption of the implanted deuterium.
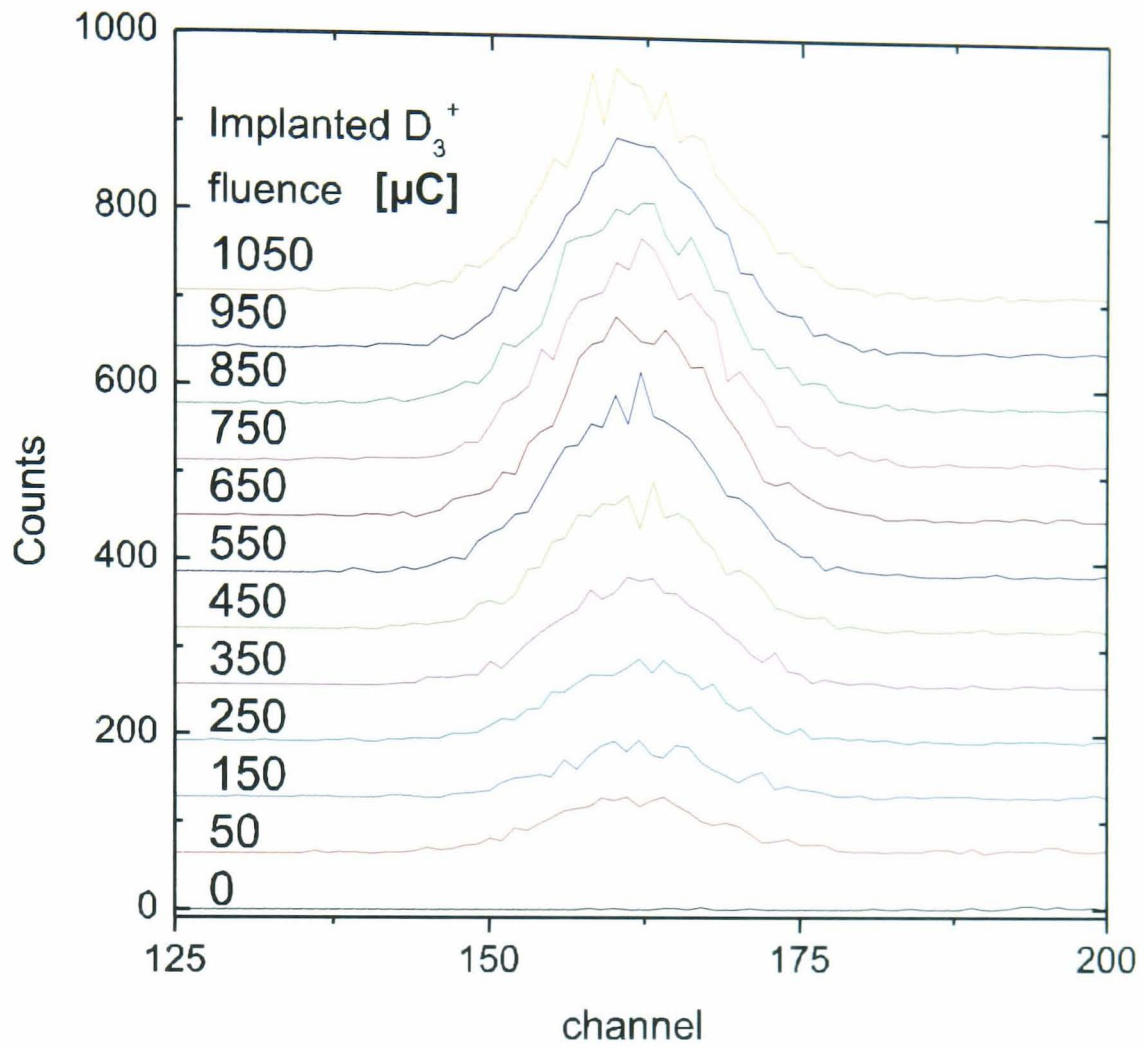
Figure 35: The retention of deuterium in beryllium with elementary carbon surface layer is observed and quantified using the nuclear reaction $D(^3He,p)^4He$.
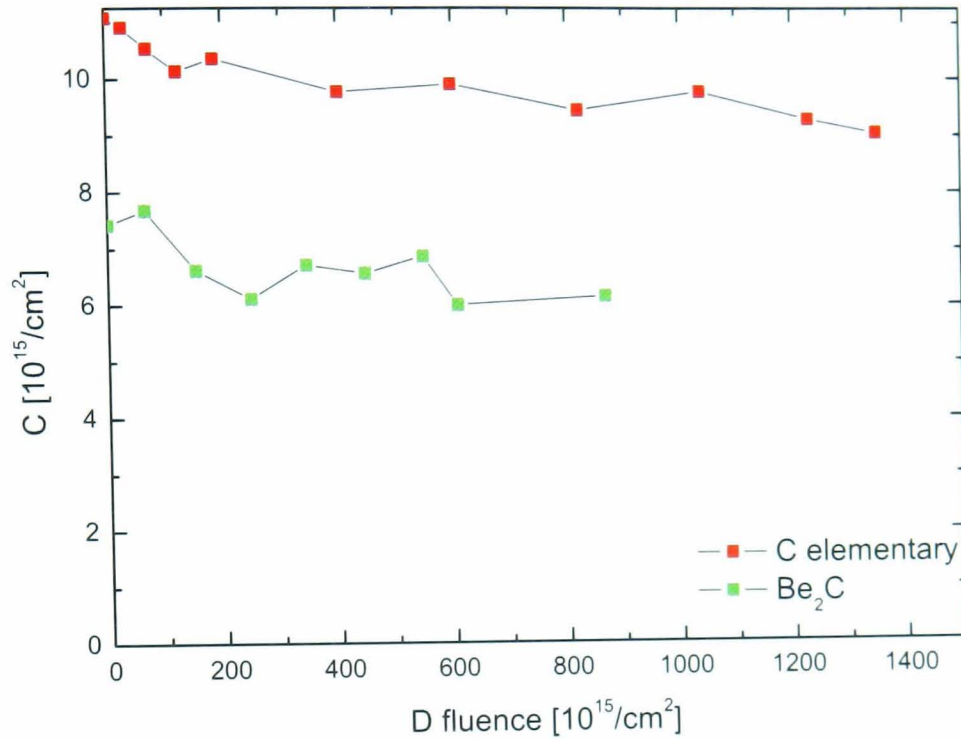
Figure 36: Quantitative erosion of elementary carbon surface layers and carbon in beryllium carbide due to deuterium ion bombardment.

The erosion of elementary and carbidic carbon surface layers through deuterium ion bombardment at 1.0 keV is shown in Figure 36. The erosion rates show no significant deviation which is caused by the absence of elementary carbon.
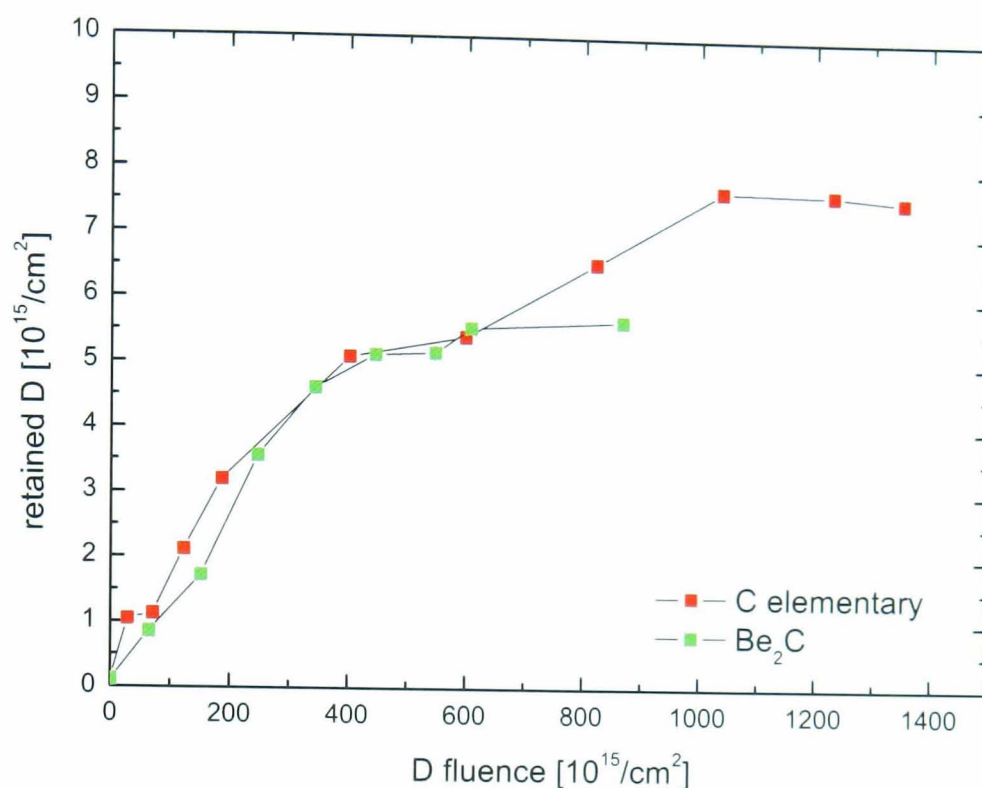
Figure 37: Retained deuterium in carbon-beryllium systems after 1 keV deuterium ion bombardment.

NRA spectra of the retained deuterium in carbon layers on beryllium is shown in Figure 35. The retention of implanted deuterium in beryllium with carbon surface layers is plotted in Figure 37. Initially, the retention of deuterium is independent of the chemical state of the carbon surface layers. Saturation of deuterium is reached above a fluence of $10^{18}/cm^2$.

The chemical state of the carbon surface layers does not have a significant quantitative effect on the retention of deuterium in beryllium. However, the retention in beryllium with surface layers is significantly greater than in clean, elementary beryllium.

After an initial linear retention of deuterium with increasing implanted fluence at a retention rate of 0.003, retention saturated after a fluence of $1 \times 10^{18} / cm^2$ at a level of $7.6 \times 10^{15} / cm^2$.

6.3.3 Formation of beryllium carbide

To understand the chemical processes during the formation of beryllium carbide through deuterium ion bombardment a sequence of implantations and XPS scans of the beryllium (Be 1s) and carbon (C 1s) binding energy regions was performed. The beryllium carbide (Be_2C) formation through deuterium implantation is observed with XPS of the C 1s electron binding energy region. (Figure 38)

Before the first implantation, a survey spectrum covering the electron binding energy region up to 1200 eV shows an elementary carbon layer of 2.1 nm on the cleaned beryllium substrate.

The deuterium bombardment of carbon layers on beryllium not only leads to retention of the implanted deuterium ions:

The implanted deuterium ions also supply the energy which leads to the chemical formation of beryllium carbide (Be_2C).
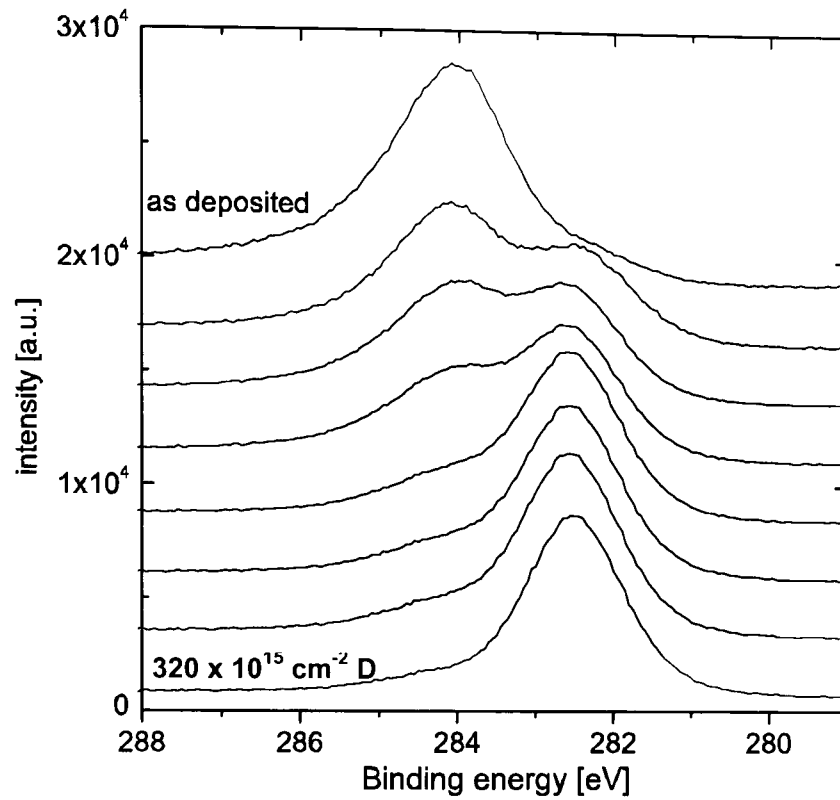
Figure 38: Beryllium carbide (Be_2C) formation through deuterium ion bombardment.

The series of XPS spectra of the binding energy region of carbon C 1s electrons (288 eV

to 280 eV) shows the formation of the beryllium carbide (Be_2C) phase.

This can be seen more clearly in Figure 39, where the contributions of the elementary

and carbidic carbon phases are shown.
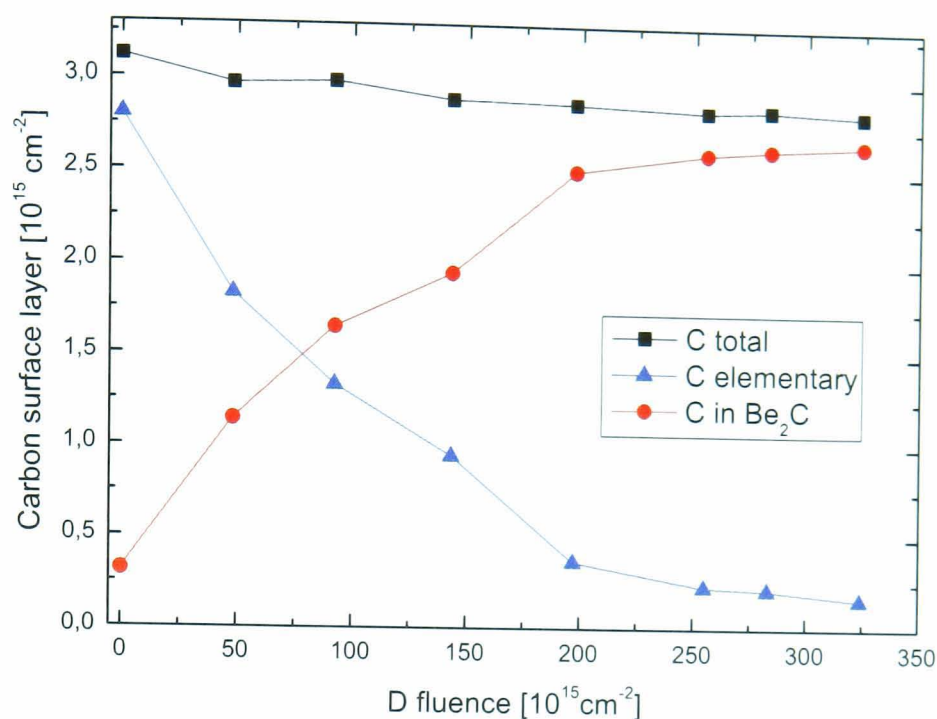
Figure 39: Chemical composition and erosion of carbon surface layer during 1 keV deuterium ion bombardment.

In a future fusion reactor, in which the surface of the plasma-facing components will invariably have experienced exposure to atmospheric conditions, particularly a beryllium tile will carry a surface impurity layer. The effect of this impurity greatly affects the hydrogen in the plasma. This unfavourable behaviour is particularly undesirable in operation modes with tritium-containing plasmas, because the increased retention of β^- emitting tritium in beryllium with impurity surface layers leads to further activation of components in the first-wall material.

6.4 Summary of results

The analysis of the effect of carbon surface layers on the retention of deuterium in metals was studied with a variety of techniques, to investigate the retention of implanted deuterium, the erosion of samples through ion bombardment, as well as the underlying chemical composition of mixed material surface layer systems.

All these effects can be observed and deduced from the collected data that is presented in chapter 6.

6.4.1 Erosion of carbon

The XPS spectra of pure carbon samples (HOPG) show a shift to lower binding energies of the C 1s photoelectrons with increasing deuterium ion fluence. This suggests that an interaction between the deuterium ions and the graphite produces slight changes in the chemical composition of the surface layer. The height of the peak is reduced with increasing ion fluences; however, at the same time the width increases such that the integral remains constant. This is because XPS can only probe the near-surface region of the carbon sample. For this reason it is impossible to measure the erosion of a bulk material.

These shifts were also observed in the XPS spectra of titanium with a carbon surface layer, suggesting that the same interaction takes place in this case. From the fact that the

height of the peak corresponding to graphite falls with increasing deuterium ion fluence, it can be deduced that the carbon layer is being eroded. However, this is not the only effect taking place; the growth of the peak at 284.2 eV, corresponding to titanium carbide TiC, indicates that some of the kinetic energy of the D ions is deposited and causes the formation of a TiC phase. This is discussed in more detail in section 6.4.3. The shrinking of the graphite peak at 288.2 eV cannot therefore be attributed to erosion alone.

Some observations can be made about the physical effects governing the erosion process of the surface layer. At low ion bombardment fluences there is an exponential decrease of the amount of carbon held in the surface layer, indicating a non-kinematic erosion process. Chemical interactions play a dominant role in this regime.

By contrast, at high fluences where the carbon in the surface layer has been fully converted into the TiC phase, the erosion process agrees well with the kinematic model, as simulated using TRIDYN.

Similar effects can be observed in the XPS spectra obtained for carbon-coated beryllium. Again, shrinking of the peak corresponding to graphite suggests erosion of the carbon layer. However, as in the case of a titanium substrate, this shrinkage is accompanied by the growth of a peak at 282.6 eV, indicating formation of a Be_2C phase (cf. section 6.4.3).

Comparison of the results obtained for beryllium with a pure carbon layer to results obtained for beryllium with a Be_2C layer show that carbon erodes at a similar rate for both types. This differs from the behaviour displayed by the titanium samples.

6.4.2 Deuterium retention in beryllium samples

The NRA spectra obtained for deuterium-bombarded samples of beryllium show a similar increase in retained deuterium with increasing ion fluences both for pure beryllium as well as for carbon-coated beryllium, as can be seen in Figure 40. This may be due to similar caption mechanisms for all types of beryllium samples.
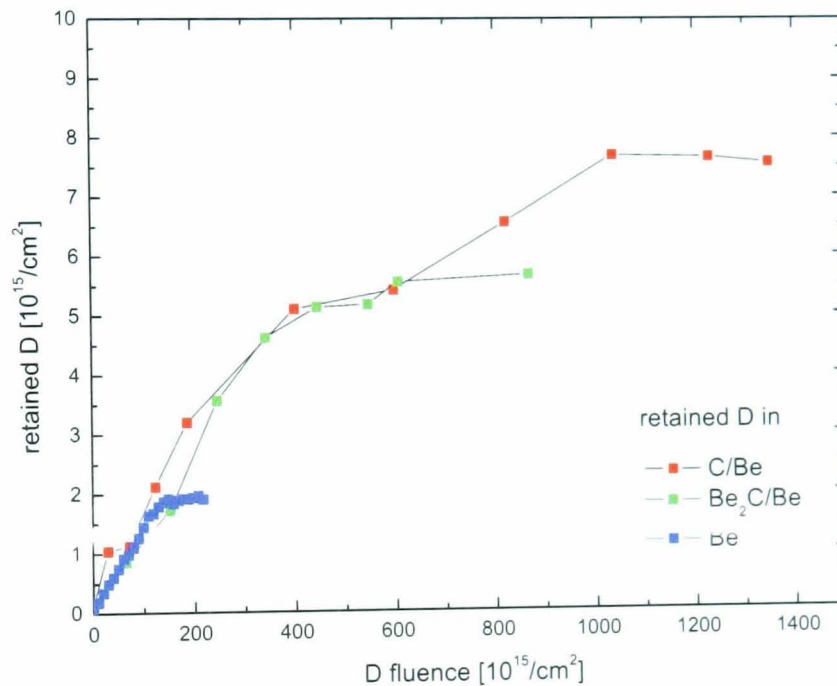
Figure 40: Retention of deuterium in clean beryllium and in beryllium with carbon surface layers. The effect of surface layers is an increased deuterium retention capacity.

The retention of deuterium in clean metallic beryllium saturated at a level of $2 \times 10^{15}/cm^2$. This is substantially lower than the saturation levels obtained for both mixed-material beryllium samples; $5.5 \times 10^{15}/cm^2$ for beryllium with an elementary carbon surface, and $7.6 \times 10^{15}/cm^2$ for a beryllium carbide surface layer.

Metallic beryllium that was left in a vacuum of 3×10^{-9} Pa for 15 hours showed a modified retention rate upon ion bombardment compared with the retention rate observed for clean beryllium, indicating the presence of accumulated impurities in the surface layer. At higher fluences, this difference disappeared. This can be explained by the erosion of the impurities through ion bombardment.

Previously reported values of saturation in deuterium retention are greater than the value observed here for clean metallic beryllium. However, measurements on which these values are based were conducted under vacuum conditions with pressures of the order of 10^{-8} Pa.

It may be assumed that this leads to a much higher density of impurities in the surface layer that was not fully removed by ion bombardment.

6.4.3 Changes in chemical composition

XPS spectra of argon implantation in highly-oriented pyrolytic graphite show no shifts in the positions of the peaks with increasing ion fluence. This is in contrast to what is observed in the spectra of deuterium ion bombardment, suggesting that a chemical interaction takes place between the hydrogen isotope ions and the carbon. As a noble gas, argon is not involved in a chemical reaction and cannot therefore lead to chemical shifts in the binding energy levels of C 1s electrons.

This effect of a modified carbon state is also observed in deuterium ion bombardment of carbon-coated titanium, where the peaks corresponding to carbon shift in a similar way.

In addition, a further peak grows with increasing deuterium fluence. This may be attributed to the growth of a TiC phase; the deuterium ions deposit some of their kinetic energy, thus creating carbides. A small intensity contribution at this position before ion implantation is due to the carbon-titanium interface, where TiC is present from the first. This peak does not shift in position with increasing ion fluence, implying that no changes are made to the chemical state.

Similar observations can be made from the spectra for deuterium ion bombardment of beryllium with a carbon layer: a shift in the position of the carbon peak indicates a chemical interaction between the carbon layer and the implanted hydrogen isotope. Moreover, as with titanium, the formation of beryllium carbide is indicated by the growth of a further peak.

7 Conclusions

The aim of this work was to investigate the effect of implanting hydrogen isotopes with energies in the keV range into materials, as applicable to plasma nuclear fusion devices. This involved the redesign and construction of an ultra-high vacuum device, Artoss. The modified apparatus has the facilities to clean, modify, and analyse samples with mixed material surface layers, and can achieve ultra-high vacuum conditions with base pressures of less than 3×10^{-9} Pa .

During the construction phase of Artoss, the effects of deuterium ion bombardment of carbon layers on titanium were studied using X-ray photoelectron spectroscopy on another ultra-high vacuum setup (XPS).

In measurements where samples consisting of carbon layers on a titanium or a beryllium substrate were bombarded with deuterium ions, it was observed that the carbon erodes at higher yields when it is present in its elementary state than when it is present in the form of a carbide. Moreover, it was found that different mechanisms govern the erosion process, depending on whether the carbon is elementary or carbidic. The erosion rate of carbon in titanium carbide is well accounted for in a kinematic collision model, as could be shown by comparing the data to a computer simulation. By contrast, elementary carbon erosion has further contributions from chemical interactions between the deuterium and the carbon atoms.

The saturation level of deuterium retention was found to be considerably affected by modifications in the surface of a material. Clean metallic beryllium saturated at a lower deuterium level than beryllium with a carbon or a beryllium carbide layer.

Additionally, it was noted that even under the achieved ultra-high vacuum conditions, the surface layer of pure beryllium accumulated impurities, mainly oxygen, from the residual gas over the course of 15 hours, which changed the material's reaction properties with hydrogen isotopes and allowed a higher retention rate. This implies that previous studies of beryllium bombarded with deuterium, which have been conducted under vacuum conditions with 10^{-7} Pa dealt with modified surface layers rather than pure beryllium.

Hydrogen isotope retention is ideally minimised in any first-wall material for a number of reasons. It disturbs the plasma; and as tritium is radioactive, retaining this isotope in the building blocks of a fusion device is not desirable.

Fusion in magnetically confined hydrogen isotope plasmas depends to a great extent on a low level of impurity ions in the plasma, as these either reduce the hydrogen isotope density through dilution (in the case of light isotopes), and lead to cooling of the plasma through radiation from the bound electrons in heavy, not fully ionised impurities. Therefore, its low atomic weight, coupled with the fact that beryllium is a highly reactive getter material that binds oxygen impurities from the residual gas in the chamber, make beryllium a very attractive plasma-facing material in fusion energy devices.

8 Bibliography

[And92]   R.A. Anderl, M.R. Hankins, G.R. Longhurst, R.J. Pawelko and R.G. Macaulay-Newcombe, *Journal of Nuclear Materials* **196-198** (1992) 986-991

[And99]   R.A. Anderl, R.A. Causey, J.W. Davis, R.P. Doerner, G. Federici, A.A. Haasz, G.R. Longhurst, W.R. Wampler and K.L. Wilson, *Journal of Nuclear Materials* **273** (1999), 1

[Ara89]   R. Aratari and W. Eckstein, *Nuclear Instruments and Methods in Physics Research B* **42** (1989) 11

[Ash84]   K. Ashida, K. Ichimura, M. Matsuyama and K. Watanabe, *Journal of Nuclear Materials* **128&129** (1984), 792

[Ash86]   K. Ashida, K. Kanamori, K. Ichimura, M. Matsuyama and K. Watanabe, *Journal of Nuclear Materials* **137** (1986), 288

[Ash97]   K. Ashida, K. Watanabe and T. Okabe, *Journal of Nuclear Materials* **241-243** (1997) 1060-1064

[Bie80]   J. Biersack and L. Haggmark, *Nuclear Instruments and Methods* **174** (1980) 602

[Bie84]   J. Biersack and W. Eckstein, *Applied Physics A*, **34** (1984) 73

[Bri83]   D. Briggs and M. Seah, *Practical Surface Analysis by Auger and X-Ray Photoelectron Spectroscopy*, John Wiley & Sons, Chichester, (1983)

[Bri85]   D. Briggs and M.P. Seah, *Practical Surface Analysis by Auger and X-ray Photoelectron Spectroscopy*. John Wiley and Sons, Chichester (1985)

[Cau90a]   R.A. Causey, W.L. Hsu, B.E. Mills, J. Ehrenberg and V. Philipps, *Journal of Nuclear Materials* **176&177** (1990) 654-660

[Cau90b]   R.A. Causey, W.L. Hsu, B.E. Mills, J. Ehrenberg and V. Philipps, *Journal of Nuclear Materials* **176&177** (1990) 661-665

[Cau97]   R.A. Causey, G.R. Longhurst, W. Harbin, *Journal of Nuclear Materials* **241-243**(1997) 1041-1047

[Cau02]   R.A. Causey, *Journal of Nuclear Materials*, **300** (2002) 91

[Con97]   R.W. Conn, R.P. Doerner and J. Won, *Fusion Engineering and Design* **37** (1997) 481

[Dah95]   D. Dahl, SIMION 3D V. 6.0, 43rd ASMS Conf. on Mass Spectrometry and Allied Topics, Atlanta (1995)

[Eck91]   W. Eckstein, Computer Simulation of Ion–Solid Interactions. *Springer Series in Materials Science* **vol. 10**, Springer, Berlin (1991)

[Eck93]   W. Eckstein, C. García-Rosales, J. Roth, W. Ottenberger. Max-Planck-Institut für Plasmaphysik, Garching, IPP-Report **9/82**, (1993)

[Fed01]   G. Federici, C.H. Skinner, J.N. Brooks, J.P. Coad, C. Grisolia, A.A. Haasz, A. Hassanein, V. Philipps, C.S. Pitcher, J. Roth, W.R. Wampler and D.C. Whyte, *Nuclear Fusion* **41** (2001), 1967

[Fin01]   A. Fink, W. Widdra, W. Wurth, C. Keller, M. Stichler, A. Achleitner, G. Comelli, S. Lizzit, A. Baraldi and D. Menzel, *Physical Review B* **64** (2001), 045308

[Fra89]   E. Franconi, M. Rubel and B. Emmoth, *Nuclear Fusion* **29** (1989) 787

[Gol99]   P. Goldstraß, W. Eckstein, and Ch. Linsmeier, *Journal of Nuclear Materials* **266-269** (1999) 581

[Gol00]   H.P. Goldstraß, Carbidbildung auf Beryllium. PhD thesis (2000) University of Bayreuth

[Gol01]   P. Goldstraß, and Ch. Linsmeier, *Journal of Nuclear Materials* **290-293** (2001) 71-75

[Gri95]   W.H. Gries, *Journal of Vacuum Science and Technology*. **A13,3** (1995) 1304

[Gri96]   W.H. Gries, *Surface and Interface Analysis*. **24** (1996) 38

[Hir97]   Y. Hirooka, *Fusion Engineering and Design* **37** (1997) 299

[ITER96]   ITER Project, Detailed Design Document, IdoMS# G 16 DDD 2 96-11-27

[Jab99]   A. Jablonski and C.J. Powell, *Journal of Electron Spectroscopy and Related Phenomena* **100** (1999) 137

[Jab02]   A. Jablonski and C.J. Powell, *Applied Surface Science* **90** (2002) 33

[Jan01]   G. Janeschitz, ITER JCT and HTs, *Journal of Nuclear Materials* **290-293**

(2001) 1

[Kri99]   K. Krieger, H. Maier and R. Neu, *Journal of Nuclear Materials* **266-269** (1999) 207

[Kri01]   K. Krieger, H. Maier, R. Neu, V. Rohde and A. Tabasso, *Fusion Engineering and Design,* **56-57** (2001) 189

[Les89]   B. Lesiak, A. Jablonski, Z. Prussak and P. Mrozek, *Surface Science.* **223** (1989) 213

[Lie87]   H. Liebl, J. Bohdansky, J. Roth, and V. Dose. *Review of Scientific Instruments* **58** (1987) 1830

[Lin61]   J. Lindhard und M. Scharff., *Physical Review.* **124** (1961) 128

[Lin01]   Ch. Linsmeier, J. Luthin and P. Goldstraß, *Journal of Nuclear Materials* **290–293** (2001), 25

[Lin03]   Ch. Linsmeier, J. Roth, K. Schmid, IAEA APID Series vol. 12 (2003)

[Lut00]   J. Luthin and Ch. Linsmeier, *Surface Science* **454–456** (2000). 78

[Lut01a]   J. Luthin and Ch. Linsmeier, *Physica Scripta T* **91** (2001), 134

[Lut01b]   J. Luthin, H. Plank, J. Roth and Ch. Linsmeier, *Nuclear Instruments and Methods B* **182** (2001), 218

[Lut01c]   Untersuchungen zur chemischen Wechselwirkung bei der Bildung von Kohlenstoff-Mischsystemen. PhD thesis (2003) University of Bayreuth

[Mar84]   C. Martin, E.T. Arakawa, T.A. Callcott and J.C. Ashley. *Journal of Electron Spectroscopy and Related Phenomena,* **35** (1984) 307

[May97]   M. Mayer, R. Behrisch, P. Andre and A.T. Peacock, *Journal of Nuclear Materials,* **241-243** (1997) 469

[May98]   M. Mayer, M. Balden and R. Behrisch, *Journal of Nuclear Materials.* **252** (1998) 55

[Mil97]   S. Miller, G. Berning, H. Plank and J. Roth, *Journal of Vacuum Science and Technology A* **15** (1997), 2029

[Moe84]   W. Möller and W. Eckstein, *Nuclear Instruments and Methods in Physics Research B* **2** (1984) 814

[Nau92]   D. Naujoks and R. Behrisch, Proceedings of the International Conference on Plasma Physics, Innsbruck, 16C part II (1992) 843

[Par00]   R. Parker, *Nuclear Fusion*, **473** (2000) 1

[Por00]   M. Portail, I. Forbeaux, N. Papapeorgiou, M. Carrère, D. Roy and J.-M. Layet, *Surface Science* **454–456** (2000), 384

[Rot80]   J. Roth and B.M.U. Scherzer, *Journal of Nuclear Materials* **93&94** (1980) 601

[Rot96]   J. Roth and C. García-Rosales, *Nuclear Fusion*, 36, **12** (1996) 1647

[Rot97]   J. Roth, W.R. Wampler, W. Jacob, *Journal of Nuclear Materials* **250** (1997) 23

[Sea79]   M.P. Seah and W.A. Dench, *Surface and Interface Analysis*, **1** (1979) 2

[Shi72]   D.A. Shirley, *Physical Review B*, **5** 12 (1972) 4709

[Tag80]   E. Taglauer, W. Heiland and J. Onsgaard, *Nuclear Instruments and Methods* **168** (1980) 571

[Tan88]   S. Tanuma, C.J. Powell and D.R. Penn, *Surface and Interface Analysis*, **11** (1988) 577

[Tan91a] S. Tanuma, C.J. Powell and D.R. Penn, *Surface and Interface Analysis*, **17** (1991) 911

[Tan91b] S. Tanuma, C.J. Powell and D.R. Penn, *Surface and Interface Analysis*, **17** (1991) 927

[Ugo92]   D. Ugolini, J. Eitle and P. Oelhafen, *Applied Physics A* **54** (1992) 57

[Ver98]   H. Verbeek, J. Stober, *Nuclear Fusion* 38 **12** (1998) 1789

[Vie82]   E. Vietzke, K. Flaskamp, and V. Philipps, *Journal of Nuclear Materials* **111&112** (1982) 763

[Wer92]   W.S.M. Werner, *Surface and Interface Analysis* **18** (1992) 217

List of publications

Surface reactions on beryllium after carbon vapour deposition and thermal treatment

Journal of Nuclear Materials, **290-293** (2001), 76

P. Goldstrass, K. U. Klages and Ch. Linsmeier

ARTOSS – A New Surface Science Experiment to Study the Hydrogen Inventory in Multi-Component Materials

Physica Scripta **T94** (2001) 28

Christian Linsmeier, Peter Goldstraß, and Konrad U. Klages

Deuterium bombardment of carbon and carbon layers on titanium

Journal of Nuclear Materials, **313-316** (2003) 56

K. U. Klages, A. Wiltner, J. Luthin and Ch. Linsmeier

Oxidative erosion of graphite in air between 600 and 1000 K

Journal of Nuclear Materials, **341, 1,** (2005), 31

M. Balden, K.U. Klages, W. Jacob and J. Roth